KfK 4777
September 1990

Development of the KfK NET Toroidal Field Coil React and Wind Conductor

Final Report, June 1990

R. Flükiger, R. Heller, P. Komarek, W. Maurer, M. Klemm, K.-R. Leimbach, A. Nyilas, C. Schmidt, W. Specking, P. Turowski, A. Ulbricht

Institut für Technische Physik
Projekt Kernfusion

Kernforschungszentrum Karlsruhe

KERNFORSCHUNGSZENTRUM KARLSRUHE

Institut für Technische Physik

Projekt Kernfusion

KfK 4777

Development of the KfK NET Toroidal Field Coil React and Wind Conductor

Final Report, June 1990

by

R. Flükiger, R. Heller, P. Komarek, W. Maurer, M. Klemm, K.-R. Leimbach*,
A. Nyilas, C. Schmidt, W. Specking, P. Turowski, A. Ulbricht

*Ruhr-Universität Bochum, Fakultät für Bauingenieurwesen

Kernforschungszentrum Karlsruhe GmbH, Karlsruhe

Kernforschungszentrum Karlsruhe GmbH
Postfach 3640, 7500 Karlsruhe 1

ISSN 0303-4003

Abstract:

In the frame of the Euratom Fusion Technology program an A15 forced flow cooled conductor for the toroidal field (TF) coils of the Next European Torus (NET) was developed at KfK Karlsruhe. The conductor is based on the bronze route of Nb_3Sn. It was designed as a react and wind conductor in a sandwich type where the flat Nb_3Sn Rutherford cable was enclosed between two Cu stabilizers based on roebeled Cu profiles. A subsize conductor at the scale 1:1.75 was fabricated for developing the industrial fabrication procedure and testing the electrical properties within an acceptable cost frame. For the heat treatment of the Rutherford cable a suitable process was developed. No unexpected degradations were found on samples taken at different fabrication stages and tested in the FBI facility at KfK. In a late stage of development the NET parameters were changed which loaded the conductor with 10 times higher field transients caused by plasmas disruption with respect to the original specifications. A detailed analysis showed that the conductor fulfilled further all specifications except the field transients of the plasma disruption where the conductor will quench. The development of the Nb_3Sn conductor in react and wind technique demonstrate that this conductor type is feasible using the common manufacturing techniques of large coils which were already successfully demonstrated in the Large Coil Task and in the KfK-Polo project.

Entwicklung des KfK NET Toroidal-Feldspulenleiters

Abschlußbericht, Juni 1990

Zusammenfassung:

Im Rahmen des europäischen Fusions-Technologie-Programmes wurde im KfK Karlsruhe ein forciert gekühlter A15 Leiter für die toroidal Feldspulen des NET (Next European Torus) entwickelt. Der Leiter basiert auf der bewährten Bronzefertigungstechnologie. Der Leiter ist vom "react and wind (reagieren und wickeln)" Typ, bei dem das reagierte Nb_3Sn Flachkabel mit einer CuNi-Umhüllung zwischen zwei verroebelten Cu-Flachleitern eingelötet wird. Um den Leiter innerhalb eines tragbaren Aufwands industriell entwickeln und testen zu können, wurde ein verkleinerter Leiter im Maßstab 1:1,75 gefertigt. Für die Durchführung der Reaktionsglühung des Flachkabels ist ein geeignetes Verfahren entwickelt worden. Dieser Leiter wurde in den verschiedenen Stufen seiner Fertigung in der Zugapparatur FBI im KfK-Karlsruhe bezüglich seiner kritischen Daten vermessen. Es war keine Degradation im Rahmen der üblichen Schwankungsbreite feststellbar. In einem späten Stadium der Entwicklung haben sich die Anforderungen bezüglich der bei dem Plasmaabriß auftretenden zeitlichen Feldänderungen um einen Faktor 10 geändert. Aufgrund einer Untersuchung wurde festgestellt, daß der Leiter alle anderen Spezifikationen weiterhin erfüllen kann, der Plasmaabriß aber zur Normalleitung des Leiters führt. Mit der durchgeführten Entwicklung wurde gezeigt, daß ein Leiter in "react and wind" Technik industriell herstellbar ist, wobei die Herstellungstechniken weitgehend am Euratom-LCT Leiter und dem Polo-Leiter demonstriert wurden.

Contents

1. INTRODUCTION

The European superconducting laboratories were called by the NET team in October 1984 to design a Nb_3Sn conductor for the toroidal field coils of NET, at that time based on the react and wind technique. Most of the laboratories followed the call and worked on a conductor design [1.1]. The 1:1 scale conductor favoured by the NET team started the discussion about the testing possibilities and facilities. In a series of workshops within the laboratories over a period of about two years suitable test programmes and the required facilities were discussed [1.2, 1.3]. The result was the conversion of the Sultan facility to a split coil geometry for short sample measurements and the upgrading of the TOSKA facility at KfK in Karlsruhe for model coil testing. Both test facilities are suitable for testing overall properties of short samples of full size conductors and allow also the test of model coils manufactured from the latter. The practical experiences with Nb_3Sn conductors showed the necessity of starting the development with a subsize NET-conductor in order to reduce the costs and to perform test runs with already existing test facilities, e.g. the FBI high field test facility at KfK [1.4]. The developments were performed in collaboration with industry. Representative steps of the fabrication of various components were performed at an industrial scale.

The KfK-NET-TF conductor is based on the following principles:

- forced flow cooling for
  - ensured electrical insulation,
  - effective force transmission,
  - predictable thermohydraulics, and
  - simplified winding fabrication;

- large wetted perimeter for a given hydraulic diameter to provide optimal stability,
- mechanically fixed conductor strands to avoid disturbance energy created by mechanical movement,
- strand separation or resistive barriers for reducing AC losses, and
- steel reinforcement for force transmission, support of the large hoop stresses and minimization of transverse stresses.

In order to avoid an excessive prestrain on the Nb_3Sn strands, the reinforcing steel is introduced after the reaction heat treatment ("react and wind" technique).

The way to proof the various steps of fabrication technique was to manufacture a subscale conductor at a scale 1:1.75. Heat treatment of long conductor lengths required a careful method to fix the cable on the reaction drum. This was done in order to compensate different thermal expansion, to avoid sintering between the layers, and to keep a constant temperature in time and space during the reaction. Soldering procedures were developed, not only for the subsize, but also for the 1:1 fabrication scale. During the different fabrication stages measurements of the critical current under field and strain of the strands, the flat Rutherford cables, the mechanical stabilized cable, the cable with copper stabilizers and finally with the steel jacket were performed in the KfK-FBI facility. No inconsistency was found. The application of laser beam technology for the assembly of the jacket from drawn stainless steel sections was successfully demonstrated within the Polo project by manufacturing 4 x 150 m of the Polo conductor [1.5]. The successful welding in combination with the KfK-TF conductor development demonstrates the fabricability of such a conductor in an industrial scale.

The original design parameters for the KfK-NET-TF conductor were taken from the NET I design of the NET team. The critical discussion of this design within the Community resulted in a NET II design with considerably higher plasma current (22 MA) compared to NET I (11 MA). This led to larger coils with an increase of the forces by about 30% and much higher dB/dt due to plasma disruptions. The need for more structural material and higher stability margins requires also a higher current density, especially for the central solenoids with high mechanical load. Presently no A15 material is available and produced at an industrial scale which is able to cover all the required specifications. It is the aim of this report to check the KfK-TF-conductor concept for the conductor in order to fulfill NET II toroidal field coil specifications and to explore the limits of the conductor. The result of the fabrication developments is described in detail.

[1.1] R. Flükiger, F. Arendt, A. Hofmann, U. Jeske, K.P. Jüngst, P. Komarek, H. Krauth, W. Lehmann, J. Lühning, B. Manes, W. Maurer, A. Nyilas, W. Specking, P. Turowski, H. Zehlein, KfK 3937, Juni 1985.

[1.2] J. Erb, A.Grünhagen, W. Herz, I. Horvath, K. Jentzsch, P. Komarek, K. Kwasnitza, E. Lotz, S. Malang, C. Marinucci, W.Maurer, G. Nöther, G.

Pasztor, A. Peters, A. Roeterding, C. Sborchia, A. Ulbricht, A. Vogt, P. Weymuth, G. Zahn, KfK 4355, Nov. 1987.

[1.3] A. Grünhagen, R. Heller, W. Herz, A. Hofmann, K. Jentzsch, H. Kapulla, B. Kneifel, P. Komarek, W. Lehmann, W. Maurer, G. Ries, B. Rzezonka, H. Salzburger, Ch. Schnapper, A. Ulbricht, A. Vogt, G. Zahn, KfK 4602, Juli 1989.

[1.5] W. Specking, A. Nyilas, M. Klemm, A. Kling, R. Flükiger, Proc. MT-11 28 Aug. - 1 Sept. 1989, Tsukuba, Japan.

[1.6] S. Förster, G. Friesinger, R. Heller, U. Jeske, G. Schenk, G. Nöther, C. Schmidt, L. Siewerdt, M. Süßer, A. Ulbricht, F. Wüchner, P. Bonnet, A Bourquard, F. Geyer, H. Schadt, Proc. 16th SOFT 3 - 7 Sept. 1990, London, UK

2. CONDUCTOR SPECIFICATIONS

2.1 Specifications for NET I

The specifications for the conductor changed considerably during the development of the design for NET. The starting point in 1984 was a nominal current of 20 kA and a maximum field of 11 T. AC losses and nuclear heat were taken into account.

As boundary conditions for the conductor design, the NET I parameters have been used. Following informations provided by the NET team have been taken into account [2.1]:

- the coil definition given in the note from February 2, 1984,
- the operation scenario given in the note from March 23, 1984,
- the preliminary stress results given in the note from March 23, 1984,
- the transient field distribution across the TF coils calculated by N. Mitchell,
- the calculation of field and force distribution by M. V. Ricci,
- the neutronic calculation for heat and radiation energy deposition by W. Daenner (NET/IN/84-067, 26.07.1984).

Basis of the original design was a critical current of 30 kA at 12 T and 4.2 K and an operational current of 20 kA. The maximum field at that time was 10.7 T for the TF coils, but the scenario for NET was not fully developed and changes

were expected. Further development of the conductor is described in [2.2]. Special care was taken for the fabrication of the steel jacket of the conductor.

During the development phase of testing scenarios for NET model coils described in [2.3, 2.4, 2.5] no severe change in the parameters was conceivable. Even in the report [2.3] the following target test values were given for the NET-TF conductors as listed in Table 2.1:

Parameter	Unit	Value
Maximum field at conductor	T	11.4
Operating Current	kA	16
Peak winding pack stresses		
- radial	MPa	- 40
- toroidal	MPa	- 140
- hoop	MPa	140
- shear	MPa	30
Maximum rate of field change		
- normal operation	T/s	0.55
- plasma disruption	T/s	1.0 estimate, to be confirmed by further analysis
Nuclear heating in winding pack		
- average	mW/cm^3	0.05
- peak	mW/cm^3	0.3

Table 2.1: Target test values for TF coils (TF-conductors)

2.2 Conductor specifications for NET II

During the development of the NET scenario from NET I to NET II new specifications were defined. The main reason for that were a new plasma scenario with disruptions creating about 40 T/s at the PF solenoid. Test conditions for the conductor were defined for the test of model coils. They are listed in Table 2.2 compared to the values for the TF coils in operation. The values are extracted from Refs. [2.6, 2.7, 2.8, 2.9]. Supplementary informations are contained in Tabs. 2.3 and 2.4.

Table 2.2: New target test values for conductors and model coils (MC)

Parameter	Unit	Value for TF coil	Value for MC test
Minimum bending radius	m	~ 2.7	1
$J_{op.cable}$		$0.6 J_{crit.cable}$	up to $J_{crit.cable}$
Cable space current density	$\frac{MA}{mm^2}$	65.5	~ 65
Operating current	kA	16	23
Total coil current	MA	9.1	~ 7.5
Maximum field at conductor	T	11.2	~ 13.5
$\sigma_{vonMises}$ **(cable steel jacket)**	MPA		~ 600
Peak winding pack stresses **- radial** **- toroidal** **- hoop** **- shear**	 MPa MPa MPa MPa		
Maximum rate of field change **- normal operation**	 T/s		
Maximum dB/dt due to plasma disruption	T/s	[1]) ∥ 40 [2]) ⊥ 20	~ 40
$\int_0^{100\ ms}$ **(dB/dt) dt**	T	∥ 2 ⊥ 0.5	
$\int_0^{100\ ms}$ **(dB/dt)^2 dt**	T^2/s	∥ 50 ⊥ 5	
T_{max} **(hot spot)**	K	≤ 150	≤ 150
V_{max} **(dump)**	kV	≤ 20	≤ 10
τ_{dump} **for coil**	s	$2(1/16)E_s/(I_0U_0)$	~ 10
Quench internal pressure (max.)	MPa	≤ 20	≤ 20

1) Field parallel to the axis of the conductor
2) Field perpendicular to the axis of the conductor

Table 2.3: Supplementary values for the TF-coils

Parameter	Unit	Value for TF coil	Value for MC test
Cycling number		10000 full power PF coils	
Cool down cycles		20 during its life	
Maximum dose for insulation	rads (Gy)	2×10^9 (2×10^7)	
Maximum neutron fluence	n/cm^2	1×10^{23} ($E \geq 0.1$ MeV)	
Cu damage	dpa	1.1×10^{-3}	
Nuclear heating	W/coil	600	
Coupling time constant for AC losses	ms	$\sim$ 7	
Coil case AC losses	W/coil/cycle	200 on average	
Static heat flow	W/coil	$\leq$ 50	
Joint resistance	Ω/joint	$2.5x10^{-9}$ ($\sim$ 4 W per joint for 40 kA)	

Table 2.4: Supplementary values for the insulation of TF-coils

Parameter	Unit	Value for TF coil	Value for MC test
Insulation shear stress	MPa	30 (fatigue)	
Insulation compression stress	MPa	450	
Insulation tension strain	%	0.25	
Turn-to-turn voltage	V	~ 100	
Pancake-to-pancake voltage	V	~ 1700 (peak)	
Operating voltage	kV/mm	4	
Minimum separation		1.5 mm between turns	
Minimum separation		2.5 mm between pancakes	
Minimum thickness		10 mm of ground insulation + additional Kapton film	

References

[2.1] R. Flükiger, F. Arendt, A. Hofmann, U. Jeske, K.P. Jüngst, P. Komarek, H. Krauth, W. Lehmann, J. Lühning, B. Manes, W. Maurer, A. Nyilas, W. Specking, P. Turowski, and H. Zehlein, "An A15 Conductor Design and its Implication for the NET-II TF Coils", Final Study Report, KfK 3937, June 1985.

[2.2] R. Flükiger, U. Jeske, P. Komarek, A. Nyilas, P. Turowski, A. Ulbricht, "Status of the Development of the KfK NET Toroidal Field Conductor", Proc. 15th SOFT, Utrecht, Netherlands, September 19-23, 1988, pp. 1589-1595.

[2.3] J. Erb, A. Grünhagen, W. Herz, I. Horvath, K. Jentzsch, P. Komarek, K. Kwasnitza, E. Lotz, S. Malang, C. Marinucci, W. Maurer, G. Nöther, G. Pasztor, A. Peters, A. Roeterdink, C. Sborchia, A. Ulbricht, A. Vogt, P. Weymuth, G. Zahn, "NET Model Coil Test Possibilities", Final Study Report KfK 4355, November 1987.

[2.4] A. Grünhagen, R. Heller, W. Herz, A. Hofmann, K. Jentzsch, H. Kapulla, B. Kneifel, P. Komarek, W. Maurer, G. Ries, B. Rzezonka, H. Salzburger, Ch. Schnapper, A. Ulbricht, A. Vogt, G. Zahn, "NET Model Coil Test Possibilities in the TOSKA TWIN Configuration", KfK 4602, July 1989.

[2.5] A. Hofmann, P. Komarek, A. Maurer, W. Maurer, G. Ries. B. Rzezonka, H. Salzburger, Chn. Schnapper, A. Ulbricht, G. Zahn, "Further Use of the EURATOM LCT Coil", Proc. 15th SOFT, Utrecht, Netherlands, September 19-23, 1988, pp. 1596-1602.

[2.6] N. Mitchell, A. Portone, "Design Basis for the Plasma System", N/P/3010/1/A, 11.12.1989.

[2.7] N. Mitchell, L. Bottura, "Design Basis for the Toroidal Field Coils", N/P/3510/2/B, 28.11.1989.

[2.8] N. Mitchell, L. Bottura, F. Fardi, "Concept Design and Analysis of the Toroidal Field Coils", N/P/3510/3/A, 24.10.1989.

[2.9] R. Annandale, L. Bottura, N. Mitchell, M. Perella, E. Salpietro, "Concept Definition and Analysis of the NET Model Coils", N/R/0221/1/A, 19.02.1990.

3. THE CONDUCTOR CONCEPT

3.1 General features

The main design features of the NET-KfK-TF conductor can be summarized as follows:

- a transport current of 16 kA at 11.5 T and 4.2 K.,
- low AC losses induced by pulsed operation of poloidal field coils by using Nb_3Sn strands fabricated by the bronze route, i.e. with external bronze,
- extremely flat Nb_3Sn cable to minimize bending strains,
- large contact surface of the Nb_3Sn strands, minimizing the local compressive transverse stress,
- forced flow supercritical helium flowing through defined internal cooling channels, and
- stainless steel jacket as a conduit withstanding high transversal and compressive stresses.

According to the guidelines above the present status of the KfK-NET-TF conductor is given in Fig. 3.1. The design can roughly be divided into three major components: the core, the electrical stabilizer and the stainless steel jackets.

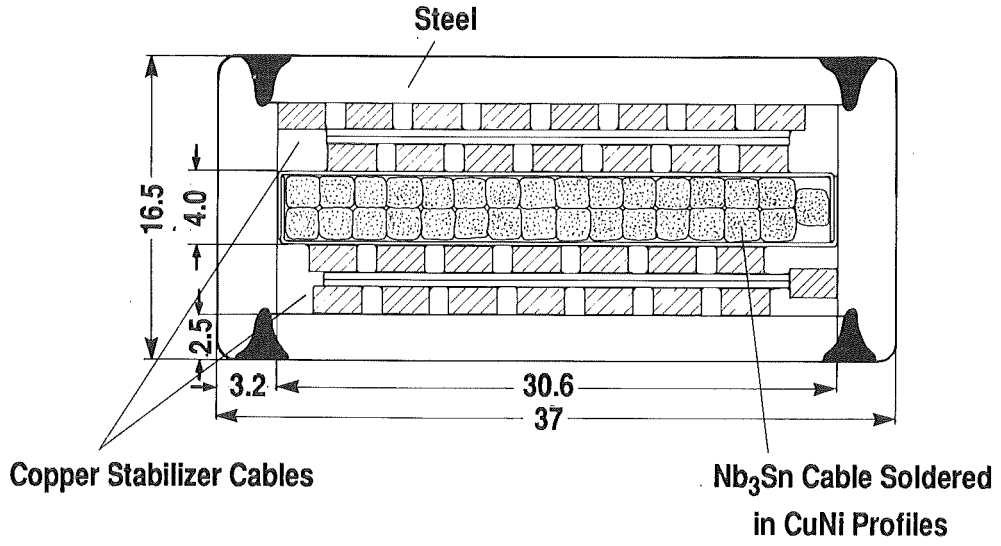

Fig. 3.1: Cross section of KfK-NET-TF superconductor concept with its main dimensions.

The development philosophy is based on:

- A step by step progress to a full size superconductor development on the basis of an industrial manufacturing program of a relevant subsize conductor.
- Introducing of both manufacturing experience and conductor test results collected during the subsize development to the full size KfK-NET-TF superconductor.

In order to get a better control of the fabrication steps and the properties of a full size conductor, a subsize conductor at a scale of 1:1.75 was fabricated and successfully tested.

3.2 Details of the conductor design

The main technical characteristics of the full size conductor are listed in Tables 3.1 to 3.4.

The components of the conductor are described as follows.

3.2.1 The superconducting core

The rectangular superconducting core consists of a Nb_3Sn flat cable, soldered within a thin sheated CuNi conduit with external dimensions of 4.0 x 30.6 mm^2. The flat cable consists of 31 internally stabilized Nb_3Sn strands. The strand diameter is 1.92 mm and can be routinely produced by the industrially available bronze route process. The large diameter of 1.92 mm leads to a number of about 50 000 filaments with an approximate diameter of 4 µm. The strands are composed of 433 Nb/CuSn elements at a first stage which are bundled again to 114 elements (total of 433 x 114 = 49362 filaments). The internal stabilizing copper is placed at the center of the strands.

Table 3.1: Main technical characteristics of the KfK-NET-TF conductor

Parameter	Unit	1986 [3.1]	1988 [3.2]	1990
Outer conductor dimensions (without insulation)	mm^2	37.0 x 16.5	37.0 x 16.5	37.0 x 16.5
Dimensions including CuNi sections	mm^2	30.6 x 5.1	30.6 x 4.0	30.6 x 4.0
Thickness of stainless steel jacket	mm	1.5 / 2.5+0.7	2.5 / 3.2	2.5 / 3.2
Delivery length in multiples	m	800 / 1600		
Number of sc strands		29	31	31
Number of stabilizer cables		2	2	2
Number of Cu strands per stabilizer cable		13	15	15
Critical current at 12 T / 4.2 K / ε = 0.3 %	kA	24	22	31.4
Note: to 1988 : VAC NS-10000(0.8) - 20 % degradation to 1990 : J_c increased by 50 % [3.3] - 30 % degradation				
Rated current at 12 T / 4.2 K	kA	16	16	16
Cross section of sc (non copper bronze)	cm^2	0.613	0.691	0.691
Note: Nb_3Sn + bronze (without 23 % Cu and 4 % Ta) for [3.1] Nb_3Sn + bronze (without 17 % Cu and 6 % Ta) for [3.2]				
Cross section of Cu in stabilizers	cm^2	1.248	1.17	1.17
Cross section of Ta	cm^2	0.034	0.054	0.054
Cross section of Cu in sc strand	cm^2	0.193	0.153	0.153
Cross section of helium channels	cm^2	0.9504	0.789	0.886
Wetted perimeter of helium channels	cm	18.56	18.52	19.58
Cross section of folder strip	cm^2	0.138	-	-
Cross section of CuNi barriers	cm^2	0.314	0.1528	0.1528
Cross section of steel conduit	cm^2	1.974	2.586	2.586

Table 3.2: Characteristics of the superconducting cable core of the KfK-NET-TF conductor

Parameter	Unit	1986 [3.1]	1988 [3.2]	1990
Dimensions including CuNi sections	mm^2	30.6 x 5.1	30.6 x 4.0	30.6 x 4.0
Cross section of strand	cm^2	0.613	0.691	0.691
Note: Nb_3Sn + bronze (without 23 % Cu and 4 % Ta) for [3.1] Nb_3Sn + bronze (without 17 % Cu and 6 % Ta) for [3.2]				
Number of strands		29	31	31
Strand diameter	mm	1.92	1.92	1.92
Transposition length	mm	600	300	300

Table 3.3: Characteristics of the superconducting strands of the KfK-NET-TF conductor

Parameter	Unit	1986 [3.1]	1988 [3.2]	1990
Superconducting material		Nb_3Sn or $(Nb-7Ta)_3Sn$	Nb_3Sn or $(Nb-7Ta)_3Sn$	Nb_3Sn or $(Nb-7Ta)_3Sn$
Processing		Bronze process	Bronze process	Bronze process
Strand diameter	mm	1.92	1.92	1.92
Bronze/Nb ratio		3.1 : 1	3.1 : 1	3.1 : 1
Number of filaments		~ 56000	~ 50000	~ 50000
Size of filament	μm	~ 4	4 - 6	4 - 6
Twist pitch	mm	50	50	50
J_c (non copper) at 12 T / 4.2 K / $\varepsilon = 0$	$\frac{A}{cm^2}$	$4.2\ 10^4$	$3.96\ 10^4$	$5.15\ 10^4$
J_c (non copper) at 12 T / 4.2 K / $\varepsilon = 0.3$ %	$\frac{A}{cm^2}$	$3.36\ 10^4$	$3.17\ 10^4$	$4.54\ 10^4$
J_c (overall strand) at 12 T / 4.2 K / $\varepsilon = 0$	$\frac{A}{cm^2}$	$3.1\ 10^4$	$3.05\ 10^4$	$3.80\ 10^4$
Note: to 1988 : VAC NS-10000(0.8) - 20 %degradation to 1990 : J_c increased by 50 % [3.3] - 30 % degradation				

Table 3.4: Characteristics of a stabilizer cable of the KfK-NET-TF conductor

Parameter	Unit	1986 [3.1]	1988 [3.2]	1990
Outer dimensions	mm^2	30.6 x 4.2	30.6 x 3.75	30.6 x 3.75
Material		Cu-profiles (1/4 hard-ened)	Cu-profiles (1/2 hard-ened)	Cu-profiles (1/2 hard-ened)
RRR			~ 100	~ 100
Number of units		2	2	2
Number of stabilizers per unit		13	15	15
Distance of stabilizers	cm	0.16	0.12	0.12
Wire dimensions	mm^2	3.0 x 1.6	2.6 x 1.5	2.6 x 1.5
Cross section of stabilizers	cm^2	1.248	1.17	1.17
Cross section of helium channels	cm^2	0.9504	0.789	0.886
Wetted perimeter of helium channels	cm	18.56	18.52	19.58
Hydraulic diameter	cm	0.205	0.170	0.181
Heat transfer area (copper + strands)	cm^2	16.44	11.02	11.28

The required diffusion barrier during the reaction heat treatment consists of Ta.

The 31 strands are cabled with a standard planetary cabling machine with 100 % backtwist. The transposition pitch is in the same sense as the twist pitch, the transposition length being about 300 mm. In contrast to the former design where a ceramic insulated core strip was incorporated at the center of the cable to minimize the losses, the current status is to produce the cable without an electrical insulated core strip. The reasons for the elimination of this core strip are:

- Cabling of the Nb_3Sn strands on a core still bears manufacturing risks due to the high elastic spring back effect of the Cu-13wt.%Sn bronze. After the cabling process the core strip is subjected to high compressive stresses in axial direction, thus enhancing the risk of cable collapsing after removal from the cabling machine, e.g. during the reeling of the cable on the reaction heat treatment drum.
- Removal of the core strip was beneficial in this design, because of the reduction of the core thickness. The latter became necessary due to the increased jacket thickness of the cover sheets. This sheet thickness was no more force withstanding due to the increase of transversal stresses from 70 MPa (former design value) to 140 MPa in the current magnet reference design. A second beneficial effect of the core thickness reduction is the further reduction of the bending strain.
- The current situation of the AC loss calculations for this cable along with some experiments shows that the AC losses of the cable may still be acceptable without an insulated core strip.

After the calibration to a rectangular shape the Nb_3Sn cable itself will have a dimension of 29 x 3.45 mm. This cable will be subjected to a reaction heat treatment process. During the subsize cable development programme the heat treatment process turned out to be one of the most important key problems. The first reaction heat treatment with a ~ 100 m length subsize cable (12.45 x 1.95) was carried out with a 1200 mm ∅ drum of the Swiss PSI laboratory under pure Argon atmosphere. The drum material (Inconel 600) and the core strip (Duratherm) of the cable have integral thermal expansions between 300 K and 1000 K of approximately 1.1 % and 0.6 %, respectively. This non-matched condition of thermal expansion coefficients and the volume increase of the strands

during the formation of the Nb_3Sn layer led to unacceptable cable distortions after the heat treatment process (In the actual case, the cable was reeled on the drum as a layer winding). The final analysis showed that the cable dimensions after the process were increased by ~ 0.4 % in all dimensions (volumetric effect). Taking the present cable dimension of 29 x 3.45 mm and adding the 0.4 % volumetric increase one can fulfill the design goal to insert the cable after the reaction heat treatment process into the two CuNi10 U-type sections. These U-sections of 0.2 mm thickness give with their legs a defined closure during the soldering process, therefore the dimensional stability can be guaranteed. The soldering will take place in a vertical electrically heated ceramic mould. This device is already completed and the first dummy tests gave positive results. Figure 3.2 shows a schematic view of this soldering unit, which is designed in such a way that soldering of the subsize calbe as well as of the full size cable is possible.

The well characterized Sn58Pb39In3 with a melting point of ~ 235 °C has been chosen as solder material. In order to check the solder performance, double lap shear tests were carried out with a material combination of copper/copper (OFHC) and a lap area of 200 mm^2. The lap shear strength results are 23/26 MPa at 300 K and 30/48 MPa at 4 K, respectively. The ultimate strain capacity of the ~ 50 µm thick solder layer was found to be ~ 0.1 %, thus giving enough operational safety margin. The complete core will have a dimension of 30.6 x 4 mm^2 according to Fig. 3.1. If necessary an increase of the dimension in width of some tenths of a mm is still possible without harming the overall design. This aspect will be important at a later manufacturing period.

3.2.2 The electrical stabilizer

The two electrical stabilizers at both sides of the core (see Fig. 3.1), (which should carry the transport current during a fault condition), comprise rectangular 1/2 hard (RRR ~ 100) copper sections, which have been Roebel processed on a sandwich core strip with an electrical insulation at the center (state-of-the-art). The sandwich core consists of two copper plated strips of Ni80Cr20 glued together by adhesive insulation tape. The sandwich will be covered on both surfaces with the same solder (Sn58 Pb39 In3) as used in the superconducting core. The overall dimensions of this electrical stabilizer will be 30.6 x 3.75 mm^2. Each stabilizer consists of 15 copper sections (strands) of 2.6 x 1.5 mm^2. The Roebeling process, in particular the absence of electrical contacts between neighbouring Cu sections at

the edges (important for ac losses) has been already successfully demonstrated in short lengths of ~ 3 meters.

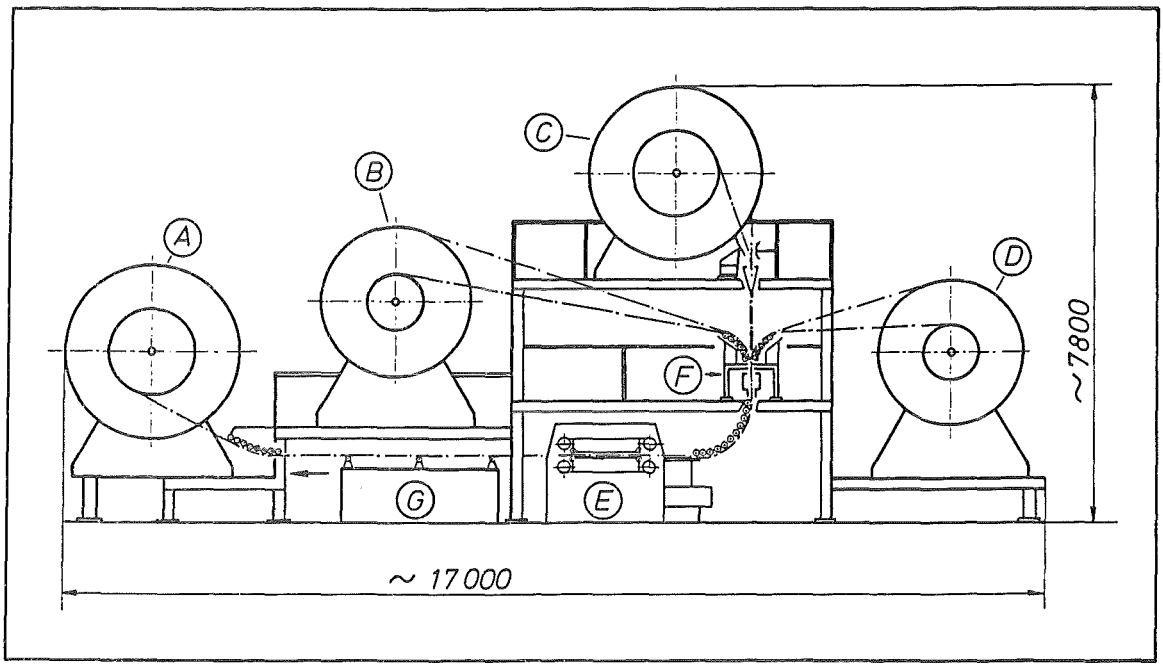

Fig. 3.2 Present core soldering line (courtesy of Vacuumschmelze GmbH, Hanau). (All dimensions in mm)

A) Take-up reel of the completed core 1500 ∅ - 3000 ∅ mm (working range)
B) Pay-off reel for CuNi U-section No. 1; 1000 ∅ - 2600 ∅ mm
C) Pay-off reel for prereacted superconducting cable 1500 ∅ - 3000 ∅ mm
D) Pay-off reel for CuNi U-section No. 2; 1000 ∅ - 2600 ∅ mm
E) Linear capstan
F) Vertical soldering station
G) Dimension control plus quality control

Calculations with the boundary condition of 16 kA and 15 s discharge time constant have shown that the Cu cross section in the Nb_3Sn strands can carry the transport current in the quench case without reaching non permissible "hot spot" temperatures (~ 150 K). The manufacturing of such cables is well demonstrated and the tolerances are very low, in the range of ± 10 µm for the completed cable as indicated by the manufacturers report [3.4] of the LCT cable.

These two stabilizers will then be joined with the prereacted core on an assembly line by soldering. The solder will be Sn50/Pb32/Cd18 with a low melting point of ~ 185 °C. By correct temperature adjustment the soldering can be

performed without a melt down risk of the already soldered core region. The unit lengths can be collected on a take up reel ready for the final jacketing process. This solder was also tested to have an appropriate data base for the present design. Again the 4 K values are higher compared to the ambient values. The results show lap shear strength values of 17/33 MPa at 300 K and 24/28 MPa at 4 K, respectively. The straining capacity of this solder is also in the same range as the previous one (~ 0.1 %).

3.2.3 The steel jacket

The steel jacket (see Fig. 3.1) is an essential part for the mechanical integrity of the conductor in the coil winding. It consists of two rectangular cover sections and two special T-shaped side sections. The jacket must withstand all mechanical loads during the magnet operation. According to the NET reference design the radial coil stresses and the toroidal coil stresses are -40 MPa and 140 MPa, respectively [3.5]. The hoop stresses are +140 MPa. The jacket sheet thickness along with the conductor aspect ratio give thus the mechanical performance of the conduit. The jacket material will be a high strength 316 LN type stainless steel, which was already successfully used in the past. Figure 3.3 shows schematically the jacket and the stresses acting on it. Before going on to detailed mechanical finite element calculations, a first estimation of the critical loads shows that the chosen jacket geometry may be capable to withstand the operational loads. The toroidal stress of -140 MPa results in a compressive stress of ~ -460 MPa in the 2.5 mm thick cover section. The materials 4 K yield strength (~ 1200 MPa) is far above this value.

The toroidal load of each side section is calculated to be 1150 N per mm of conductor length. Taking the cover section of 37 mm length as a column, the calculated critical load is ~ 1800 N per mm of conductor length. Considering the weldments plus the winding pack stiffening effect, a buckling phenomenon may be therefore outruled. The side section with its 3.2 mm thickness is subjected to a deflection under the toroidal stress of -140 MPa. The maximum deflection assuming a non supported beam of 11.5 mm length is ~ 60 µm. This value will drop down considerably by the mechanical supporting of this beam by the weldments. The deflection of the cover section is accordingly the more severe one due to the length of 30.6 mm. Considering the radial stress of - 40 MPa the deflection yields a value of ~ 1.7 mm. This means that the interior of the jacket will be subjected to considerably compressive stresses. The smaller stress of -40 MPa will increase to ~ -70 MPa due to the stress transmission. This - 70 MPa will therefore act as a radial stress on the superconducting core. Due to the presence of

solder and the correlated distribution of stresses in the core, the compressive stress of 70 MPa is the effective stress acting on the Nb_3Sn wires. This is strongly different from other configurations, e.g. the cable-in-conduit, where the effective compressive stress at the crossover points is much higher. According to Ref. [3.6] transversal compressive stresses of the order of 70 MPa at 12 T lead to a decrease of J_c by ~ 25 %.

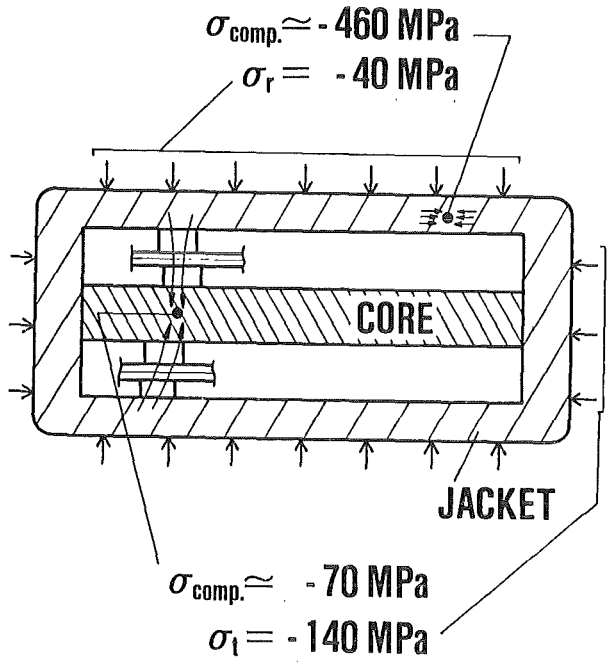

Fig. 3.3: Conductor jacket and the stresses (NET I) acting on it during operation

In order to maintain a sufficient safety margin for the overall critical current, it is necessary to use Nb_3Sn wires with considerably higher critical current densities than originally thought. A prototype study undertaken in our laboratory has demonstrated that the critical current density of bronze route Nb_3Sn can be further increased [3.11]. A detailed stress distribution calculation accompanied by an integral electrical test is necessary to determine the effect of local stress enhancement and the corresponding current degradation of the superconducting core.

The present jacket design has been also improved compared to the former jacket configuration [3.7], which used tack welded spacer sheets. A major manufacturer gave a bid on the fabrication of the side section by a forming process for the necessary long lengths. Figure 3.3 shows the section in detail. The geometrical tolerances and the evaluation of manufacturing risks for long lengths

of such a section represent one major milestone before going on to a detailed final jacket design.

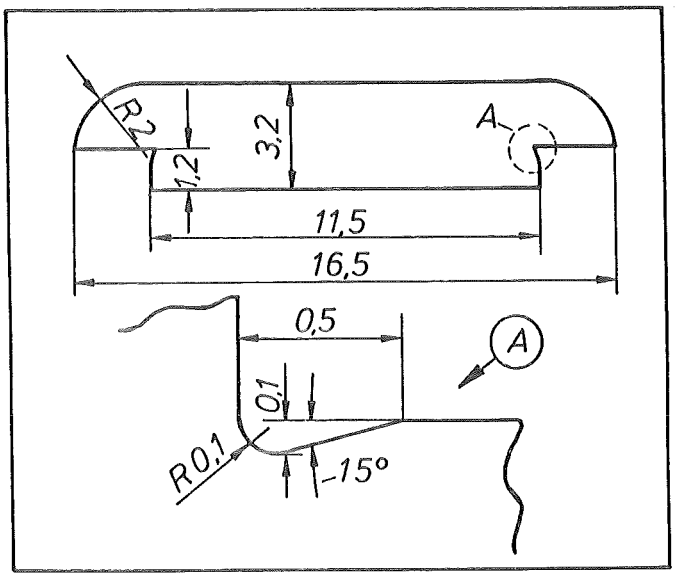

Fig. 3.4: Side section of the conductor jacket manufactured by continuous forming process. A) according to DIN 509 (All dimensions in mm).

A key technology of the jacket design is the continuous laser beam welding of the four seams. The deep weld profile of ~ 2.8 mm forces to switch on to laser beam weld process, because of the low heat input of this technique. Details of this weld procedure are given in ref. [3.8]. According to the recent short dummy welding tests on short lengths the temperature rise of the interior (important because of the soldered stabilizer) has been proven to be negligible [3.9]. At present we prefer the following manufacturing route:

- Prefabrication of the U-shape with two simultaneously working laser stations of ~ 4 kW power range.

- Reel on of the produced U-shaped configuration on a > 3.5 meter ∅ take up reel.

- Closure of the U-shaped section after the cable assembling in one step, again with two laser beam working stations.

The success of this process must be proven as early as possible with representative lengths. There is no doubt that the laser beam welding technology can be applied after the successful demonstration of welding of 4 x 150 m Polo conductor with two laser beams [3.10].

References

[3.1] A. Nyilas, private communication

[3.2] R. Flükiger et al., "Status of the development of the KfK NET Toroidal Field conductor", Proc. of the 15th Symp. on Fus. Techn., Utrecht, September 19-23, 1988, pp. 1589-1595.

[3.3] M. Klemm, E. Seibt, W. Specking, J.Q. Xu and R. Flükiger, "Enhancement of j_c at 10-12 T in Nb_3Sn Wires by Artificial Ta Inclusions distributed at a Nanometer Scale", to be published in Supercond. Sci. and Techn.

[3.4] R. Bezouska et al., "LCT Entwicklungsarbeiten zur Herstellung eines Supraleiters mit forcierter Kühlung", 1982 VAC Abschlußbericht VAC BA 99371.

[3.5] NET Status Report No. 84, Dec. 1987 EURFU XII-80/88-84.

[3.6] W. Specking, W. Goldacker and R. Flükiger, Adv. Cryo. Eng., Vol. 34 (1987) 569.

[3.7] R. Flükiger et al., An A15 Conductor Design and its Implications for the NET-II TF Coils, EURFU XII/361-85/37.

[3.8] A. Nyilas, "Laser Beam Welding of Advanced Superconducting Cable Conduits", 14th Symp. on Fus. Techn. Proc. SOFT Conf., Avignon, F, Sept. 8-12, 1986.

[3.9] J.M. Plaum et al., "Development Toroidal Field Conductor for NET", ECN-87-158 presented at the 10th Int. Conf. on Magnet Techn., Boston, Sept. 23-26, 1987.

[3.10] S. Förster et al., "Development of Components for Poloidal Field Coils within the KfK-Polo-Project. Proc. 16th SOFT, London U.K., Sept. 3.-7. 1990.

[3.11] R. Flükiger, M. Klemm and W. Specking, Appl. Supercond. Conference, Sept. 90, Snowmass (USA).

4. CALCULATIONS

4.1 Transfer of winding stresses to the core

Investigations on the effect of stress levels in both longitudinal and in axial direction showed that Nb_3Sn multifilament wires are sensitive to both [4.1.1] (Fig. 4.1.1). The critical current degraded under the effect of external forces, the conductor being more sensitive to axial stresses than to longitudinal stresses. Therefore a two dimensional FEM was used in order to get an impression how and under which boundary conditions the winding stresses were transferred to the Nb_3Sn core of the KfK-NET-TF conductor. The radial and axial stress levels in the winding are given in Fig. 3.3. These values are winding stresses for the NET I design. The larger coil of the NET II design increase them by about 30 %. Both designs were investigated.

The investigations were performed both on a half model and a quarter model of the conductor. The last one showed better resolution of peak stress levels in the jacket [4.1.2] (Fig. 3.3). In order to simulate the boundary conditions of the conductor in the winding, a movement to the outside is prohibited. Two load cases were calculated, the load case with the nominal stress levels marked with the load factor 1 (NET I) and the 30 % higher stress levels marked with the load factor 1.3 (NET II).

A lateral gap between the electrical part of the conductor and the stainless steel jacket was assumed in order to investigate the stress transfer and the supporting effect of the jacket. Displacements and stress levels for a gap with a dimension from 0 to the maximum value can be derived by application of both results using scaling factors. The calculated principal stresses for the load factors 1 and 1.3 are presented in Fig. 4.1.3.

A gap of 0.05 mm already leads to stresses of -100 MPa and exceeds the level of -70 MPa for 30 % degradation. Allowing a gap of 0.1 mm for assembling reduced by a worst tolerance of 0.015 mm the actual gap is 0.85 mm. In this case the stresses in the superconducting cable were calculated to be about -770 MPa.

In the jacket of the conductor the peak principal stress appears for an open gap of about -800 MPa for a load factor of 1 and about -1000 MPa for a load factor of 1.3.

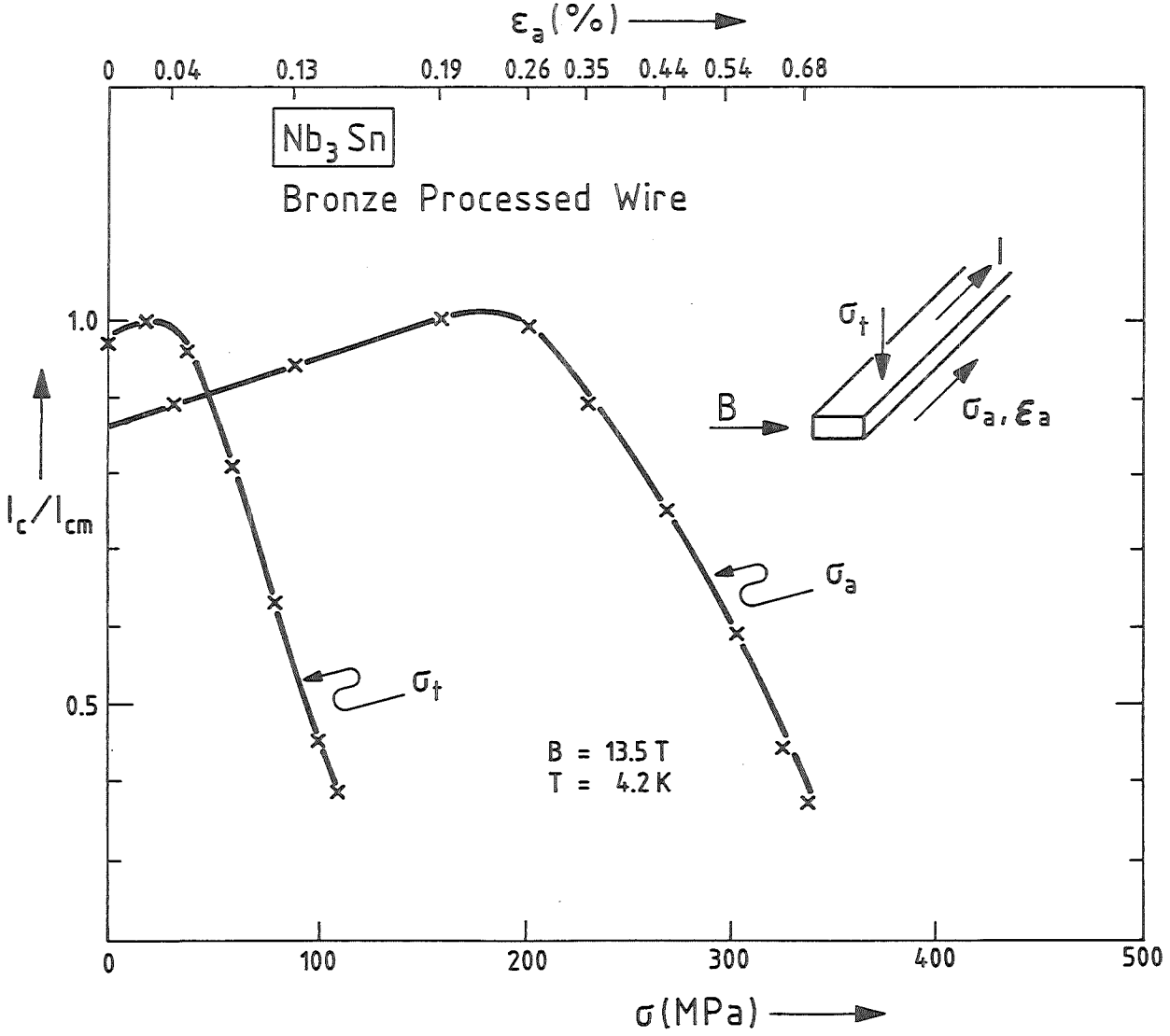

Fig. 4.1.1: Transverse and axial stress dependence of the critical current of a Nb_3Sn conductor

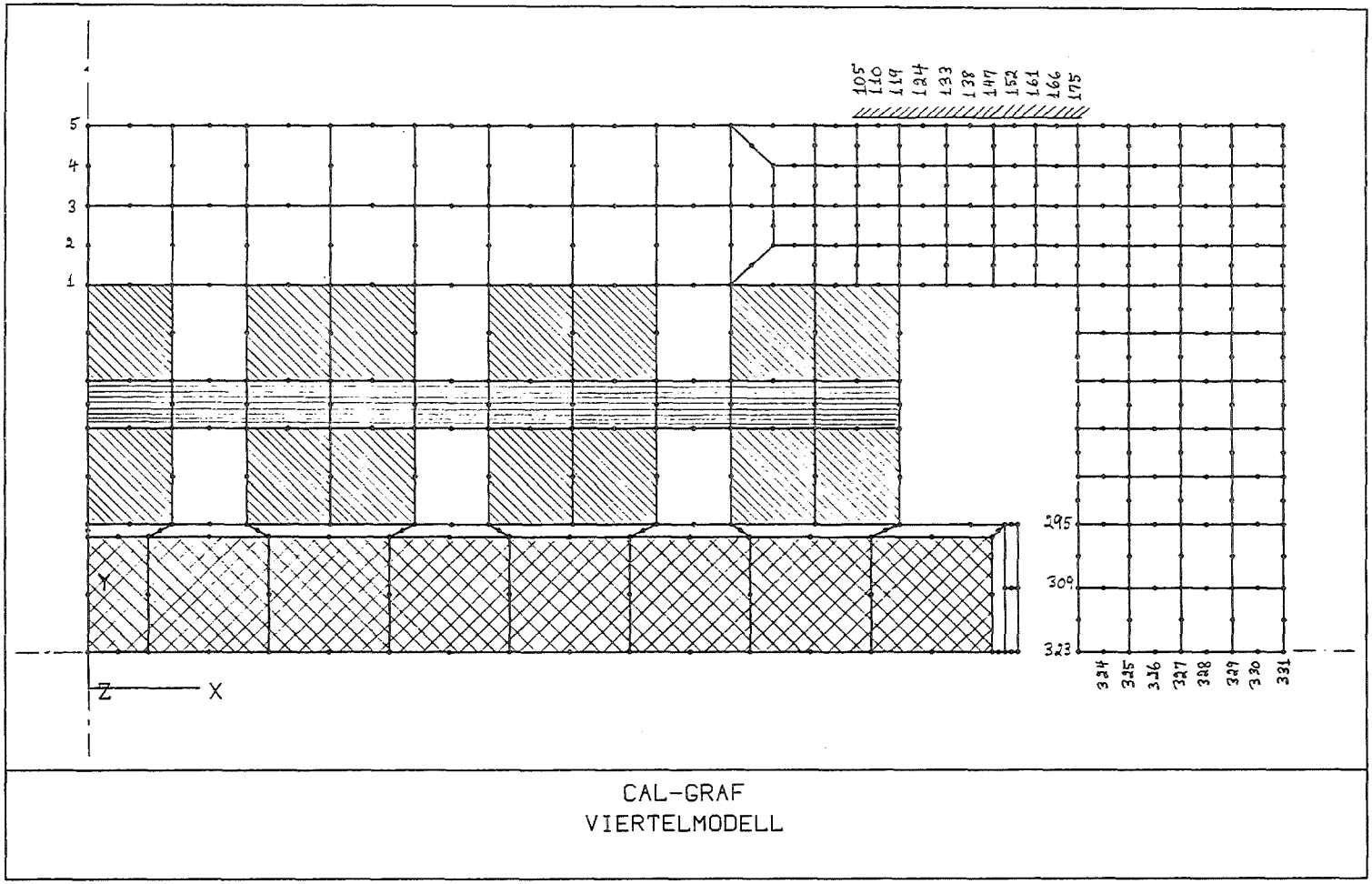

Fig. 4.1.2: Finite element model of a quarter section of the conductor. Elements 105 to 175 are prohibited to move towards the outer direction.

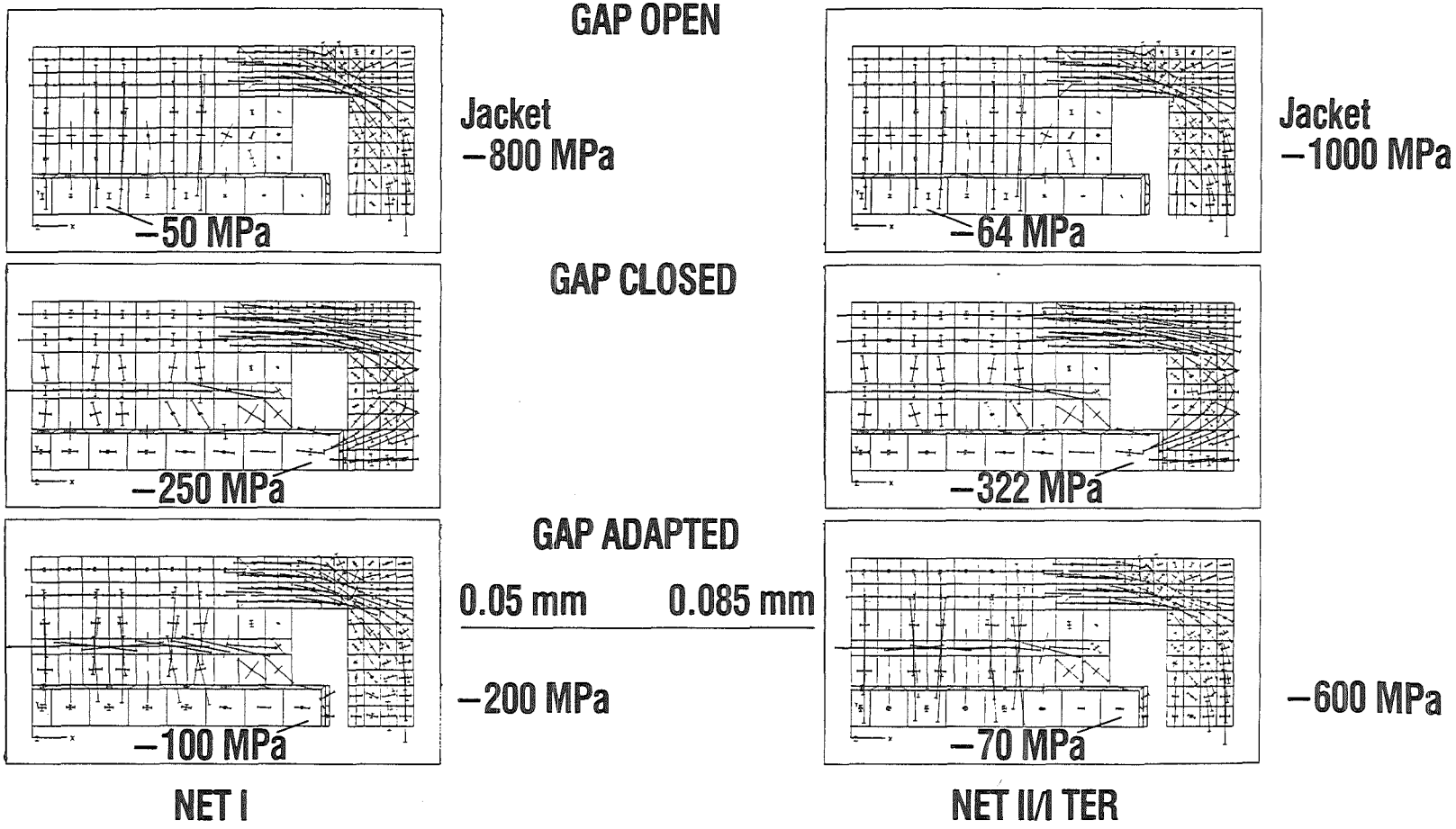

Fig. 4.1.3: Principal stresses in the electrical part of the conductor and the conductor jacket

These values are reduced to -250 MPa for a gap of 0.05 mm (load factor 1) and -600 MPa for a gap of 0.085 mm (load factor 1.3).

This parameter study demonstrates the impact of tolerances on the stress level in the superconducting core. The investigation showed that the stress level can be considerably reduced by suitably chosen gaps. A three dimensional model is necessary to investigate impacts like bending, cooldown and the longitudinal tension of the conductor under Lorentz forces. According to these results the mounting of the conductor components has to be reconsidered.

References

[4.1.1] W. Specking, W. Goldacker, R. Flükiger, Adv. Cryog. Eng. Vol 34 (1987), 569.

[4.1.2] K.-R. Leimbach Report, Ruhr-Universität Bochum, Fakultät für Bauingenieurwesen, Dec. 4, 1989.

4.2 Thermohydraulic and stability analysis

The transient stability and steady-state thermal behaviour of the KfK conductor proposed for the toroidal field coils of NET have been investigated by means of two computer codes developed and improved by the NET-Team for this issue. The optimization of the helium mass flow for different cooling conditions under external heat loads, i.e. nuclear heat is presented. The stability behaviour of the proposed conductor due to short heat pulses is investigated, too. The energy margin has been computed for different critical current densities at different critical temperatures and different mass flow rates. This results in an energy safety region for different perturbation times like plasma disruptions or burn cycle losses.

The hot spot temperature, i.e. the maximum temperature in the conductor after quench and discharge has been computed.

The AC losses which are generated by the field changes during the burn cycle as well as by a plasma disruption are calculated. For this purpose a procedure is described which allows an estimation of the average and maximum magnetic field changes during a burn cycle. This leads to the conclusion that the cycle losses are acceptable whereas the disruption losses are more than one order of magnitude too high.

4.2.1 Introduction

The main purpose of this work was to study the stability behaviour of a Nb_3Sn react-and-wind conductor proposed by KfK for the NET superconducting toroidal field coils. Since it is rather impossible to compute such a complex composite conductor with complete and accurate detail a conservative simplified model calculation has to be done with respect to the perturbation spectrum, i.e. heating rate, duration, extent, location and other effects which will occur in a plasma machine.

The first aim is to study the cooling condition of a flow channel which represents the cooling length e.g. of a pancake of a coil. This was done by means of the computer code HE-SS [4.2.1] which calculates the temperature, pressure and velocity distribution in single-phase, supercritical Helium I flowing in the cooling

channels of a conductor, considering the real properties of the helium and the effect of distributed steady state heat influxes along the flow path. Parameters are the helium mass flow rate and the cooling perimeter. An important quantity which enters into the pressure drop behaviour of a cooling channel is the friction factor which represents the geometry of the conductor and therefore is an individual number.

As a second point, the stability margin of a conductor has to be known. This will give the margin of operational safety in case of external transient energy input e.g. AC losses of the superconductor, coupling losses in the superconducting wire and in the cable, and AC losses in the cable jacket. These losses are induced by time dependent magnetic fields and currents, e.g. during ramping and pulsing, but also during discharges of the coils (time scale is some seconds). In addition external heat loads can be present, for example stickslip mechanical events (time scale is less than one millisecond). For this purpose the computer code HESTAB [4.2.2] has been written which calculates the energy margin as the maximum, sudden energy input from which the conductor will recover the superconducting state. "Sudden" means here that the time of the energy pertubation and recovery event is much shorter than the time for the heat removal by steady state convection of the cooling fluid.

As already mentioned, the time dependent change of the magnetic field leads to eddy currents in the conducting parts in the superconductor, stabilizing copper, and steel jacket which results in AC losses. The magnetic fields variations can have two origins,

- current driving of the poloidal field coils in the torus, and
- plasma disruption inside the plasma chamber.

The time scales are different by roughly three orders of magnitude e.g. during a plasma disruption the plasma current of 22 MA will drop to zero within 20 milliseconds whereas the time interval of a poloidal field coil current change is in the order of seconds. Consequently the integrated field changes will be different, too.

4.2.2 Boundary conditions

The input requirements for the calculation results presented in this sections are given in [4.2.3] and [4.2.4] and summarized in Tab. 4.2.1 as well as the main parameters of the KfK NET-TF conductor whereas a detailed list is given in Appendix A and B. The latter one also gives the data of an earlier design stage for comparison.

It should be noted that the helium channel cross section as well as the cooling perimeter has to be variable in case of the stability analysis. This will be discussed in detail in the corresponding section.

Parameter	Unit	Value
Maximum field	T	11.5
Total current of one coil	MA	9.1
Dump voltage	kV	10
Operation current	kA	16
Inlet pressure	bar	5. - 10.
Inlet temperature	K	4.2
Cooling length	m	360.
Helium mass flow	g/s	5. - 10.
A_{SC}	mm^2	69.1
A_{Cu}	mm^2	132.3
A_{He}	mm^2	63.4 - 88.6
A_{ss}	mm^2	288.9
P_{cool}	cm	7.08 - 11.28

Table 4.2.1: KfK-NET-TF conductor: Input parameters for the analysis

In Fig. 3.1 the actual cross section of the KfK NET-TF conductor is shown. The main difference compared to [4.2.18] is that the copper nickel cage which surrounded the core made of 31 Nb_3Sn strands is now reduced to two copper nickel

strips which are placed on the flat side of the core, thus protecting the superconductor from the copper stabilizer.

In the literature there is some confusion in calculating the energy perturbation per unit volume whereas the formulas for computation of AC losses represent the power loss per conductor length. Some authors only count the cross section of the superconductor plus the stabilizing copper if talking about transient stability [4.2.2]. But if one has to compute the steady state energy margin e.g. the nuclear heat the energy will be deposited also in the steel jacket as well as in the helium which serves as coolant and moves very slowly (some cm/s) through the conductor. The AC losses during the burn cycle are in between. In Tab. 4.2.2 different sources of energy perturbation and the influenced kind of material are summarized.

origin of energy perturbation	Supercon-ductor	Copper sta-bilizer	Stainless steel	Helium
Disruption losses	yes	yes	no	no
Burn cycle losses	yes	yes	yes	no
Nuclear heat	yes	yes	yes	yes

Table 4.2.2: Different origins of energy perturbation and the influenced matter

Therefore the authors made the convention that all numbers which are normalized to the conductor volume are calculated by taking into account the whole conductor cross section (including insulation).

4.2.3 Thermohydraulic analysis

One keypoint for the design of a conductor is its cooling behaviour. Measurements during the LCT experiment at ORNL, USA, have shown that the temperature difference along a cooling channel cannot be reduced below a certain limit by increasing the helium mass flow rate because the losses due to the friction inside the channel increase. On the other hand the steady state heat input is roughly independent from the coil current. Further details are given in [4.2.5].

Therefore the determination of the friction factor is very important for the computation of the temperature distribution along the cooling channel or of the

maximum temperature in the cooling channel as a function of the helium mass flow rate.

The friction factor is generally defined by the pressure drop along a cooling channel and contains the geometry of the channel.

$$\Delta p = f \frac{\rho v^2}{2} \Delta x$$

where

Δp = pressure drop,
Δx = unit length,
ρ = density of fluid,
v = velocity of fluid, and
f = friction factor.

The friction factor has to be determined experimentally because the geometry of the conductor of the "state of the art" is very complex. This will be done by measuring the pressure drop for different mass flow rates and calculation the flow velocity. In general, f will be given as a function of the Reynolds number.

For a bundle conductor, the friction factor of a single pipe is used and corrected by a factor which takes into account the non uniform channel distribution inside the conductor. This has been experimentally verified e.g. for the Westinghouse LCT coil.

For an inhomogeneous conductor of the EURATOM LCT coil type, f has been measured and transformed in an analytic expression [4.2.6]. Since the KfK-NET-TF conductor has a similar geometry, the same correlation has been used for the analysis presented in this report.

Another important quantity which influences the temperature of the helium is the external heat load. This has been also measured for the EURATOM LCT coil during the experiment at ORNL [4.2.5]. In case of NET the external heat load due to the varying magnetic fields of the poloidal coils is smaller than the so-called static losses due to nuclear heat. The latter will be concentrated at the inner layers of the inner leg of the toroidal field coils. Their numbers and locations are given in [4.2.3]. Because the conductor dimensions used there are different from those of the KfK conductor, the losses have been only estimated. The result is plotted in Fig. 4.2.1, where the nuclear heat is expressed in Watts per conductor length.

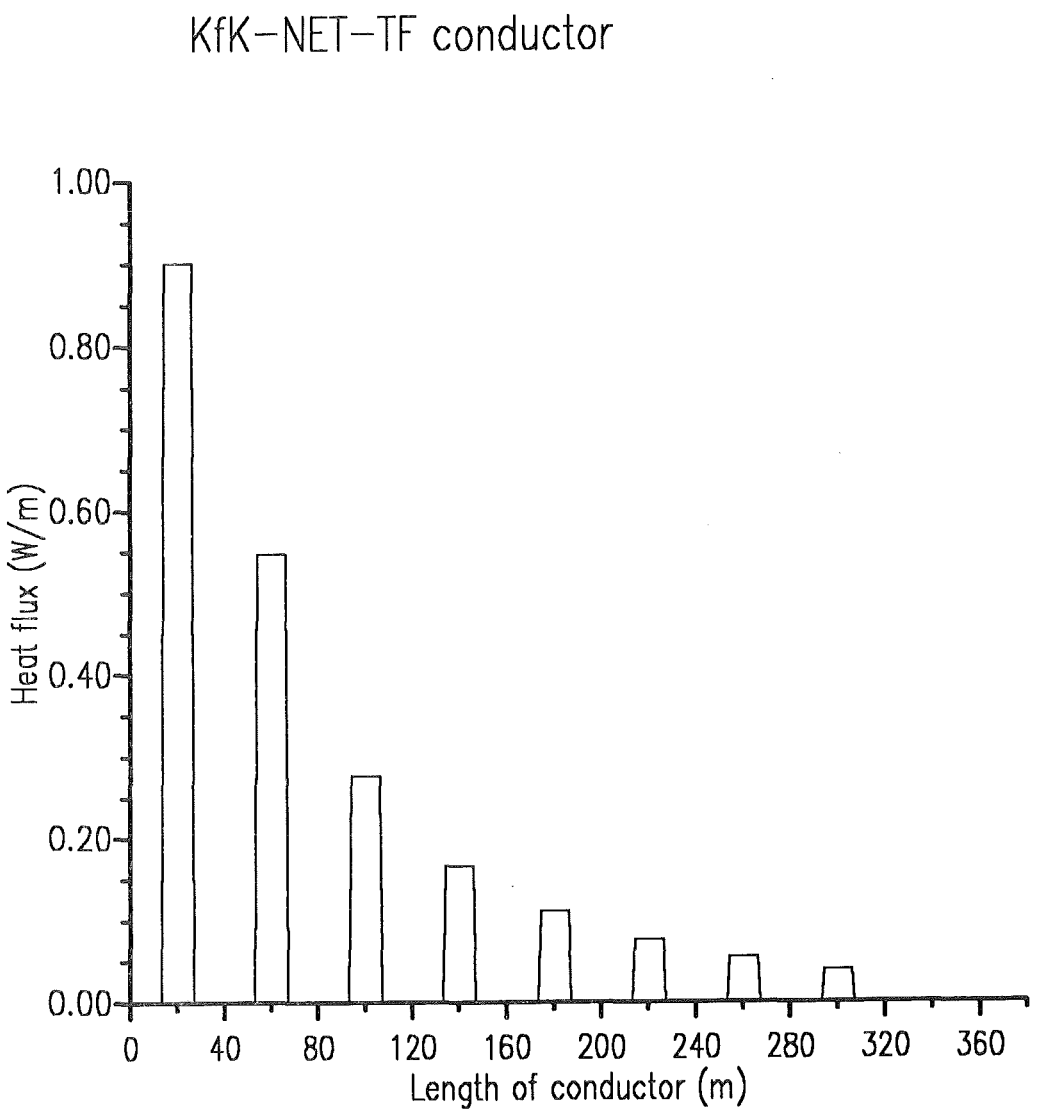

Fig. 4.2.1: Thermohydraulic analysis of the KfK-NET-TF conductor: Nuclear heat in W/m vs. conductor length.

To get the energy perturbation per volume unit, these numbers have to be multiplied by the total conductor cross section. The result is given in Tab. 4.2.3.

Layer number	Heat load	
	W/m	mJ/cm³
1	0.901	260
2	0.547	158
3	0.277	80
4	0.166	48
5	0.111	32
6	0.076	22
7	0.055	16
8	0.04	11

Table 4.2.3: Nuclear heat input for the inner layers

In the following the numbers summarized in Tab. 4.2.3 have been used in the calculation.

In Fig. 4.2.2 the temperature distribution in a heated channel is plotted for an inlet pressure of 10 bar, inlet temperature of 4.2 K, and a helium mass flow rate of 10 g/s. The effect of the step-like external heat load is clearly seen.

It should be mentioned that the minimum safety is not obviously encountered at the position of the highest magnetic field but within the coil where the temperature increase is appreciable while the field has still a high level [4.2.7]. This effect has been indicated in Fig. 4.2.3 where the so called "safety factor" s is plotted as a function of the conductor length for different mass flow rates. s is defined as

$$s = \frac{I_c(B, T)}{I_{op}} - 1$$

where

I_c = critical current at actual B, T, and

I_{op} = operational current.

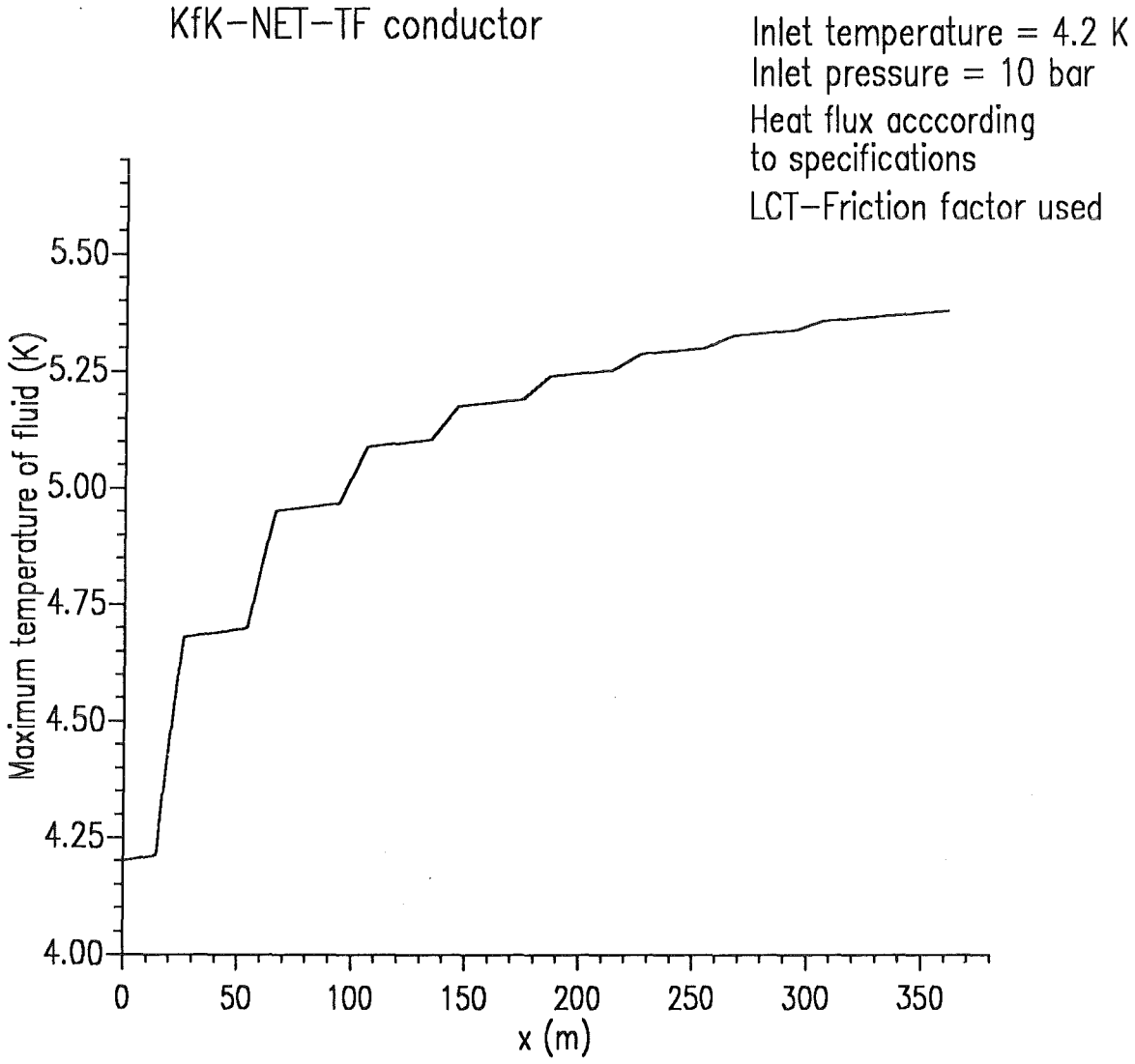

Fig. 4.2.2: Thermohydraulic analysis of the KfK-NET-TF conductor: Temperature distribution in a heated channel (inlet pressure 10 bar, inlet temperature 4.2 K, mass flow rate 7.5 g/s)

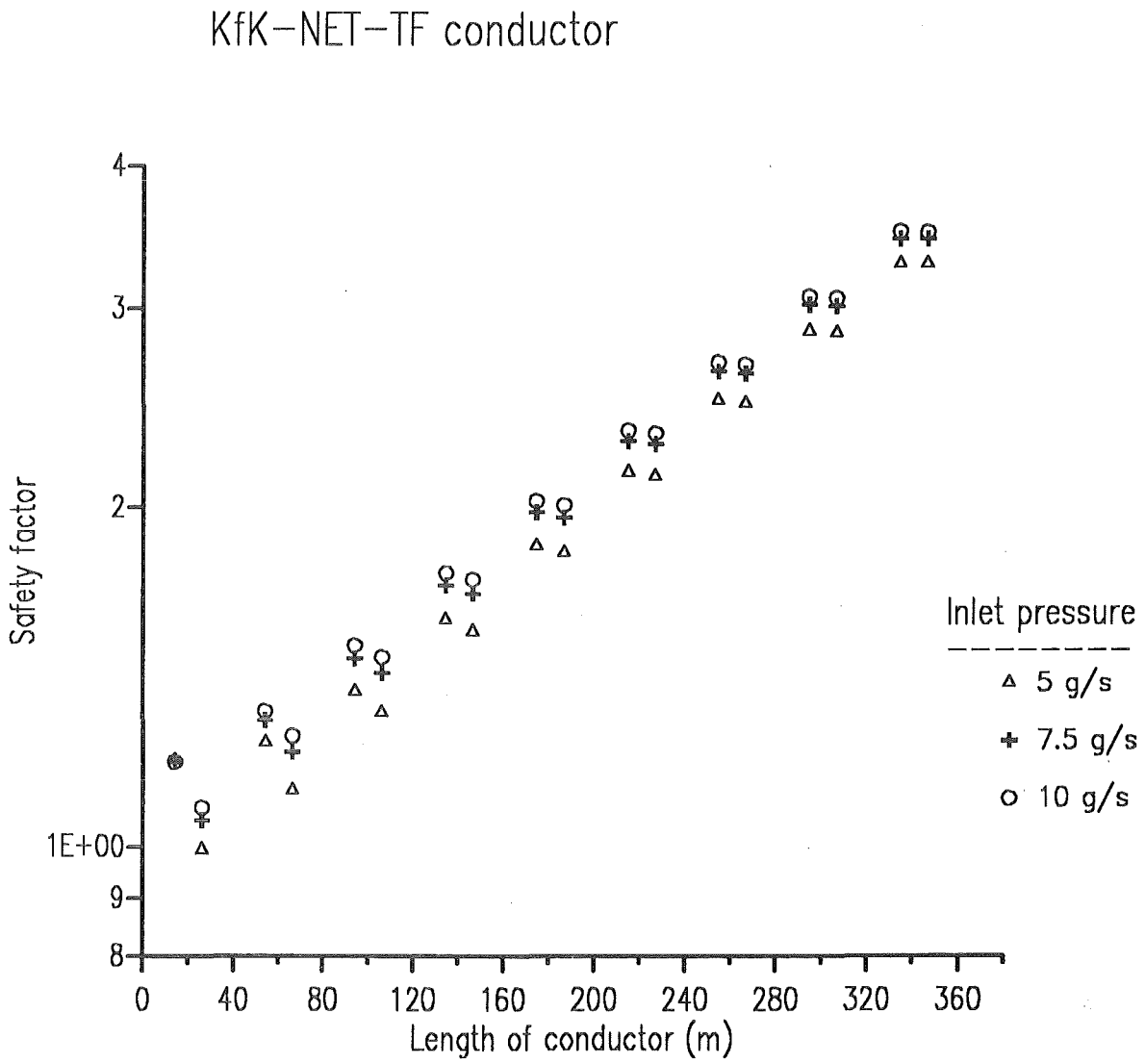

Fig. 4.2.3: Thermohydraulic analysis of the KfK-NET-TF conductor: Safety factor vs. conductor length for different mass flow rates (inlet pressure 10 bar, inlet temperature 4.2 K)

Fig. 4.2.4 shows the maximum temperature in the cooling channel as a function of the helium mass flow rate for three different inlet pressures.

Comparing the calculated curves to those measured (and computed) for the EURATOM-LCT coil [4.2.5], no minimum occurs. The reason is the high nuclear heat which results in a much higher power consumption at lower mass flow rates than the one needed for pumping. To indicate this, a calculation has also been done for 10 bar but for a much smaller nuclear heat load of 1 mW/m (= 0.36 W) (dotted line). Its shape shows the same behaviour as the one measured and calculated for the EURATOM LCT-coil [4.2.5]. The region of the current sharing temperature is also indicated. In Fig. 4.2.5 the pressure drop along the channel has been plotted.

In Tab. 4.2.4 the results of the thermohydraulic analysis have been summarized.

$\dot{m}$	Parameter	Inlet pressure		
		5 bar	7.5 bar	10 bar
$5\ \frac{g}{s}$	T_{max}	5.35 K	5.56 K	5.70 K
	Δp	0.95 bar	0.88 bar	0.84 bar
	P_{pump}	4.74 W	3.53 W	3.19 W
$7.5\ \frac{g}{s}$	T_{max}	5.05 K	5.26 K	5.38 K
	Δp	2.09 bar	1.95 bar	1.87 bar
	P_{pump}	13.64 W	11.63 W	10.46 W
$10\ \frac{g}{s}$	T_{max}	n.a.[1]	5.12 K	5.28 K
	Δp	n.a.	3.51 bar	3.33 bar
	P_{pump}	n.a.	29.01 W	25.6 W

[1]n.a. not applicable

Table 4.2.4: Maximum temperature, pressure drop Δp, and pumping power P for the KfK NET-TF conductor

It should be noted that the cooling length of 360 m is roughly one half of the total conductor length of a pancake. This comes from the fact that for a 16 kA conductor one needs more turns to get the same magnetic field. The implications on the cross section of the winding pack will not be discussed in this report.

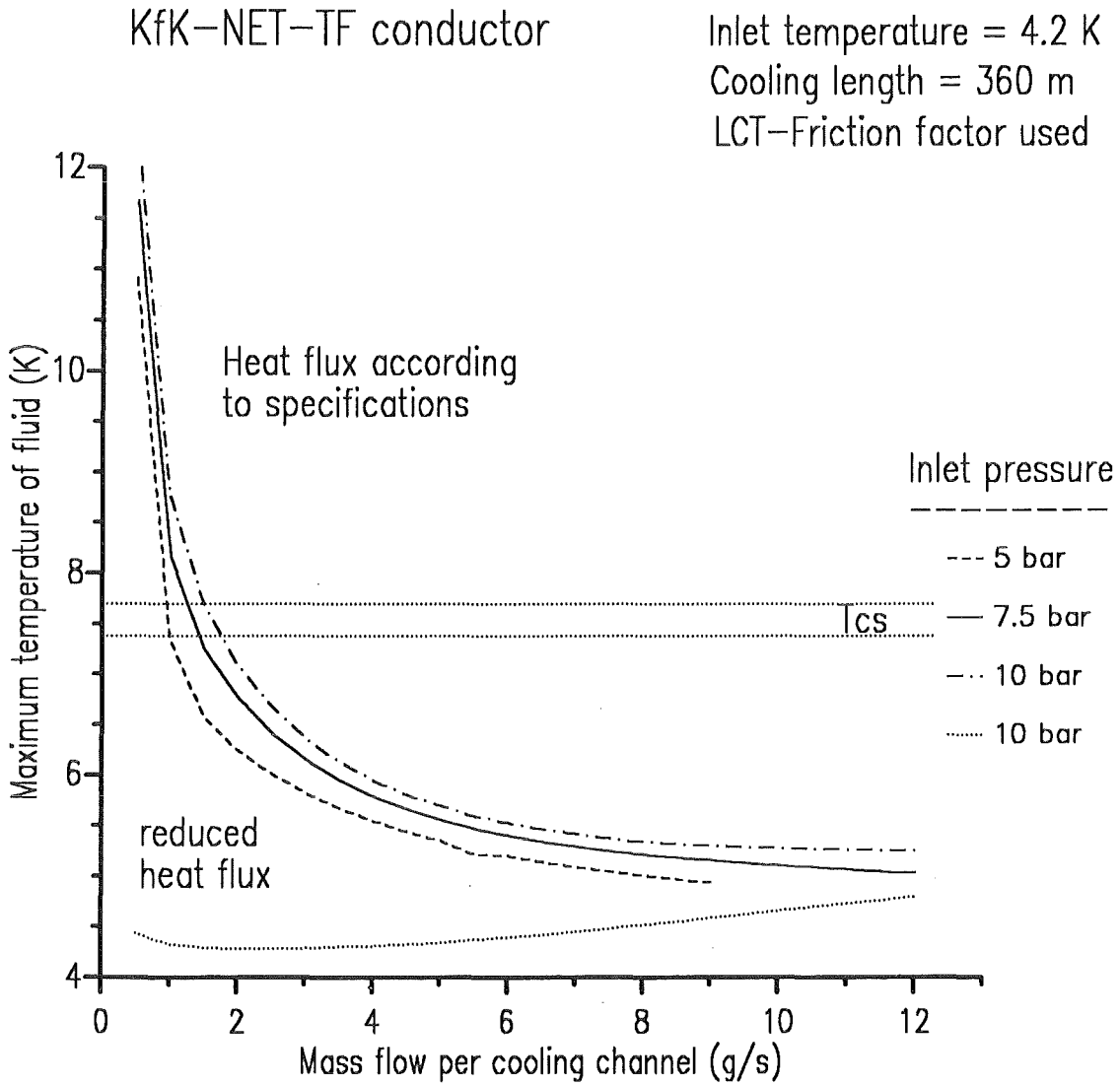

Fig. 4.2.4: Thermohydraulic analysis of the KfK-NET-TF conductor: Maximum temperature vs. helium mass flow rate for different inlet pressures. The result for a reduced heat load is also shown

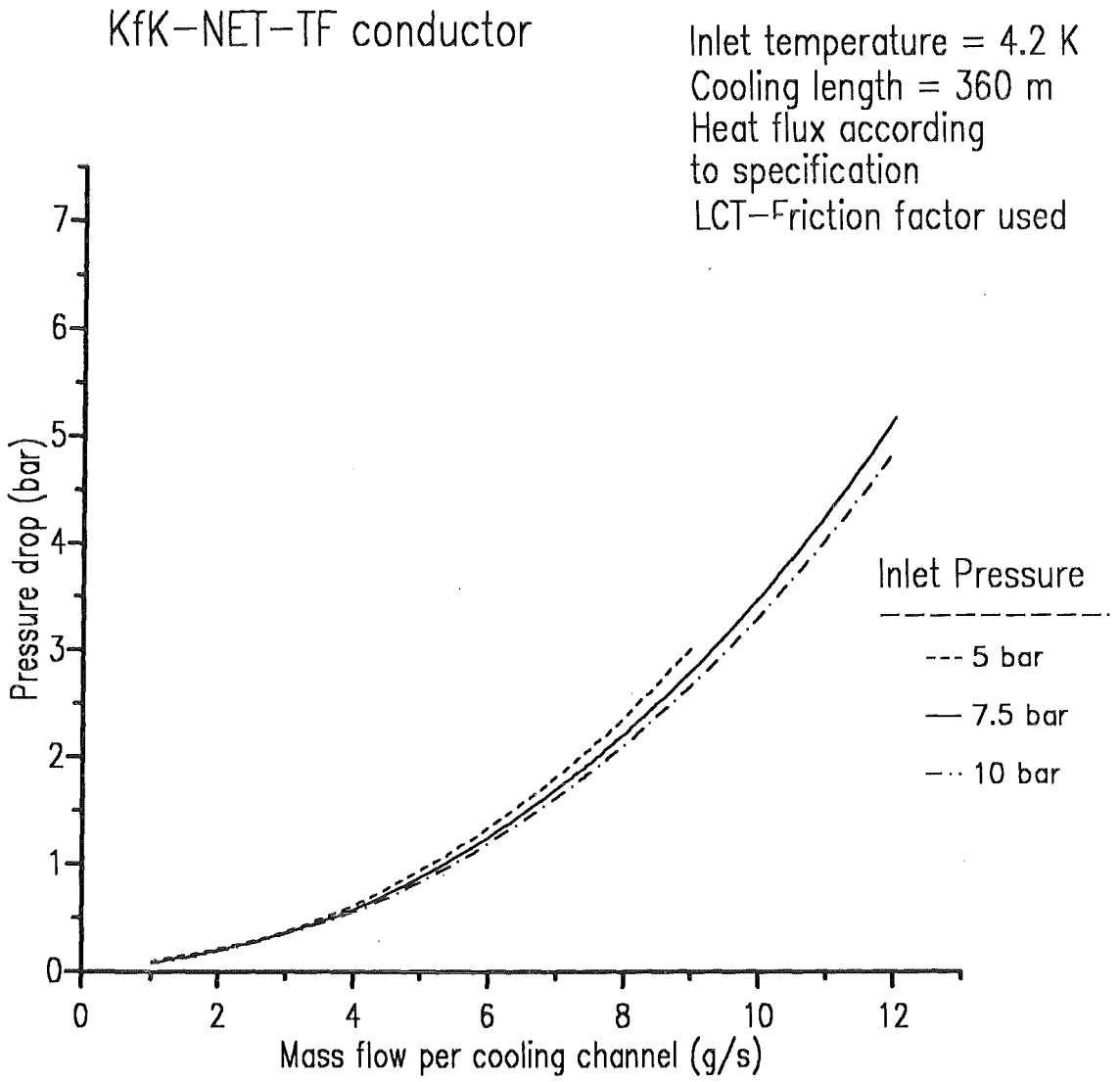

Fig. 4.2.5: Thermohydraulic analysis of the KfK-NET-TF conductor: Pressure drop vs. helium mass flow rate for different inlet pressures

The pumping power which must be available for cooling the conductor has to be compared to the heating power which results from the nuclear heat load, P_{heat} = 28.8 Watts.

4.2.4 Stability analysis

The stability analysis for the KfK-NET-TF conductor has been done by using the computer code HESTAB described in [4.2.2]. This code simulates the energy perturbation only in a so-called "zero-dimensional" model where no space coordinates and only time integration have been used. This means that the time scale of the perturbation have to be small compared to the time constant of the energy input. This should be valid in case of a bundle conductor where the superconducting area is at the "same" location as the stabilizing copper and the cooling helium. But in case of the KfK conductor where the superconducting core and the stabilizing copper as well as the cooling helium channels are spatially separated, its validity has to be proven.

For this case the thermal as well as the magnetic diffusivities have been calculated for the different materials and related to their time constants by help of their local thicknesses. The material properties have been taken from the program package PROPACK written by L. Bottura [4.2.8].

The thermal resp. magnetic diffusivities α as well as the thermal resp. the field penetration time constants τ are defined as follows [4.2.9]:

$$\alpha_{th} = \frac{k}{c_p \rho_d} \quad ,$$

$$\alpha_{mag} = \frac{\rho_e}{\mu_0} \quad ,$$

$$\tau_{th} = \frac{4}{\pi^2} \frac{d^2}{\alpha_{th}} \quad , \text{and}$$

$$\tau_{mag} = \frac{4}{\pi^2} \frac{d^2}{\alpha_{mag}}$$

where

k = thermal conductivity,

c_p = heat capacity,

ρ_d = density,

ρ_e = electrical resistivity,
μ_0 = permeability, and
d = layer thickness.

In Tab. 4.2.5 the input numbers as well as the results are presented.

Parameter	Unit	CuNi (90/10)	Copper RRR = 100	Stain-less steel tapers	Stain-less steel jacket	Helium
Magnetic field	T	11.5				
Temperature	K	4.2				
Pressure	bar	10.				
Transversal thickness	mm	0.2	1.5	0.3	2.5	0.6
Electrical resistivity	Ωm	$0.14\ 10^{-6}$	$6.5\ 10^{-10}$	$0.514\ 10^{-6}$	$0.514\ 10^{-6}$	-
Thermal conductivity	W/mK	1.504	420.	0.262	0.262	0.0233
Heat capacity	J/kgK	0.164	0.1008	2.243	2.243	2908.5
Density	kg/m^3	9000	9000	7890	7890	151.33
Magnetic diffusivity	m^2/s	0.111	$5.17\ 10^{-4}$	0.409	0.409	-
Thermal diffusivity	m^2/s	$1.02\ 10^{-3}$	0.463	$1.48\ 10^{-5}$	$1.48\ 10^{-5}$	$5.3\ 10^{-8}$
Field penetration time constant	ms	$0.36\ 10^{-3}$	4.35	$2.2\ 10^{-4}$	0.015	-
Thermal time constant	ms	$3.92\ 10^{-2}$	$4.86\ 10^{-3}$	6.1	422.	$6.8\ 10^{3}$

Table 4.2.5: Input parameters and results for diffusivity calculations

The conclusion is that the outer part of the stabilizer unit does not contribute to the energy margin because it is thermally insulated by the glue film and become the twist length of the copper profiles is half a meter. In addition the heat transfer area between the stainless steel tapers and the helium does not count because the heat resistivity of the stainless steel tapers is much higher than that one corresponding to the heat transfer from the copper or the copper nickel foil and the helium, respectively.

For pulse time constants below one second the diffusion time τ_θ of helium has to be considered. This leads to a time dependent heat transfer coefficient h(t). In addition for $\tau_\theta < 100$ ms the enthalpy of the stainless steel tapers has to be neglected. The stainless steel jacket has been neglected, too, except for the static limit.

In Tab. 4.2.6 the helium channel area and the heat transfer area, respectively, are given for various perturbation times. The use of the stainless steel tapers and the jacket, respectively, has been taken into account, too.

Parameter	Unit	Value					
Perturbation time	ms	1	10	100	1000	static	limit
Helium channel area	cm^2	0.634	0.634	0.634	0.634	0.634	0.886
Heat transfer area	$\frac{cm^2}{cm}$	7.08	7.08	7.08	7.08	7.08	11.28
Stainless steel tapers		no	no	yes	yes	yes	yes
Stainless steel jacket		no	no	no	no	no	yes

Table 4.2.6: Helium channel area and heat transfer area used for stability calculations

For small perturbation time constants the diffusion time of the materials have to be considered, i.e. a transient heat transfer coefficient has been used for the calculations. In HESTAB the following two parametrizations have been used:

$$h_t = \frac{\sqrt{\alpha}}{k} \sqrt{\frac{1}{\pi t}} ,$$

$$h_t = \frac{1}{2} \frac{\sqrt{\alpha}}{k} \sqrt{\frac{\pi}{t}} .$$

where
α = thermal diffusivity,
k = thermal conductivity, and
t = time.

The first equation results from the one-dimensional diffusion equation with fixed conductor temperature as boundary condition [4.2.10], [4.2.11]. For a constant heat flux density a different heat transfer coefficient has been obtained [4.2.11], [4.2.12] which leads to the second equation.

The difference between the two expressions is roughly a factor of two. Therefore the results of two calculations have been compared in terms of energy margin.

As an example Fig. 4.2.6 shows h(t) as a function of time for a heat pulse of 0.78 J/m for 10 ms time duration and a mass flow rate of 7.5 g/s. Its shape is step-like i.e. for $t \leq 10$ ms a constant heat has been used for $T > 10$ ms no heating occurs. For all calculations described in the next section such pulse shape has been used.

Fig. 4.2.7 shows the corresponding temperatures of the wire and the helium, respectively, as a function of time. The wire temperature rises fast above the critical temperature of the superconductor and drops again due to the large amount of enthalpy of the cooling helium (recovery).

In Fig. 4.2.8 the energy margin of the conductor is plotted vs. the perturbation time for both parametrizations of the transient heat transfer coefficient.

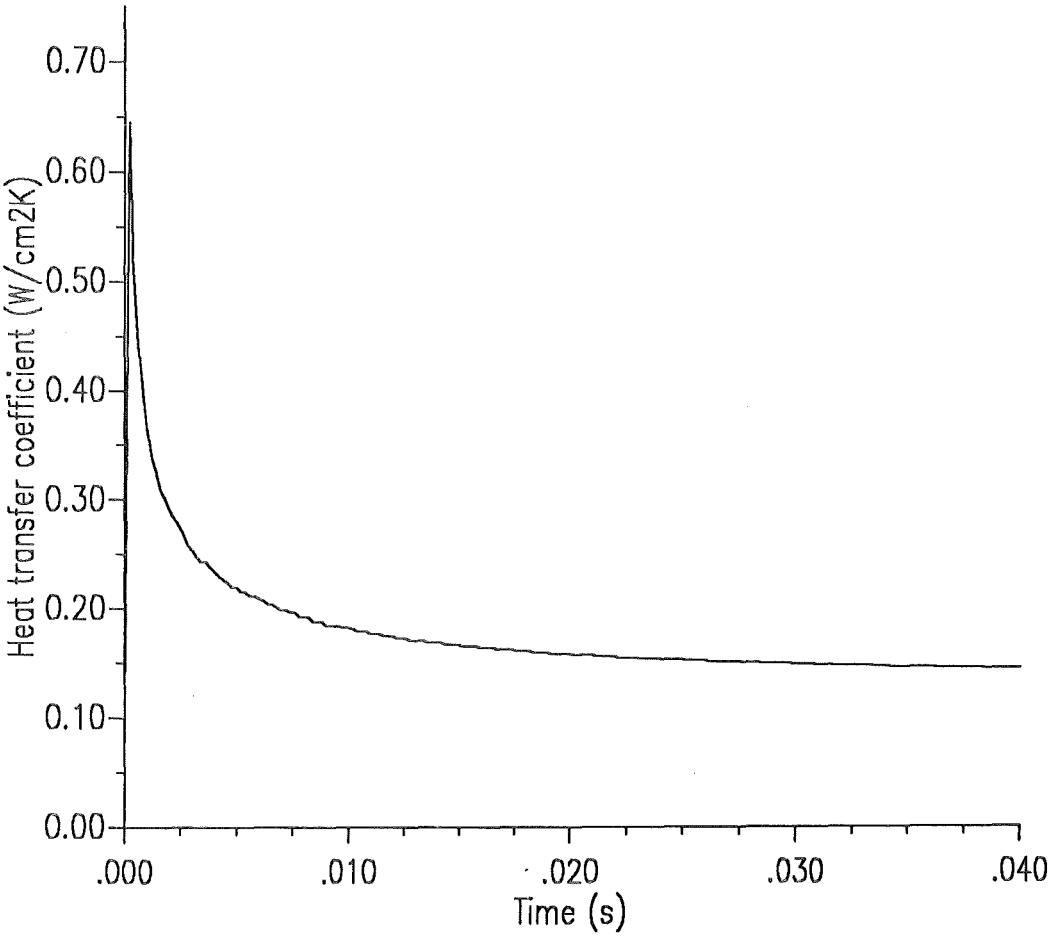

Fig. 4.2.6: Stability analysis of the KfK-NET-TF conductor: Transient heat transfer coefficient vs. time (mass flow rate = 7.5 g/s)

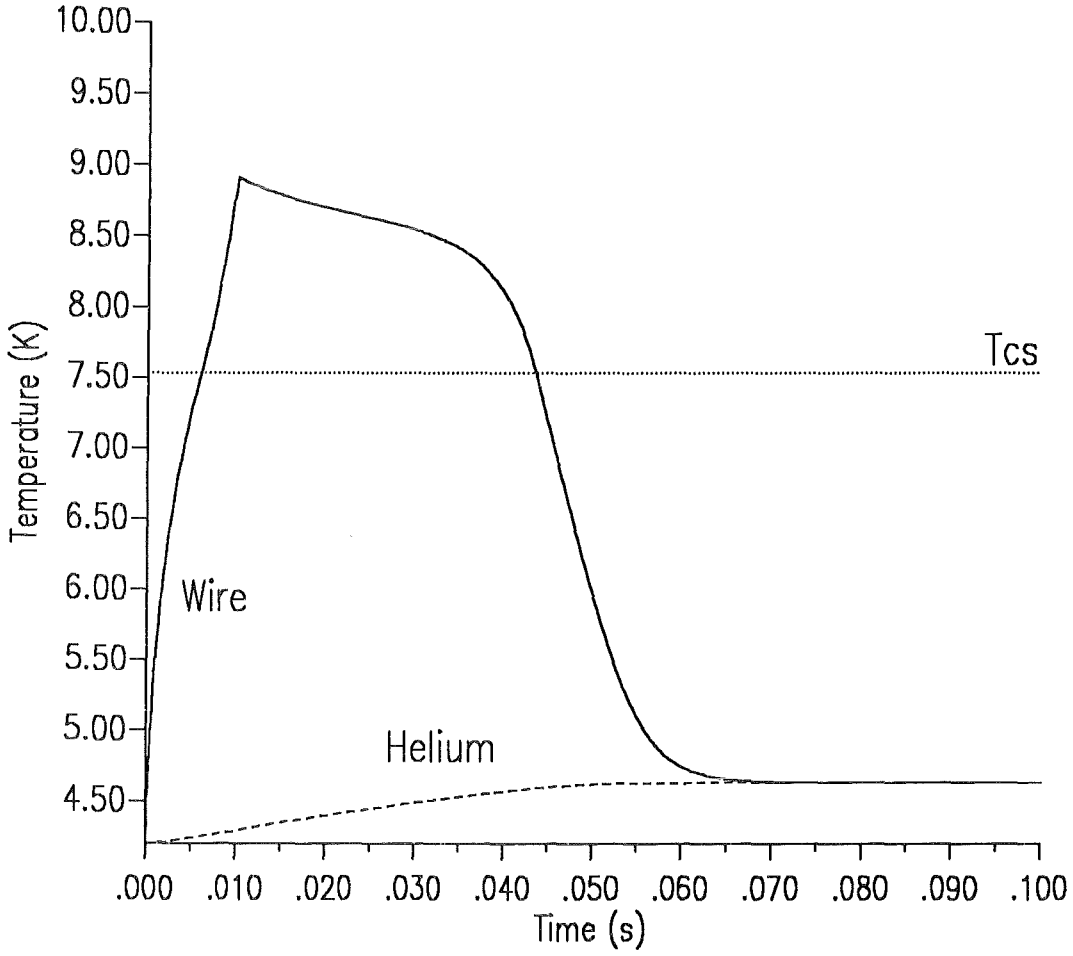

Fig. 4.2.7: Stability analysis of the KfK-NET-TF conductor: Wire resp. helium temperature vs. time for an energy perturbation of 35 mJ/cm^3 (mass flow rate = 7.5 g/s)

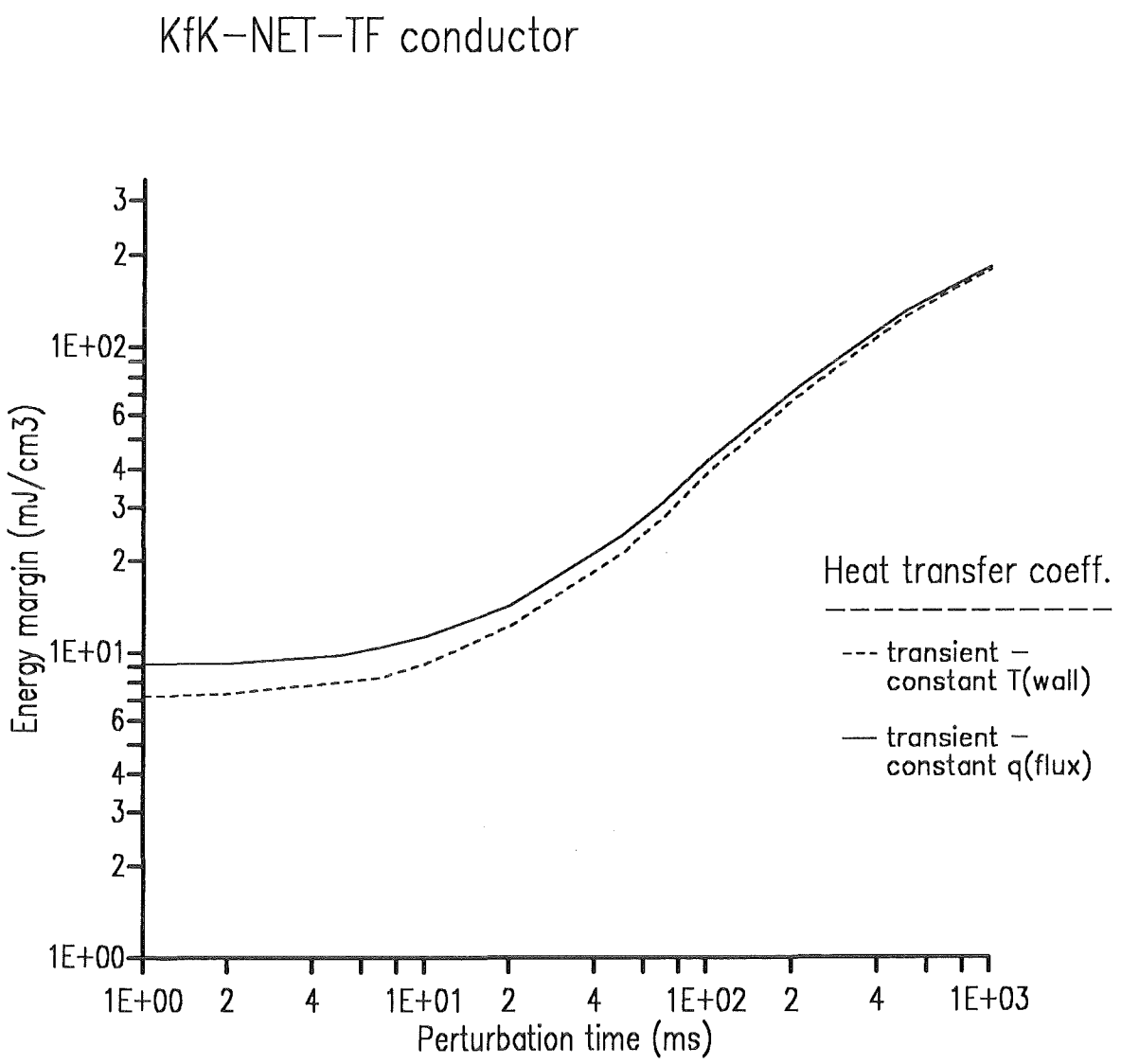

Fig. 4.2.8: Stability analysis of the KfK-NET-TF conductor: Energy margin vs. time constant of heat pulse for steady state (dotted line) and two different transient heat transfer coefficients. The solid line corresponds to the one obtained for constant heat flux, the dashed line to the one obtained for constant conductor temperature. Inlet pressure 10 bar, inlet temperature 4.2 K, helium mass flow rate 7.5 g/s

The results of the stability analysis can be summarized as follows:

The study was made for the nominal current of 16 kA i.e. a non copper current density of 232 A/mm2. First the energy perturbation has been computed as a function of the operational current for different pulse time durations. Fig. 4.2.9 shows the results. For comparison the energy margin is plotted as a function of the ratio of the operational current to the critical current. The maximum available energy margin is also shown (here the enthalpy of the stainless steel jacket has been taken into account). At the nominal current of roughly 30 % of the critical current the energy margin drops rapidly which indicates that the heat transfer area is too small to transfer the heat produced in the wire to the cooling helium.

More important is the fact that the energy margin is not well defined i.e. small changes for example in current will lead to large changes in energy input. Therefore only a region of energy margin can be given.

Then a parameter study has been made to cover the stability region of the conductor. Three parameters have been varied, i.e.

- helium mass flow and inlet pressure,
- critical temperature of superconductor, and
- critical current of superconductor.

A weak dependence of the energy margin by the mass flow rate is expected because the time independent heat transfer coefficient depends on the Nusselt number for which the validity of the Dittus-Boelter equation has been assumed:

$$Nu = 0.023\, Re^{0.8} Pr^{0.4} \propto \dot{m}^{0.8},$$

where
Nu = Nusselt number,
Re = Reynolds number,
Pr = Prandtl number, and
$\dot{m}$ = mass flow rate.

In Fig. 4.2.10 the energy margin is plotted vs. the perturbation time for an operation at nominal current.

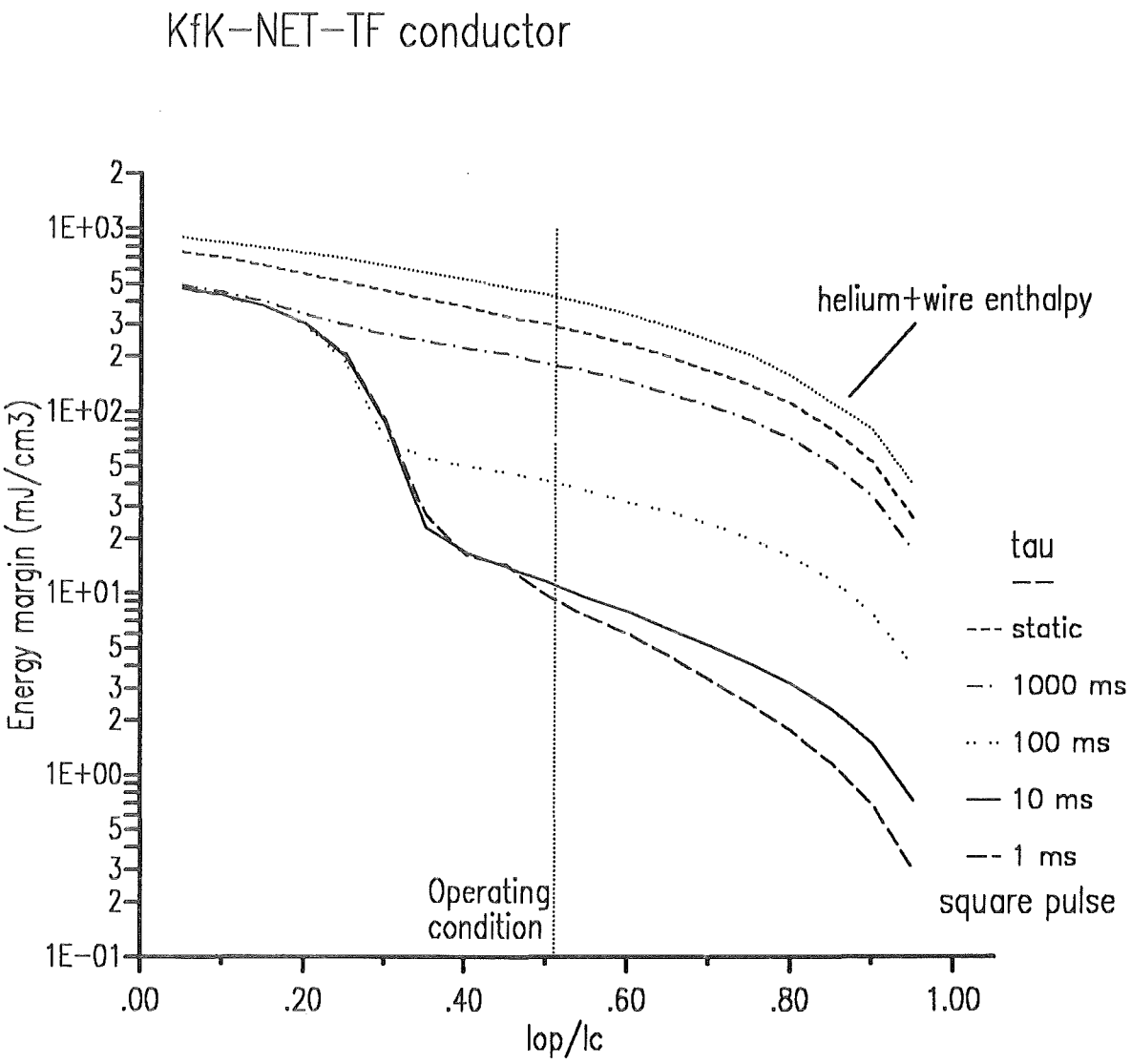

Fig. 4.2.9: Stability analysis of the KfK-NET-TF conductor: Energy margin for different transient heat pulses (square, pulse length τ = 1, 10, 100, and 1000 ms). The maximum available energy margin has been plotted, too. Transient heat transfer coefficient was assumend. Inlet pressure 10 bar, inlet temperature 4.2. K, helium mass flow rate 7.5 g/s

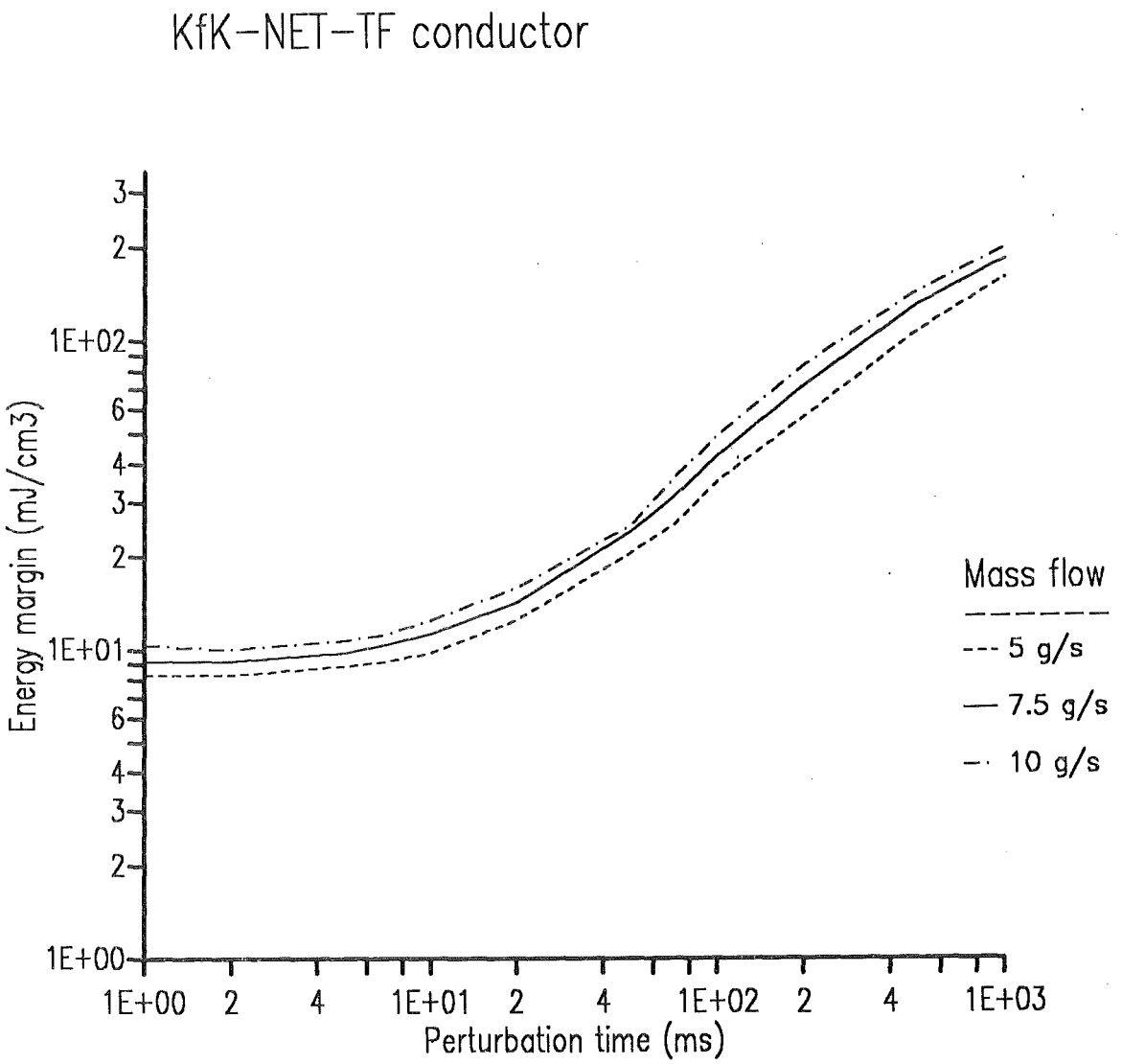

Fig. 4.2.10: Stability analysis of the KfK-NET-TF conductor: Energy margin vs. time constant of heat pulse for different mass flow rates at nominal current. Transient heat transfer coefficient was assumed. Inlet pressure 10 bar, inlet temperature 4.2 K

A slight uncertainty in the knowledge of the critical temperature leads to the decision to vary this parameter, too. In Fig. 4.2.11 the result of the calculation is shown in the same way as for the mass flow rate parameter change for at least three numbers of T_c. The range of energy margin is the same as for the last item although for the steady state case the difference is only of the order of 5 %. The hope in getting a 50 % higher current density by artificial pinning [4.2.13] is the reason why calculations were done for two different values of j_c. A degradation of 30 % due to transverse and longitudinal stress has been assumed, too. The result is shown in Fig. 4.2.12. The increase of the critical current density by 50 % leads to an enhancement of the energy margin by roughly 70 % while for the steady state case it's a factor of 2.2. Assuming no glue between the stainless steel tapers of the stabilizer also its outer part can be used in the stability calculations, too, but only for longer perturbation times because the diffusivity time of the stainless steel has to be considered. The result is shown in Fig. 4.2.13. The enhancement would be in the order of 5 %.

Tab. 4.2.7 contains the main results of the stability analysis for the parameter study.

Parameter	Unit	KfK-TF conductor				
T_{in}	K	4.2				
p_{in}	bar	10.				
$\dot{m}$	g/s	7.5				10.
j_c (11.5 T / 4.2 K) 30 % degradation	kA/cm²	30.3	45.4 50 % higher j_c			
I_{op}/I_c	%	76.4	51			
T_c	K	11.	11.34	11.	10.7	11.
T_{cs}	K	5.85	7.7	7.53	7.38	7.53
Heat transfer coefficient (steady state)	$\frac{W}{cm^2K}$	0.097				0.122
ΔE time duration:	$\frac{mJ}{cm^3}$					
1 ms		4.5	10.6	9.2	8.2	10.4
10 ms		4.9	12.2	11.3	10.2	12.5
100 ms		19.8	45.9	42.5	40.4	49.6
1000 ms		84.1	192	182.9	174	197.2
limit		137	308.	293	279	320

Table 4.2.7: Results of stability calculations of the KfK-NET-TF conductor: The energy margin is computed in terms of the total conductor cross section.

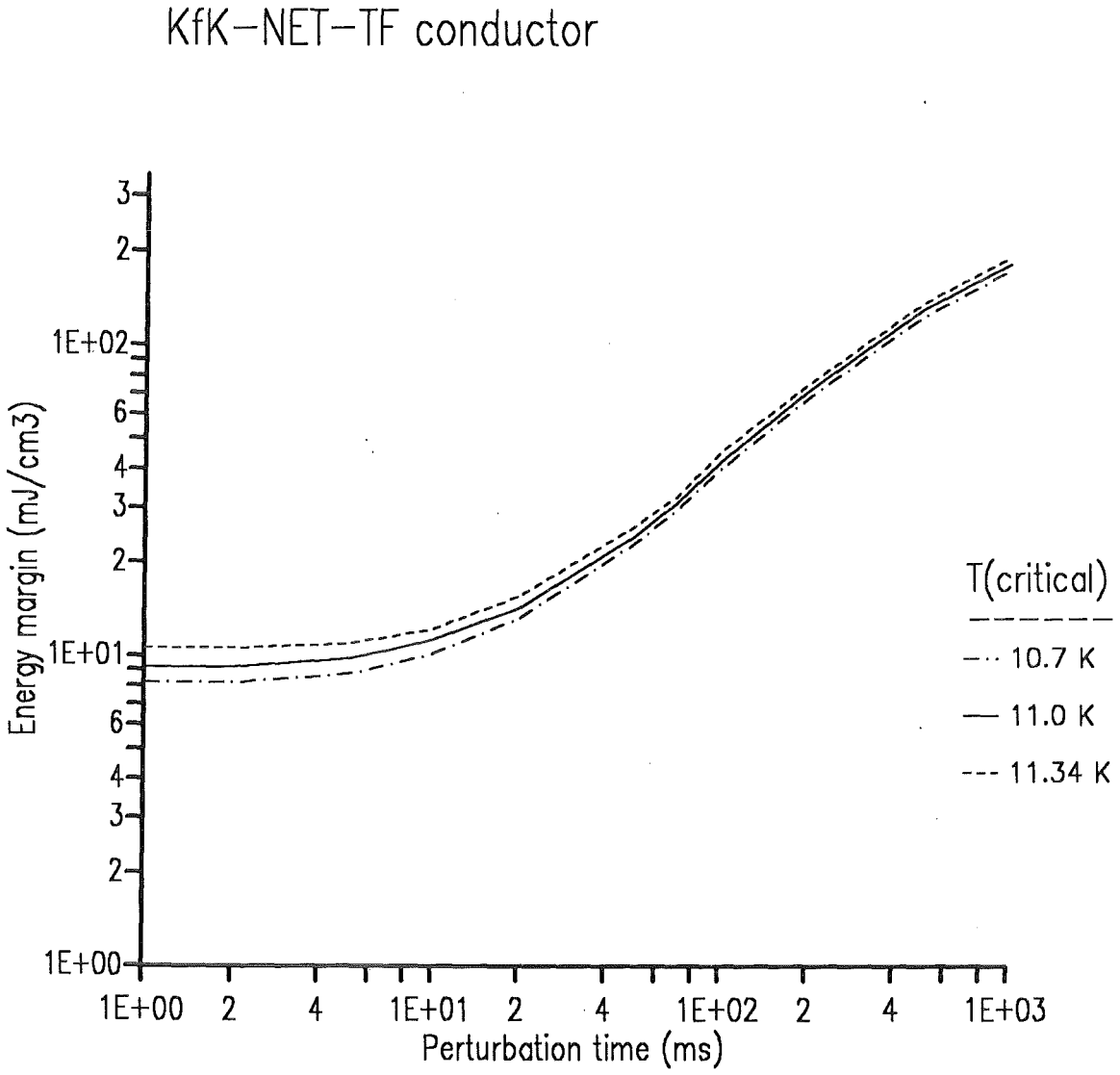

Fig. 4.2.11: Stability analysis of the KfK-NET-TF conductor: Energy margin vs. time constant of heat pulse for different critical temperatures at nominal current. Transient heat transfer coefficient was assumed. Inlet pressure 10 bar, inlet temperature 4.2 K, helium mass flow rate 7.5 g/s

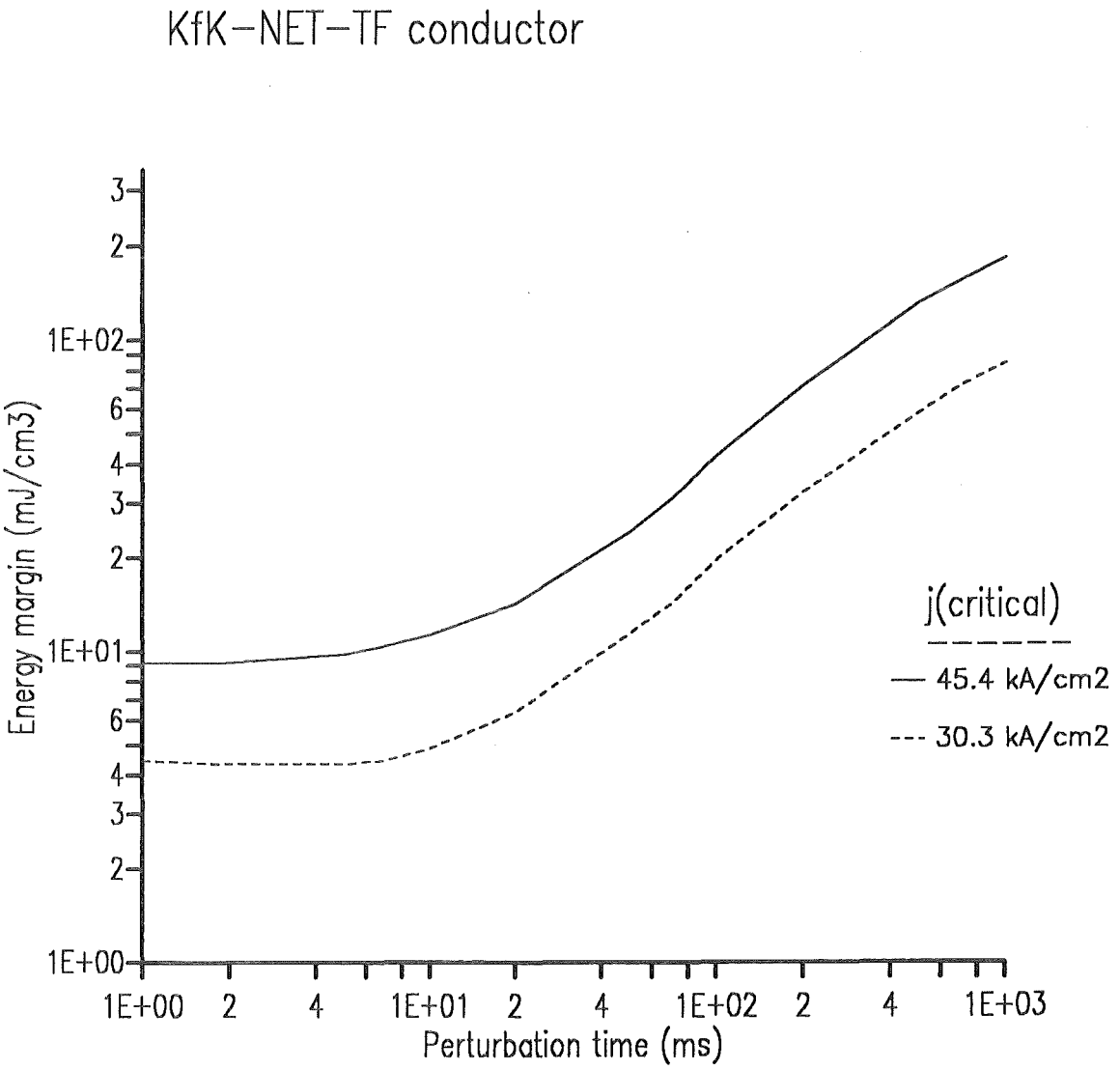

Fig. 4.2.12: Stability analysis of the KfK-NET-TF conductor: Energy margin vs. time constant of heat pulse for different critical currents at nominal current. Transient heat transfer coefficient was assumed. Inlet pressure 10 bar, inlet temperature 4.2 K, helium mass flow rate 7.5 g/s

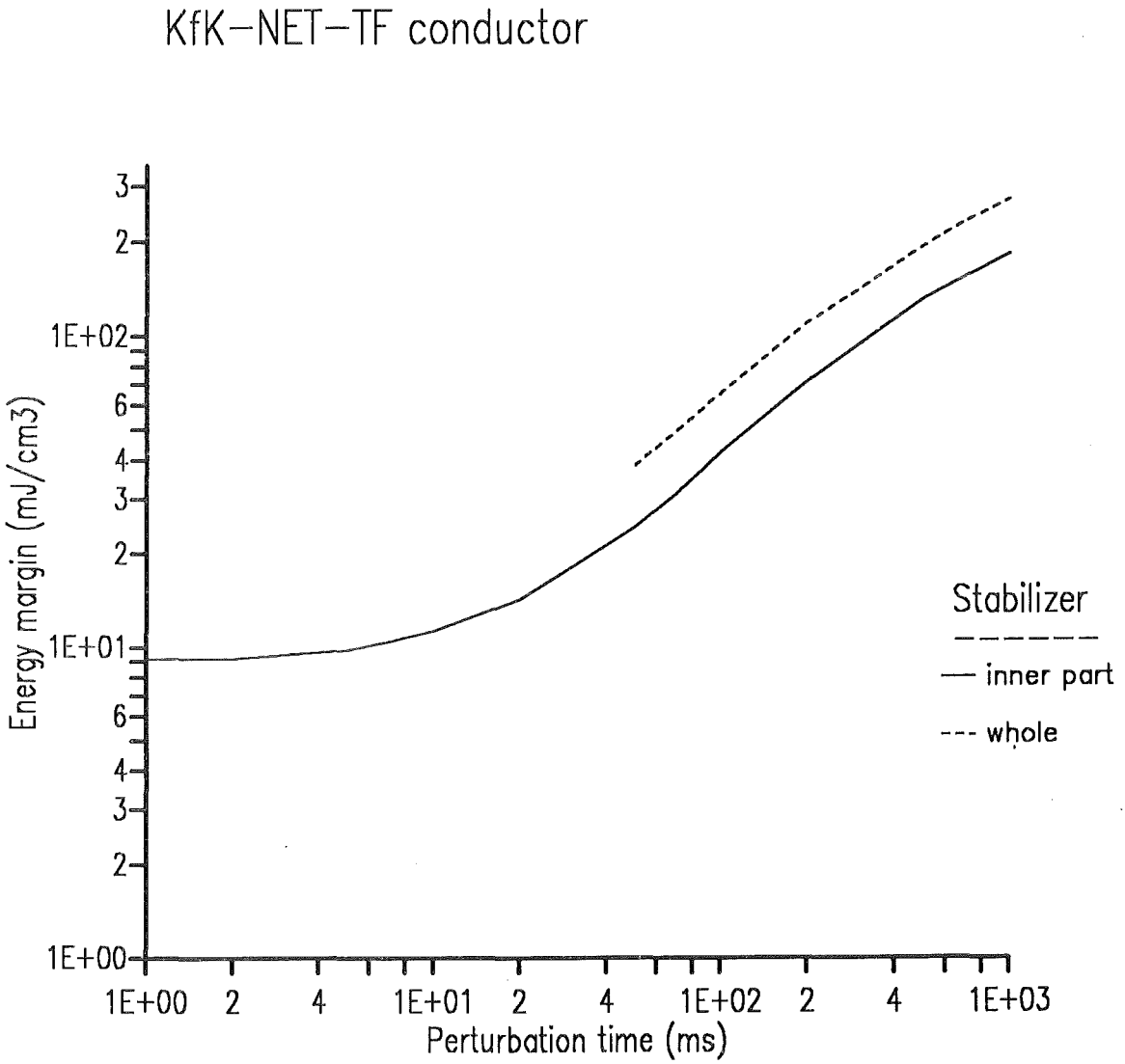

Fig. 4.2.13: Stability analysis of the KfK-NET-TF conductor: Energy margin vs. time constant of heat pulse for the inner part (solid line) and the whole (dashed line) stabilizer unit. Inlet pressure 10 bar, inlet temperature 4.2 K. helium mass flow rate 7.5 g/s

4.2.5 Calculation of the hot spot temperature

The hot spot temperature i.e. the maximum temperature in the conductor after quench and safety discharge is mainly determined by the heat capacity of the different materials e.g. superconductor, copper, steel, helium, and by the discharge time constant τ_D. The latter one is defined by

$$\tau_D = \frac{2Q}{IU},$$

where

Q = total energy of the coil,

I = coil current, and

U = dump voltage

and limited by the maximum dump voltage which can be tolerated in the circuit. In case of NET requirements and boundary conditions of the KfK conductor, one gets $\tau_D = 29$ s.

Using this number, the maximum temperature has been calculated by means of a computer code [4.2.14]. The program calculates the temperature increase in the conductor due to the ohmic power as a function of time by taking into account the enthalpy and heat capacity of the conductor components e.g. superconductor, copper, steel, and helium. The ohmic power will be calculated by using the actual current which will be exponentially reduced by using the dump time constant.

The result is shown in Fig. 4.2.14 where the temperature of the conductor is plotted as a funtion of time. The maximum temperature is computed to be 135 K , well below the specified number of 150 K.

4.2.6 Calculation of AC losses

After the determination of the (theoretically) available energy margin of the KfK-NET-TF conductor, the second part of this report concerns the estimation of the AC losses which occur in a Tokamak machine like NET. As already mentioned in the introduction two major sources lead to eddy currents which produce the losses i.e. magnetic field changes during burn cycle and fast field changes during a

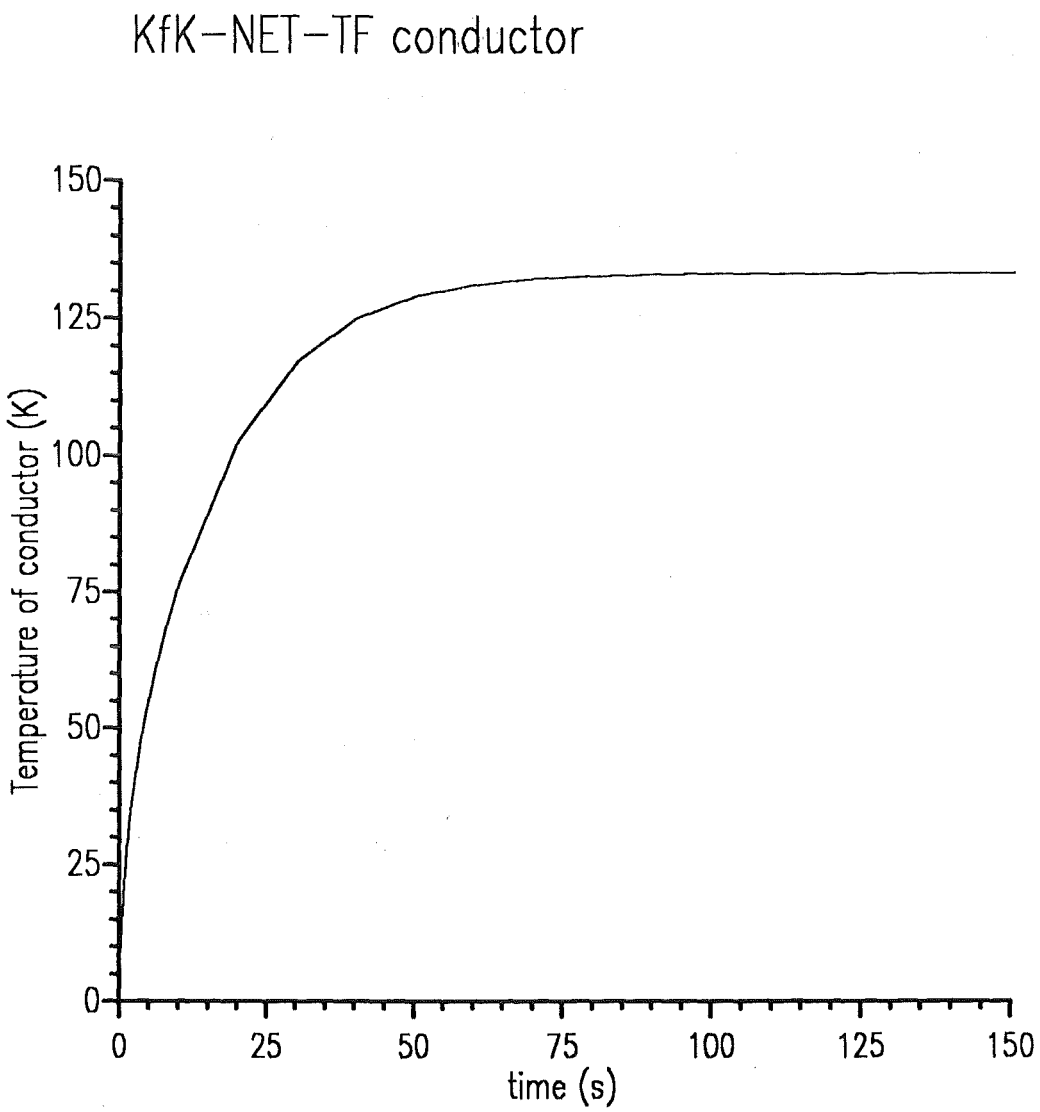

Fig. 4.2.14: Hot spot criterion: Temperature of the KfK-NET-TF conductor vs. time

plasma disruption. Both items are declared as a normal operation by the NET team [4.2.3].

The AC losses in a superconductor can be separated into

- hysteresis losses in the superconducting filaments,
- coupling losses between the superconducting strands, inside the superconducting cable core, and in the copper stabilizers, and
- eddy current losses in the copper stabilizers and in the stainless steel jacket.

Although former calculations e.g. for the LCT project [4.2.5] showed big discrepancies between the calculations and the measurements some estimations about the (possible order of magnitude of the) losses have to be done.

Big effort has been done in the past to get analytic expressions especially for the coupling losses because they are geometry dependent. A summary of equations valid for conductors of the KfK type are given in [4.2.16] and are also listed in [4.2.17].

A second uncertainty is related to the transverse resistivities of the single parts of the conductor which enter the AC loss formulas inversely linear.

In Table 4.2.13 all parameters are listed which are needed for the computation e.g. geometry and resistivity. The numbers are partly taken from [4.2.20] and [4.2.17].

A remark should be given to the nomenclature used in the following: a coordinate system is used which has its x-coordinate in radial direction, its z-coordinate in axial direction, and its y-coordinate in longitudinal direction with respect to the conductor. This means that the y-direction is the parallel one, whereas the x- and z-directions are the transversal ones.

4.2.6.1 Disruption losses

The most severe energy (and force) perturbation in a tokamak is the plasma disruption. In case of NET the plasma current of 22 MA will decay to zero within 20 ms. This leads to enormous forces acting on the vacuum vessel but also to large field changes in the toroidal field coils. In Tab. 4.2.8 the integral field changes are listed [4.2.3], they will be used for the computations of the resulting AC losses.

Parameter	Unit	transverse	parallel
$\int_0^{100ms} \dot{B} dt$	T	0.5	2
$\int_0^{100ms} \dot{B}^2 dt$	T^2/s	5	50
$\Delta\dot{B}$	T/s	20	40

Table 4.2.8: Integral fields and field changes for a plasma disruption

Using the equations given in [Ref. 4.2.17] the hysteresis, coupling, and eddy current losses for the transverse and parallel components have been calculated. The detailed results are shown in Tab. 4.2.9. For the coupling losses due to a parallel field change no reliable formulas are available. Nevertheless these losses have been estimated by calculating the change of the magnetic energy in the enclosed volume of the stabilizer unit resp. the superconducting core. This is allowed because the time scale of the disruption is small and the energy which will be decoupled from the system should be small, too.

$$\frac{Q}{L} = \frac{1}{2\mu_0} \int\int \dot{B}^2 dt\, dA$$

For the stabilizer the glue between the stainless steel tapers have been used for the enclosed area whereas for the superconducting core the value of the (now missing) copper nickel barrier has been chosen.

Note that the energy perturbations are normalized to the total conductor cross section.

Comparing this number to the available energy margin presented in section 4.2.4 the AC losses due to a plasma disruption are more than one order of magnitude too high, i.e. the conductor will quench.

4.2.6.2 Cycle losses

For calculating the AC losses induced by magnetic field changes during a burn cycle the same formulas can be used as in the last section. For this purpose the integral fields and field changes have to be known.

Parameter	W/m	mJ/cm³
Single strand perpendicular coupling losses	16.9	2.44
Single strand parallel coupling losses	missing	
Flat cable perpendicular coupling losses	252.3	36.4
Flat cable parallel coupling losses	103.0	14.9
Stabilizer perpendicular coupling losses	630.6	91.
Stabilizer parallel coupling losses	353.7	51.0
Stabilizer perpendicular eddy current losses	5.1	0.73
Stabilizer parallel eddy current losses	0.3	0.05
Jacket perpendicular eddy current losses	4.0	0.57
Jacket parallel eddy current losses	6.2	0.89
Perpendicular hysteresis losses	1.2	0.17
Parallel hysteresis losses	5.4	0.78
Total losses	1379	199

Table 4.2.9: Results on AC losses in the KfK-NET-TF conductor during a plasma disruption

The NET team has given the burn cycle losses for a fictive conductor in [4.2.4] but not the field changes. Therefore it has been decided to calculate the magnetic fields as a function of the coordinates specified in the last section for three representative parts of the whole winding pack and then to get the average field numbers. Fig. 4.2.15 shows the cross section of the winding pack at the inner leg at the medium plane, the three "representative coils" are also seen.

In Figs. 4.2.16 and 4.2.17 the magnetic field as a funtion of the axial coordinate is plotted at two radial positions of the winding cross section where the "representative coils" are located. If translated in terms of AC losses, the result can be seen in Figs. 4.8 and 4.9 of [4.2.17]. The conclusion is that the changes of losses in axial direction are very small while those in radial direction are a factor of three different. This is the reason why the procedure described above is valid.

The calculations have been done by means of the computer code EFFI [4.2.19] for each time step and the corresponding currents in the poloidal field coils. The scenario of the burn cycle up to end-of-burn (EOB) is given in Table 4.2.14.

It has been assumed that the field changes during the time between EOB and the end of the cycle (t = 500 s) are not larger than those from start-up to EOB.

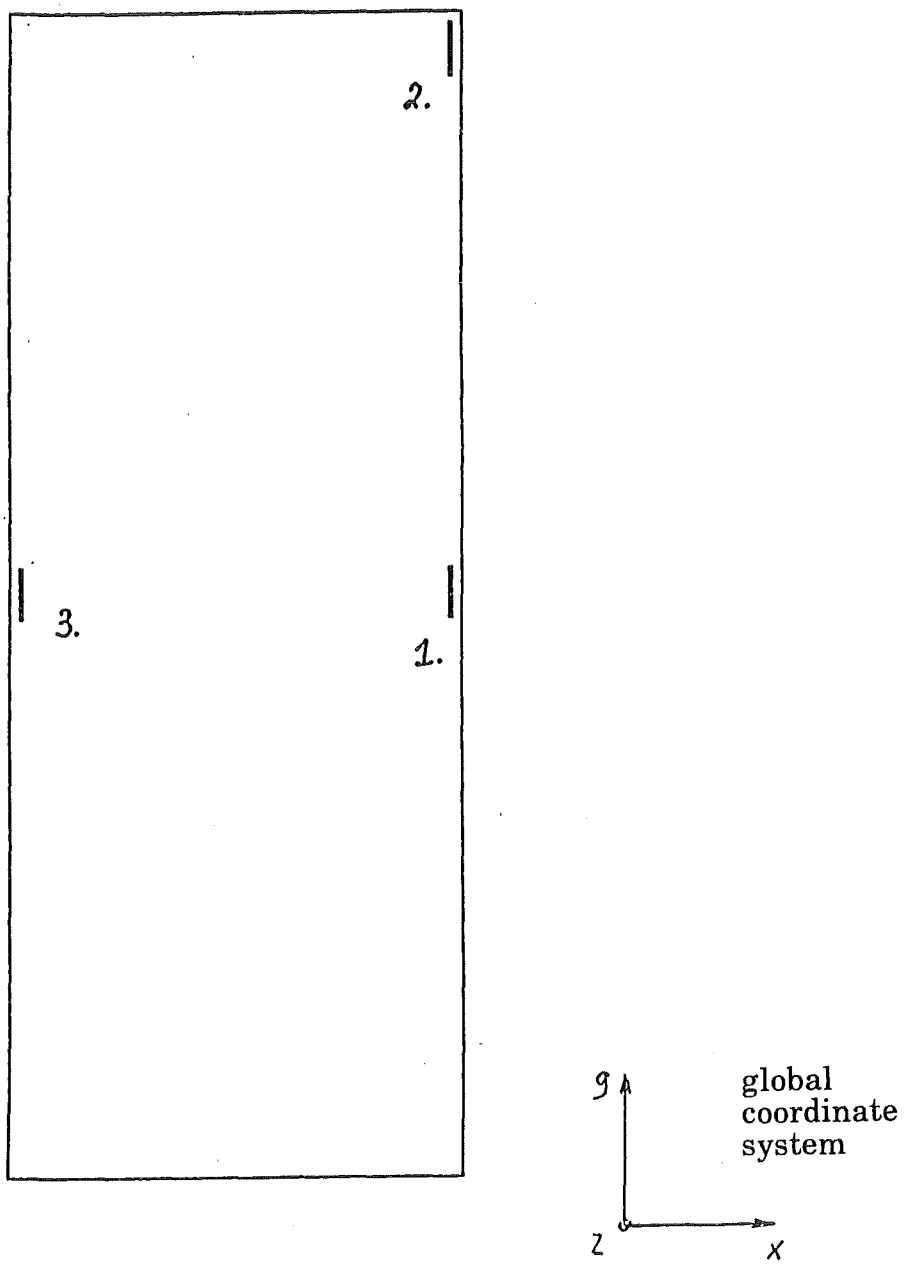

Fig. 4.2.15: Winding pack cross section: Inner leg of the toroidal field coil. The numbers 1,2, and 3 denote the "representative coils"

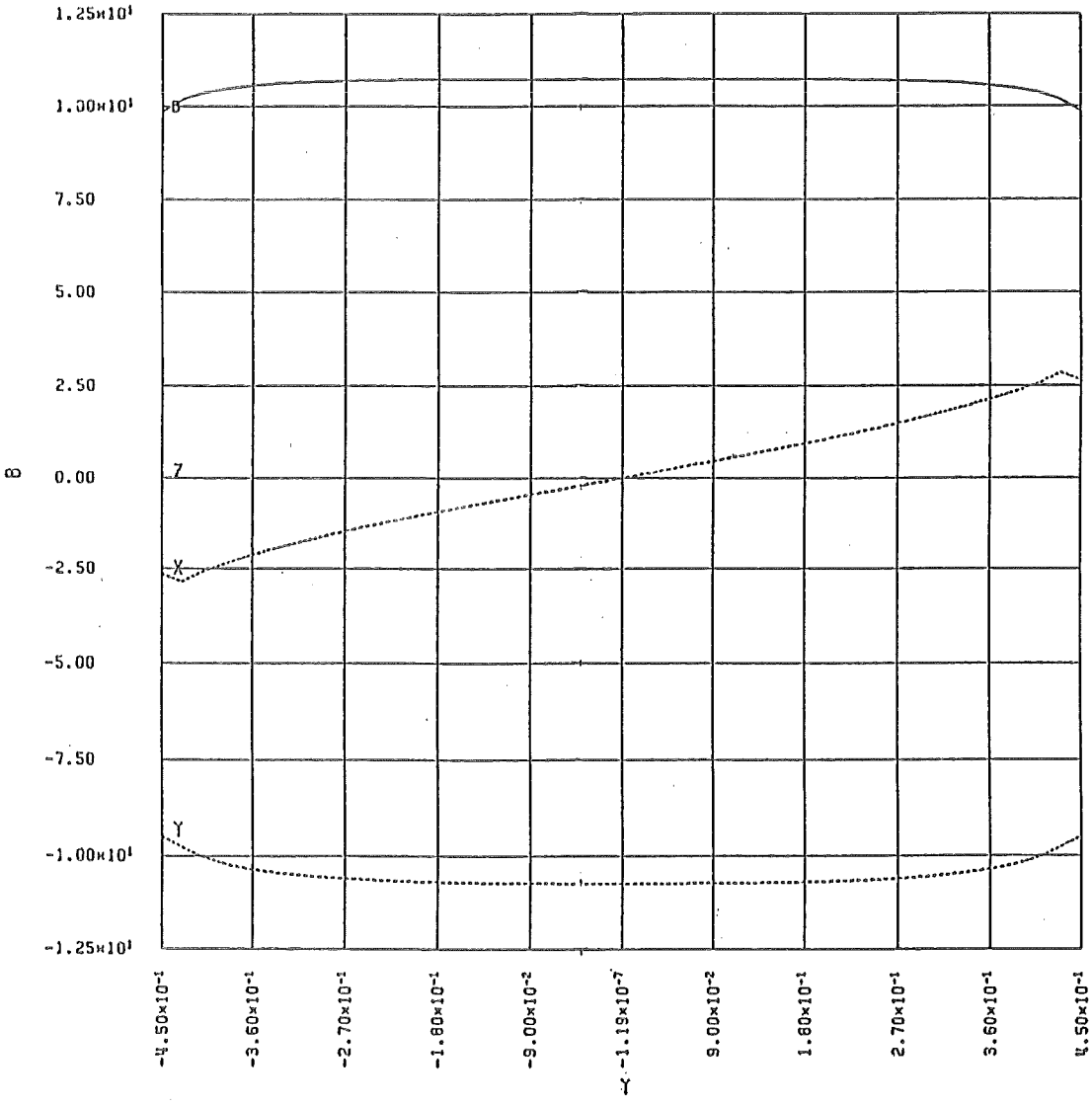

Fig. 4.2.16: Magnetic field vs. y at radial position 1

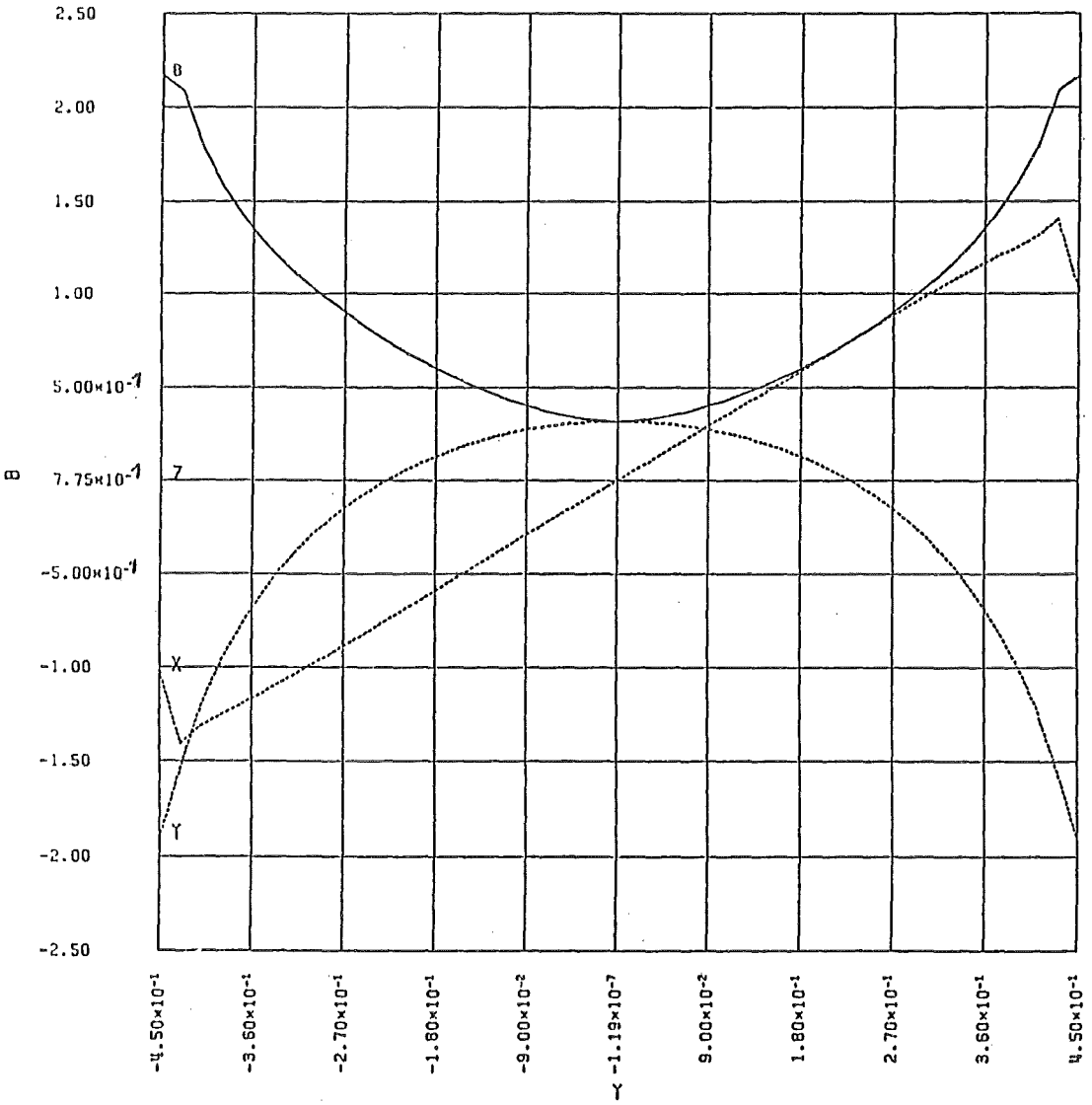

Fig. 4.2.17: Magnetic field vs. y at radial position 3

Therefore the total cycle losses should not be more than a factor of two larger than the calculated numbers.

The field vectors for 384 grid points in azimuthal direction for all three "representative coils" were stored for each of the 11 time steps. Then the ΔB were calculated. From the single $\Delta B / \Delta t$ and $(\Delta B / \Delta t)^2$ the maximum and average numbers in each direction were computed i.e.

$$\max_j \left[\sum_{i=1}^{384} \left| \frac{\Delta B_k}{\Delta t} \right|_i \right] ,$$

$$\max_j \left[\sum_{i=1}^{384} \left| \frac{\Delta B_k}{\Delta t} \right|_i^2 \right] ,$$

$$j = 1, 2, \ldots 10$$

$$\frac{1}{L} \sum_{j=1}^{10} \sum_{i=1}^{384} \left| \frac{\Delta B_k}{\Delta t} \right|_i \Delta t_j \Delta l_i \quad , \quad \text{and}$$

$$\frac{1}{L} \sum_{j=1}^{10} \sum_{i=1}^{384} \left| \frac{\Delta B_k}{\Delta t} \right|_i^2 \Delta t_j \Delta l_i \quad ,$$

$$k = x, \; y, \; z$$

where

$$L = \sum_{j=1}^{10} \Delta l_j \; .$$

In Tab. 4.2.10 the average ΔB and $\Delta \dot{B}$ are listed for the three "representative coils" resp. the maximum numbers of them.

Parameter	Unit	Maximum	Average		
			Pos. 1	Pos. 2	Pos. 3
B_{max}	T	3.34	8.41	7.93	2.2
$\int \dot{B} dt$ for					
x-coor.[2]	T	0.135	0.0365	1.009	1.238
y-coor.[3]		0.018	0.0010	1.298	1.427
z-coor.[3]		0.010	0.0	0.110	0.0
$\int \dot{B}^2 dt$ for					
x-coor.[2]	T^2/s	0.117	0.024	0.023	0.037
y-coor.[3]		0.054	0.031	0.031	0.038
z-coor.[3]		0.0	0.0	0.001	0.0

2 $\Delta t = 0.5$ s

3 $\Delta t = 0.1$ s

Table 4.2.10: Integral fields and field changes for a burn cycle: Maximum and average numbers are shown.

4.2.6.3 Calculation of AC losses

The average and maximum field changes were used to compute the AC losses in the conductor. For the longitudinal coupling losses of the core resp. the stabilizer, the method used estimating the disruption losses can not be applied here because of the completely different time scale. The energy which will be decoupled from the system can not be neglected. But there is no way to quantify it, therefore they are neglected in the calculations. In Tab. 4.2.11 the results are presented.

The average power losses in the coil can be calculated by multiplying the power loss per conductor length with the total length e.g. the mean length per turn times the number of turns. This results in

$$P_{total} = 230 \text{ W}.$$

4.2.7 Comparison and conclusion

Comparing the AC losses during a plasma disruption with those during a burn cycle, two conclusions can be drawn:

Parameter	Average losses time duration: 290 s		Peak losses time duration: 0.5/0.1 s	
	mW/m	mJ/cm³	W/m	mJ/cm³
Single strand perpendicular coupling losses	0.035	0.015	0.024	0.018
Single strand parallel coupling losses	missing			
Flat cable perpendicular coupling losses	0.53	0.22	0.368	0.265
Flat cable parallel coupling losses	missing			
Stabilizer perpendicular coupling losses	1.33	0.56	0.919	0.663
Stabilizer parallel coupling losses	missing			
Stabilizer perpendicular eddy current losses	0.02	0.009	0.016	0.04
Stabilizer parallel eddy current losses	0.0	0.0	0.0	0.0
Jacket perpendicular eddy current losses	0.72	0.003	0.06	0.004
Jacket parallel eddy current losses	0.0	0.0	0.0	0.0
Perpendicular hysteresis losses	2.58	1.08	0.191	0.138
Parallel hysteresis losses	5.35	2.24	0.193	0.028
Total losses	10	4.1	1.72	1.13

Table 4.2.11: Results on AC losses in the KfK-NET-TF conductor during a burn cycle: The losses from EOB to end of cycle are not taken into account.

1. for a plasma disruption the main contribution comes from the core resp. the stabilizer coupling losses whereas for the burn cycle it is coming from the hysteresis losses.

2. for both types of energy perturbation, the eddy current losses in the jacket resp. in the copper bars of the stabilizers are negligible (less than two percent). The same counts for the single strand coupling losses.

The different energy perturbations are summarized in Tab. 4.2.12 and compared to the numbers given in Tab. 4.2.7.

origin of energy	Energy margin	Energy input	Averaged power input	
	mJ/cm3	mJ/cm3	W/m	W
1. Burn cycle	137 - 320	4.1	0.01	230
2. Nuclear heat	137 - 320	260	0.9	390
3. Plasma disruption	6.4 - 15.9	199	1379	?

Table 4.2.12: Comparison between energy margin and energy input for different perturbation origins

It should be mentioned that all results presented in this report are "singularities" i.e. the transient and steady state energy inputs are not present at the same time. If taking into account the case that a plasma disruption occurs while nuclear heat also takes place - which is the real case - and if assuming that the energy deposition due to the disruption will occur at the same location as the nuclear heat, the temperature of the conductor at the position of high magnetic field will be higher than assumed in the calculations i.e. higher than 4.2 K due to the steady state nuclear heat. This results in a reduced energy margin.

The basic inputs for stability analysis and ac losses are summarized in Tables 4.2.12a to 4.2.12e and in Table 4.2.13. A time dependent development of the poloidal field coil scenario up to end-of-burn is summarized in Table 4.2.14.

Table 4.2.12a-e: Basic Inputs for Stability Analysis

a) Superconductor

Parameter	Unit	1986 [4.2.20]	1988 [4.2.18]	1990
Material		Nb_3Sn	Nb_3Sn	Nb_3Sn
Cross sectional area	cm^2	0.613	0.691	0.691
Note: without 23 % Cu and 4 % Ta [4.2.20] without 17 % Cu and 6 % Ta [4.2.18]				
Density	g/cm^3	7.85	8.9	8.9
Critical current density at 12 T / 4.2 K / $\varepsilon = 0$	kA/cm^2	40	39.6	51.5
Critical temperature at 12 T	K	11.	11.	11.
Critical current at 12 T / 4.2 K / $\varepsilon = 0.3$ %	kA	24	22	31.4
Note: to 1988 : VAC NS-10000(0.8) - 20 %degradation to 1990 : J_c increased by 50 % [4.2.13] - 30 % degradation				

b) Stabilizer

Parameter	Unit	1986	1988	1990
Cross sectional area	cm^2	1.791	1.170	1.170
Cross sectional area of Cu in strand	cm^2		0.153	0.153
Density	g/cm^3	8.89	8.9	8.9

c) Jacket

Parameter	Unit	1986	1988	1990
Cross sectional area	cm^2	2.345	2.586	2.586
Cross sectional area of SS tapes of stabilizers	cm^2		0.303	0.303
Density	g/cm^3	7.89	7.89	7.89

d) Helium

Parameter	Unit	1986	1988	1990
Cross sectional area	cm^2	1.076	0.537	0.634
Wetted perimeter	cm	20.16	18.52	19.58
Hydraulic diameter	cm	0.213	0.170	0.181
Heat transfer area (copper + strands + SS tapers)	$\frac{cm^2}{cm}$	16.44	11.02	11.28
Initial temperature	K	4.2	4.2	4.2
Initial pressure	atm	10.	6.	10.

e) Operation conditions

Parameter	Unit	1986	1988	1990
Magnetic field	T	12.	12.	11.5
Current	kA	16	16	16
I/I_c	%	67	73	51

Table 4.2.13: Input parameters for the AC loss calculation

Parameter	Unit	Value
Single strand coupling		
External radius of stage n	m	$0.95\ 10^{-3}$
Radius of inner region of stage n	m	$0.5\ 10^{-3}$
Cross section of stage n subcable	m^2	$2.9\ 10^{-6}$
Resistivity of inner region of stage n	Ωm	$3.2\ 10^{-8}$
Resistivity of outer region of stage n	Ωm	$1.96\ 10^{-8}$
Twist pitch length of stage n	m	0.050
Weighting factor (N-1)/N		1
Number of strands		31
Flat cable stage coupling losses		
Axial outer dimension of cable	m	$29.8\ 10^{-3}$
Axial inner dimension of cable	m	$27.88\ 10^{-3}$
Radial outer dimension of cable	m	$4\ 10^{-3}$
Radial inner dimension of cable	m	$2.08\ 10^{-3}$
Twist pitch of cables	m	0.3
Effective transverse resistivity	Ωm	$4.33\ 10^{-8}$
Stabilizer coupling losses		
Axial outer dimension of stabilizer unit	m	$30.6\ 10^{-3}$
Axial inner dimension of stabilizer unit	m	$28\ 10^{-3}$
Radial outer dimension of stabilizer unit	m	$3.75\ 10^{-3}$
Radial inner dimension of stabilizer unit	m	$2.25\ 10^{-3}$
Mean distance between two stabilizers	m	$7.75\ 10^{-3}$
Twist pitch of cables	m	0.5
Effective transverse resistivity	Ωm	$9.5\ 10^{-8}$
Effective longitudinal resistivity	Ωm	$1.4\ 10^{-7}$
Number of stabilizer units		2
Stabilizer eddy current losses		
Axial dimension of stabilizer unit	m	$2.6\ 10^{-3}$
Radial dimension of stabilizer unit	m	$1.5\ 10^{-3}$
Effective transverse resistivity	Ωm	$6.5\ 10^{-10}$
Number of stabilizer elements		30

Parameter	Unit	Value
Steel jacket eddy current losses		
Axial outer dimension of stabilizer unit	m	$37\ 10^{-3}$
Axial inner dimension of stabilizer unit	m	$30.6\ 10^{-3}$
Radial outer dimension of stabilizer unit	m	$16.5\ 10^{-3}$
Radial inner dimension of stabilizer unit	m	$11.5\ 10^{-3}$
Effective transverse resistivity	Ωm	$5.3\ 10^{-7}$
Hysteresis losses		
Operational current density	A/m^2	$784\ 10^{6}$
Effective filament radius	m	$2.5\ 10^{-6}$
Cross section of superconductor	m^2	$6.91\ 10^{-5}$

Table 4.2.14: Poloidal field coil scenario up to end-of-burn (EOB)

Time (s)	0.0	0.1	0.6	3.0	10.0	20.0	28.0	44.0	70.0	90.0	290.0
Plasma (MA)	0.0	0.0	0.5 LIM	2.0 LIM	5.0 LIM	10.0 LIM	10.0 DN	15.0 DN	22.0 SOFT	22.0 SOB	22.0 EOB
PF1 (MA)	20.411	20.09	19.32	17.31	13.53	5.24	4.56	-3.78	16.79	-17.87	-22.30
PF2 (MA)	20.411	20.09	19.32	17.31	13.53	5.24	4.56	-3.78	16.79	-17.87	-22.30
PF3 (MA)	20.411	20.09	18.15	14.56	10.87	12.25	13.69	8.86	2.85	-2.41	-9.14
PF4 (MA)	20.411	20.09	18.15	14.56	5.91	8.00	13.69	10.06	0.00	0.00	0.00
PF5 (MA)	14.529	14.303	13.61	10.92	5.24	7.89	12.87	12.90	13.60	10.79	6.250
PF6 (MA)	0.2507	0.2468	0.122	-0.16	-0.58	-1.96	-3.82	-5.80	-8.45	-7.14	-6.49
PF7 (MA)	0.2507	0.2468	0.122	-0.16	-0.58	-1.96	-0.99	-1.79	-2.72	-4.79	-5.25
R (m)	0	0	4.50	4.90	5.40	5.85	6.00	6.00	6.00	6.00	6.00
a (m)	0	0	0.8	1.20	1.7	2.14	2.15	2.15	2.15	2.15	2.15
b/a	0	0	1.00	1.00	1.00	1.41	2.22	2.22	2.22	2.22	2.22

References

[4.2.1] L. Bottura. "He-SS: A computer Program for Steady State Analysis of Helium cooled conductors", NET/IN/87-62, 22.12.1987

[4.2.2] J. Minervini, L. Bottura, "Stability Analysis of the NET TF and PF conductors", NET/IN/87-08, 23.3.1987

[4.2.3] N. Mitchell, L. Bottura, "Design Basis for the Toroidal Field Coils", N/P/3510/2/B, 28.11.1989

[4.2.4] N. Mitchell, L. Bottura, F. Fardi, "Concept Design and Analysis of the Toroidal Field Coils", N/P/3510/2/B, 28.11.1989

[4.2.5] D.S. Beard, W. Klose, S. Shimamoto and G. Vécsey (eds.) "The IEA Large Coil Task. Development of Superconducting Toroidal Field Magnets for Fusion Power", Fusion Engineering and Design, 7 (1 & 2), (1988), pp 1-232

[4.2.6] W. Stautner, "Rohrreibung des LCT-Leiters", private communication

[4.2.7] A. Hofmann, "A study on Nuclear Heat Load tolerable for NET/TF Coils cooled by Internal Flow of Helium II", KfK 4365, (1988)

[4.2.8] L. Bottura, "A Collection of Electrical and Thermal Properties for the NET Conductor Materials", NET/N/I/3000/1/A, 10.4.1989

[4.2.9] H. Brechna, "Superconducting Magnet Systems", Springer-Verlag, (1973), pp. 301-305

[4.2.10] V.D. Arp, "Stability and thermal quenches in forced-cooled superconducting cables", Proc. of 1980 Superconducting MHD Magnet Design Conference, MIT, (1980), 142

[4.2.11] F.P. Incorpera and D.P. DeWitt, "Fundamentals in Heat Transfer", John Wiley & Sons, (1981), pp. 204-206

[4.2.12] P.J. Giarratano and W.G. Steward, "Transient forced convection heat transfer to helium during a step in heat flux", Trans. of the ASME, Vol. 105, (1983), 350

[4.2.13] M. Klemm, E. Seibt, W. Specking, J.Q. Xu and R. Flükiger, "Enhancement of j_c at 10-12 T in Nb_3Sn Wires by Artificial Ta Inclusions distributed at a Nanometer Scale", Supercond. Sci. and Technol. 3 (1990) 249-254

[4.2.14] L. Bottura, private communication

[4.2.15] A. Nyilas, private communication

[4.2.16] K. Kwasnitza et al., "Basic equations for the calculation of AC losses in the conductor for the superconducting NET-TF coils", KRYO-86-13, October 1986

[4.2.17] L. Bottura and J. Minervini, "AC losses calculation in the NET TF coil", NET/IN/87-32, 28.7.1987

[4.2.18] R. Flükiger et al., "Status of the development of the KfK NET Toroidal Field conductor", Proc. of the 15th Symp. on Fus. Techn., Utrecht, September 19-23, 1988, pp. 1589-1595

[4.2.19] S.J. Sackett, "EFFI, a code for calculating the electromagnetic field, force and inductance in coil systems of arbitrary geometry", LLNL, Livermore, California, UCRL-52402 (1978)

[4.2.20] R. Flükiger et al., "An A15 Conductor Design and its Implications for the NET-II TF Coils", Final Study Report, KfK 3937, (1985)

4.3 Special considerations for the conductor design

4.3.1 Estimation of the transverse time constant

The eddy current losses in a complex conductor configuration can be estimated by some simplifications. The conductor consists of several components having different geometric arrangements and also so different electrical properties. Thus the conductor is in reality an electromagnetically and galvanically coupled system of inductive loops. It is well known that in a first approximation the losses can be estimated by the time constant of the eddy currents. Since the conductor has mainly a rectangular geometry the time constant of a slab geometry is a very appropriate approximation

$$\tau = \frac{\mu_o l_o^2}{\rho \cdot \pi^2}$$

l_0 is a characteristic length, in twisted superconductors half of the twist pitch l_p respectively the transposition length in a cable, and ρ is the resistivity. Thus in a complex conductor configuration the task is shifted to find a good approximation for the average resistivity along the flow path of the induced current.

The main contribution to eddy current losses in a superconductor is given by the change of magnetic field components vertically to the axis of the conductor. In this situation the induced electromagnetic voltages are in the conductor plane and drive the screening currents forth and back parallel to the conductor axis with components in the superconducting path and in the normal conducting matrix. A general simplified flow pattern of the screening currents through the normal conducting matrix is given in Fig. 4.3.1. On the basis of this pattern and the geometric size of the whole conductor arrangement the individual resistances were calculated. The resistivity values of the different components used here for the calculation are

$\rho_{Cu} = 4 \cdot 10^{-10}\ \Omega m$ (at 6 T)
$\rho_{bronze} = 3.2 \cdot 10^{-8}\ \Omega m$
$\rho_{solder} = 1.6 \cdot 10^{-8}\ \Omega m$
$\rho_{CuNi} = 1.4 \cdot 10^{-7}\ \Omega m$
$\rho_{sc} = \rho_{bronze} \cdot (1-\lambda)/(1+\lambda) = 1.96 \cdot 10^{-8}\ \Omega m\ (\lambda = 0.24)$

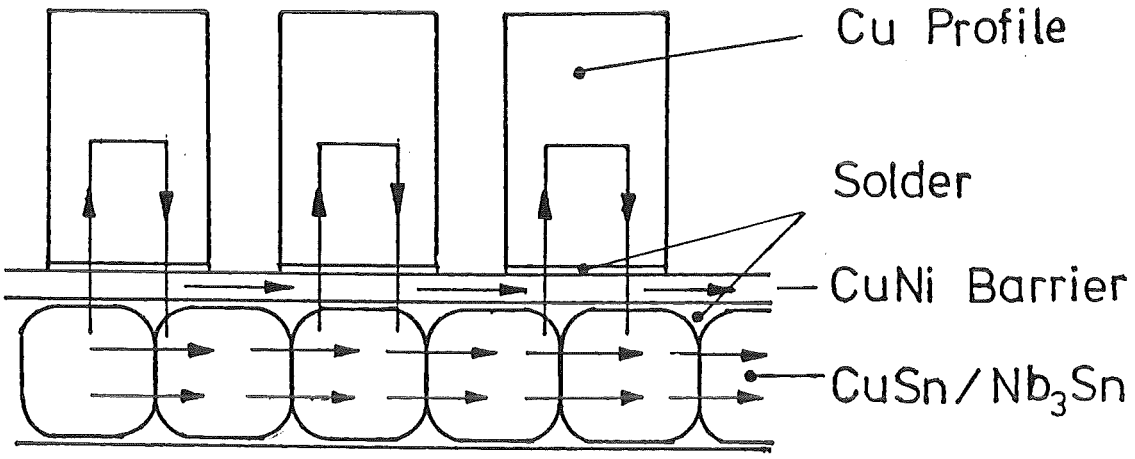

Fig. 4.3.1 The expected flow pattern of the screening currents in the NET II conductor

The total resistance for all the parallel currents was then evaluated and finally expressed in terms of resistivity for the overall conductor cross section excluding the steel case. This results in a resistivity value of

$$< \rho > = 4.33 \cdot 10^{-8}\ \Omega m$$

leading to a time constant of

$$\tau = 81\ ms$$

Within the accuracy of the estimation this time constant is compatible with the measured one in section 6.2.2 which was measured without the stabilizing copper.

4.3.2 Insulation in the core

In an earlier proposal of that flat cable conductor configuration it was assumed that a core insulation is necessary to separate electrically the upper and the lower part of the cabled strands. But it turned out that such kind of core insulation can be omitted. The formulas for eddy current losses in a Rutherford type cable used up to now are based on the consideration of only two strands twisted with the transposition length of the cable leading necessarily to a large induction loop and

consequently to large inductive currents crossing vertically the center plane. Considering the inductive coupling of neighbouring strands the result was that the screening currents are mainly flowing parallel to the center plane and transversal currents could be neglected. The loss formulas for the parallel and transversal losses are

$$P_{\|/l^*} = \frac{\dot{B}^2}{48} \quad \frac{d \cdot b}{\rho_{\|}} \cdot l_p^2 \left[\left(\frac{2b}{l_p}\right)^2 + 1\right] \qquad \left[\frac{Watt}{m}\right] \tag{4.3.1}$$

$$P_{\perp/l^*} = \frac{\dot{B}^2}{16} \quad \frac{d \cdot b}{\rho_{\perp}} \cdot l_p^2 \cdot \left(\frac{d}{b}\right)^2 \left[\left(\frac{db}{l_p}\right)^2 + 1\right]^2 \qquad \left[\frac{Watt}{m}\right] \tag{4.3.2}$$

($\dot{B}$ magnetic field change; $\rho_{\|}$ and $\rho_{\perp}$: resistivity in the different directions; d : strand diameter; b: width of the cable; l_p : the transposition length; ℓ^* : the length of the conductor)

It can be seen that the transversal losses compared to the parallel losses are mainly reduced by the square of the ratio of the filament diameter d to the cable width b, a value of two orders of magnitude smaller than one.

4.3.3 The resistive barrier between Nb_3Sn core and stabilizer

A resistive barrier between the superconductor and the normal conducting stabilizer will not impair the electrical stability of the superconductor as long as the "cold end recovery" criterium is fulfilled. In case of a normal conducting zone in the superconductor the electrical current will be bypassed via the barrier and the stabilizer, however, this needs a certain current transfer length l_0. This transfer length l_0 means a apparent lengthening of the normal conducting zone by two times l_0.

The transfer length depends on the resistivity of the stabilizer $\rho_{\|}$ and that of the barrier $\rho_{\perp}$ and obeys the following formula

$$l_o = \sqrt{\frac{\rho_{\perp}}{\rho_{\|}}} \sqrt{a \cdot d} \tag{4.3.3}$$

(a: thickness of the stabilizer; d: thickness of the barrier including a certain amount of the bronze matrix which has to be passed also vertically by the current)

The power generated in the transition zone amounts to

$$P = \rho_{\parallel} \cdot j_o^2 \cdot a \cdot b \cdot l_o \qquad (4.3.4)$$

with the current density j_o in the stabilizer cross section $a \cdot b$. Half of that power is generated in the stabilizer and the other half is generated in the resistive barrier. This heating power has to be removed by cooling to recover the superconducting state. The heat flow rate is the same as along the normal conducting zone.

In the NET-II conductor the transfer length amounts to

$$l_o = 1.5\,\text{cm}$$

$\rho_{\parallel} = 4 \cdot 10^{-10}\,\Omega\text{m}$, $\rho_{\perp} = 1.7 \cdot 10^{-7}\,\Omega\text{m}$, $a = 2.6\,\text{mm}$, $d = 0.2\,\text{mm}$.

The power generation in a stabilizing Cu profile with $j_o = 12.0 \cdot 10^3\,\text{A/cm}^2$ is

$P = 0.33$ Watt, that means a heat flow rate through the cooled surface ($S = 2\,l_o \cdot a$) of

$$\dot{q} = 1/2\,\rho_{\parallel}\,b\,j_o^2 = 0.43\ \text{Watt/cm}^2.$$

This value for the NET conductor would be in the limit of the classical stability criteria under bath cooling conditions. This heat load at the surface can be removed by the heat transfer, according to chapter 4.2.4.

5. INDUSTRIAL FABRICATION OF A SUBSIZE CONDUCTOR

Major manufacturing steps of the KfK-NET-TF superconductor are:

- Cabling process of the Cu/Sn/Nb strands to a flat cable.
- Reaction heat treatment for the Nb_3Sn formation.
- Soldering of the reacted cable into two CuNi U-type sections to produce a rigid monolithic core.
- Manufacturing of electrical stabilizing units by the Roebel technique.
- Soldering of the core between two stabilizing units to form a sandwich type cable.
- Jacketing of the cable within stainless steel sections using the laser beam welding technique.

To optimize the cost/benefit ratio it was decided to start first with a subsize superconductor fabrication step (scale 1:1.75), which should include all major manufacturing procedures necessary for a later full size cable fabrication.

The basic superconducting strand used for the subsize cable was a Nb_3Sn composite wire, fabricated by VAC by the bronze route technique. Table 5.1 contains the main technical characteristics of the subsize conductor components.

5.1 Cabling process

The 31 strands are cabled with a standard planetary cabling machine with 100% backtwist. The transposition is in the same sense as the twist pitch and is ~ 140 mm (in the full size cable this value will be ~ 300 mm). Although the current status of the cable production is a cable without an insulation core strip, the first produced subsize cable incorporates a hard bronze sheet in the middle of the flat cable. The total length of the cable was divided into two halves. One length was produced with the hard bronze sheet, the other length with a bronze sheet, the surface being alumina deposited to ensure electrical insulation. The total produced length of this cable was ~ 30 m. To check the effect of the absence of an insulation (prevent design) ~ 100 m of cable without a core strip were also produced in the same line. After cabling, all cables were calibrated on the same line to a rectangular flat shape. The produced 30 m cable (cabled and calibrated with the bronze core (non insulated) was reeled on with a pulling force of ~ 700 N

Table 5.1: Main technical characteristics of the KfK-NET-TF subsize conductor samples

Sample name		STRAND	CORE + STAB	CORE + STAB + JACKET
Parameter	**Unit**	**Strand (basic wire)**	**Core + Stabilizer**	**Core + Stabilizer + Steel Jacket**
Manufacturing process		bronze route	soldered to each other	drawn onto the core
Heat treatment		64 h at 700 °C in Argon atmosphere	64 h at 700 °C in Argon atmosphere	64 h at 700 °C in Argon atmosphere
Strand (Wire)				
Diameter	mm	0.8		
Number of filaments		6 000		
Diameter of filament	µm	4		
Twist pitch	mm	25		
Internal copper stabilization	vol %	17		
Ta barrier	vol %	6		
Core				
Number of strands in the core			31	
Transposition pitch	mm		120	
Manufacturing process			cabled, soldered into two U shaped CuNi sheets	
Thickness of CuNi sheets	mm		0.25	
Cross section	mm^2		14.3 x 3.0	
Stabilizer				
Manufacturing process			Roebel	
Number of stabilizer cables			2	
Number of Cu strands per stabilizer cable			11	
Cross section of single Cu strand	mm^2		1,5	
Dimension of steel strip	mm^2		2 x 0.2 x 12.0	
Steel jacket				
Outer dimensions	mm^2			11.4 x 17.6
Thickness	mm^2			1.5

on a drum to avoid the cable collapse after the cabling process. This is the only way to produce a flat cable with hard bronze Nb/Cu/Sn strands with a hard bronze core. The dimension of this cable after the calibration was 12.45 x 1.95 mm^2.

The 100 meter cable without the core strip was produced in two lengths. One length was ~ 30 m and the other one ~ 70 m long. The reel on and reel off after the cabling process bear in this case no risk and this is the purpose of reaction heat treatment investigation to gain information about the cable behaviour after the Nb_3Sn-formation.

The dimension of the cable was 12.45x1.40 mm^2, which has a reduced thickness compared to the latter one. This reduced thickness is a benefit for the heat treatment process, i.e. smaller drums, smaller furnaces and thus reduced costs.

5.2 Heat treatment

The Nb_3Sn formation was performed by reaction heat treatment process at 700°C/64 h (flat top). Elaborate investigations were necessary to procure this step without a risk. The only way to produce flat Nb_3Sn cables is to lead the non-avoidable distortion in a controlled orientation. By giving spatial freedom in one direction (length) and blocking the two other directions (axial and radial) the cable movement during the heat treatment process could be linked in the length orientation. Representative lengths of Nb_3Sn cables could be produced by using stainless steel (304L type) drums. The surface of these drums were nitride hardened to avoid a sintering of the first layer of the bronze cable. The diameter of the drums were 600 m ø as shown in Fig. 5.1. Several drums could be inserted in a small vessel of ~ 1000 mm and 500 mm height (see Fig. 5.2).The vessel was vacuum tight welded to ensure the later clean operation (see Fig. 5.3). The vessel was operated under purified argon flow condition. Three thermocouples have been used to record the temperature in various spatial positions during the heat treatment process.

The cable with the hard bronze core strip, which was reeled on the drum very tight with a pulling force of ~ 700 N showed after the reaction heat treatment in its total length a very constant dimensional uniform behaviour. The reacted pancake itself was rigid and a gap of ~ 5 mm was opened between the first layer and the drum. This confirms the unidirectional material flow of the cable during the Nb_3Sn-formation. Between the cable layers a 0.35 mm thick graphite strip was positioned to avoid the cable to cable sintering. Figure 5.4 shows the pancake before the reel off. During the reel off the cable dimension was measured. A

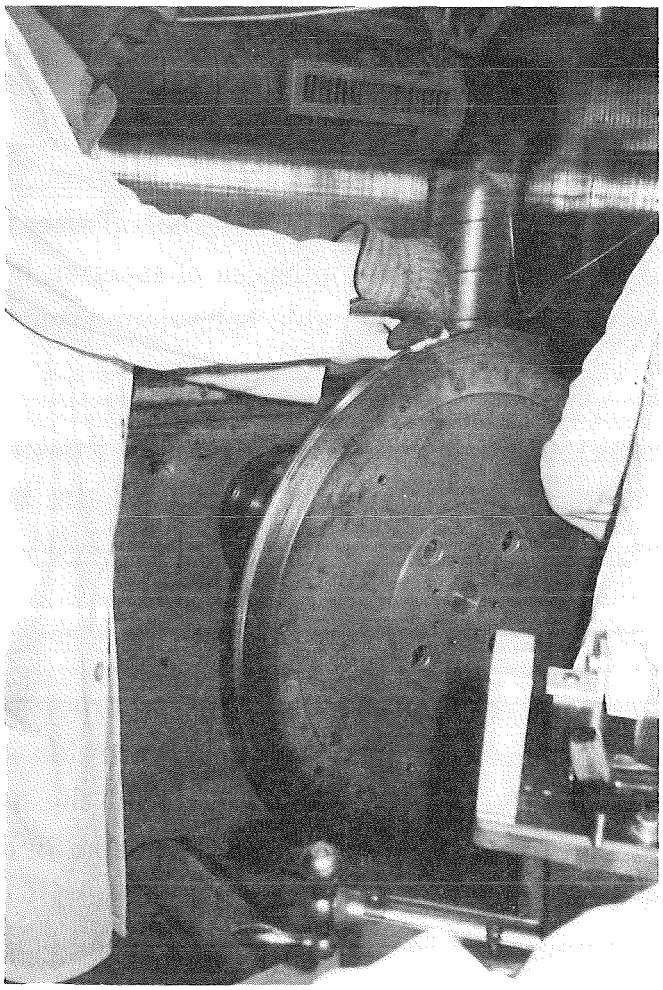

Fig. 5.1: Reaction heat treatment drum during reel on of the Nb/Cu/Sn cable.

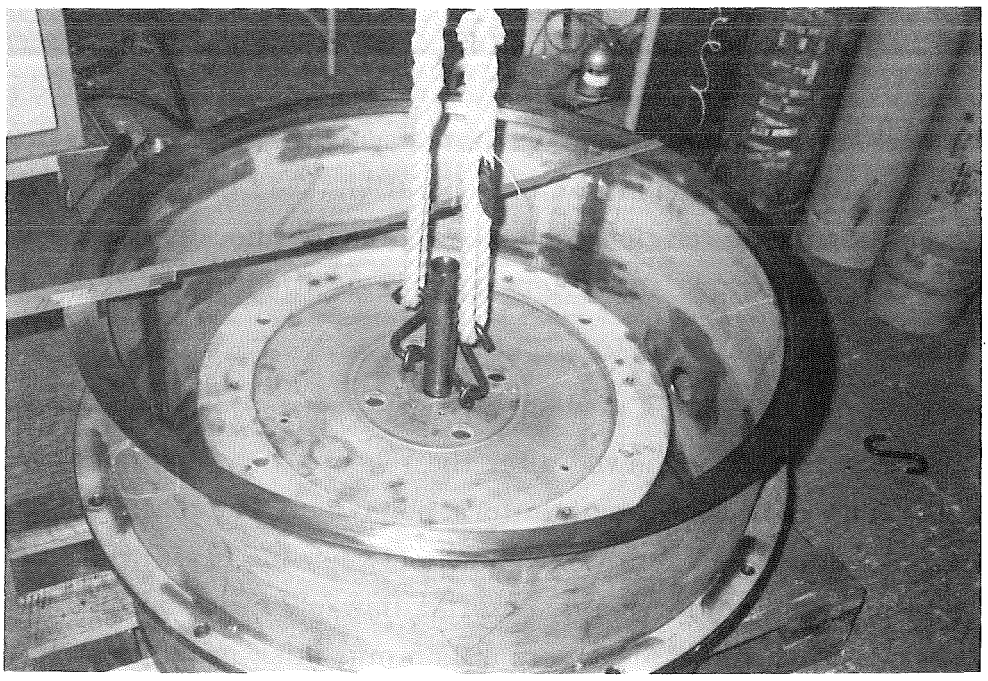

Fig. 5.2: Inserting of the drum in the heat treatment vessel

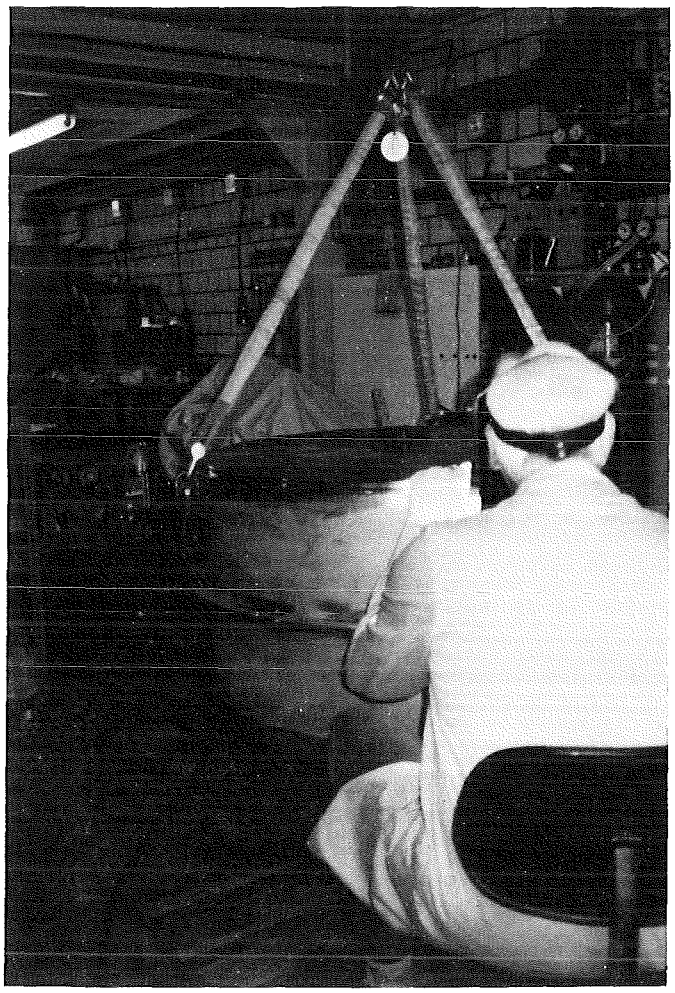

Fig. 5.3:
Vacuum tight welding of the vessel

variation of $\pm$ 20 µm in width (12,45-12,49) mm and $\pm$ 5 µm in thickness (1,995-2,015) mm was determined. This cable was the basis of the first subsize production length.

The heat treatment process was conducted in a way where the drum axis position was in vertical and the vessel was tilted 90°. To find out the possible effect of the horizontal position, where the pancake rests flat on the bottom of the vessel a second heat treatment test was carried out with a cable of ~ 70m length. The cable this time was without a core strip. Dimensions of the cable were 12,65x1,45 mm^2. The reel on was performed with a minimum of a pulling force. All other handling processes remained comparable to the latter one. The reaction heat treatment gave almost the same result with a very low dimensional ariation in width and thickness position.

From these results on reaction heat treatment one can state that the Nb_3Sn-formation process of cables, cabled with bronze route processed Cu/Sn/Nb strands, is feasible without any risk. The remaining strain during the bending of the cable

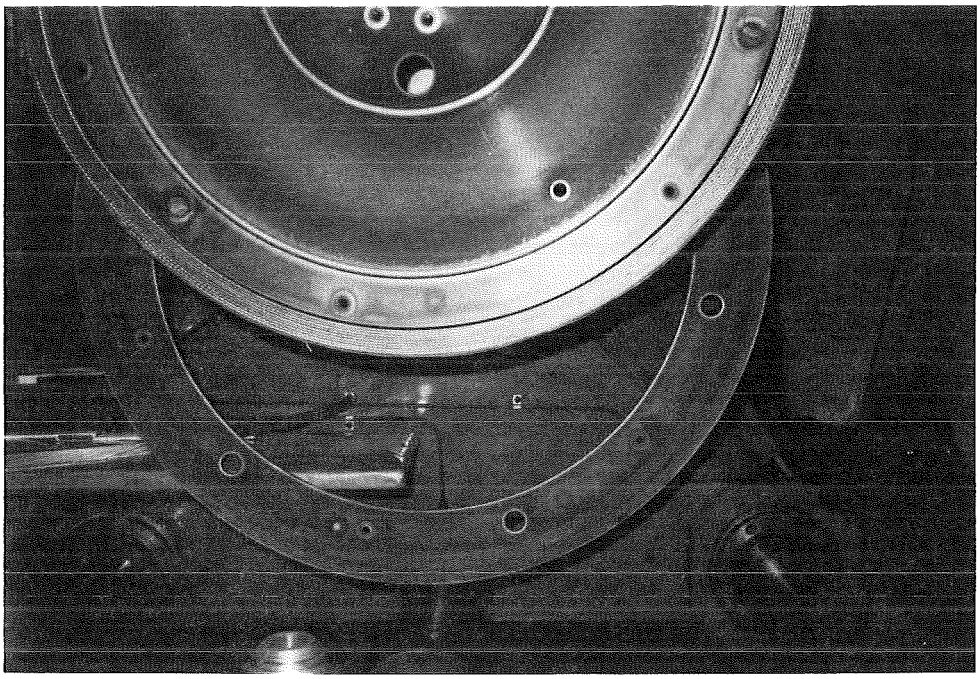

Fig. 5.4: The longitudinal size increase of the cable after the Nb_3Sn-formation. Note the gap between drum and the pancake.

(with bronze core strip) to a flat position is ~ 0.33% and ~ 0.24 for the cable without the core strip, respectively.

5.3 Core manufacturing

For the fabrication of the composite core according to the given design a soldering machine was developed. This line allows to solder the reacted cable continuously into two U-type CuNi sections. The CuNi sections were premanufactured in a standard way by using a rolling system, which produced accurate lengths out of flat CuNi (0,2 mm thick) sheets. The solder material was the alloy Sn 58Pb39In3. The working temperature of the solderbath was controlled to be between 260-270°C. The soldering was performed in a ceramic vertical tight dimensional mould system. The production allowed a speed of ~ 0.3 m/min. In this machine ~ 13 m of cable was soldered continuously without any major problem. The soldered cable was from the first batch (reacted cable with a hard bronze core strip). The pulling force was ~ 150-300 N during the processing. Figures 5.5, 5.6 and 5.7 show the core during the fabrication. The dimension of the core after the production was 14.37-14.40 in width and 2.93-2,46 mm thick, respectively. A peel off test confirmed the good weldability of the solder with the CuNi sections. The soldering machine is designed to be capable of manufacturing the full size core of the NET-TF cable.

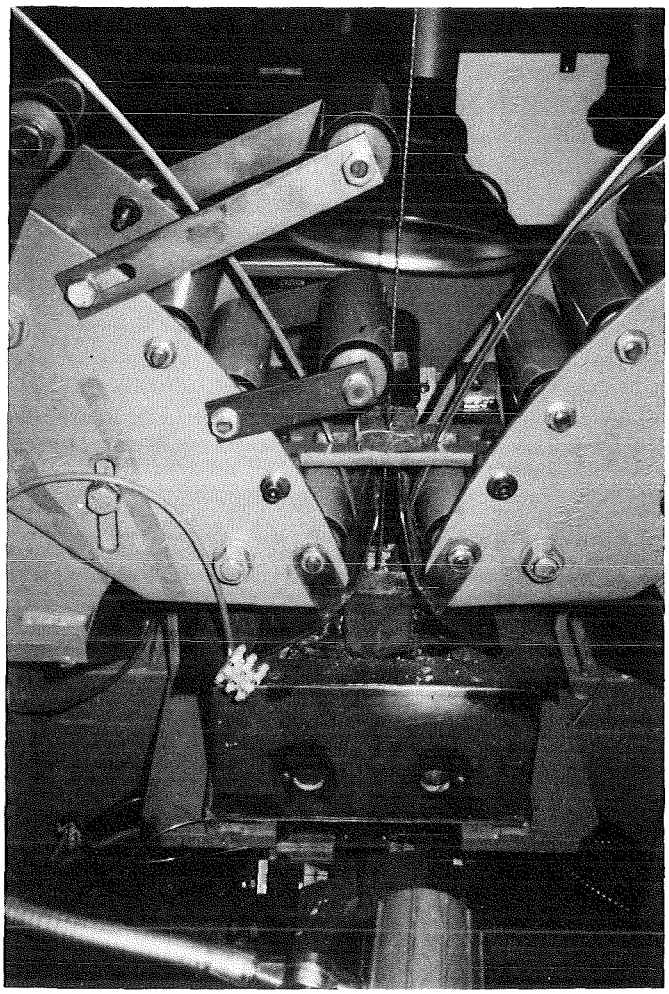

Fig. 5.5:
Entering of the cable in the soldering machine. The end of the cable with the two CuNi sections can be seen.

5.4 Manufacturing of the electrical stabilizer

The electrical stabilizer was fabricated in a small cabling machine on a 2 stage composite core with an insulation in the mid section (stainless steel/adhesive/Kapton/adhesive/stainless steel). After cabling and the calibration process every second copper wire was removed to ensure the gaps of the cooling channels. The cable was then soldered in a bath. The copper section had a dimension of ~ 1.5-1,8 mm. The stabilizer for the full size cable will be Roebel processed. Because of the high costs for a small quantity it seemed to be reasonable to avoid the Roebel processing in the case of the subsize cable production. In addition, the Roebel process is already well demonstrated during the LCT-cable production. Same solder material (Sn58Pb39In3) was used for the soldering of the copper section in case of the stabilizer.

Short lengths of ~ 1200 mm suitable for the 4 K electrical measurements (I_c vs. ε) were produced with a low melting solder material. The working temperature was ~ 180° C, which is lower than the melting point of the core solder material. A 4 m long cable and a 2 m longcable were separately produced in one piece for the

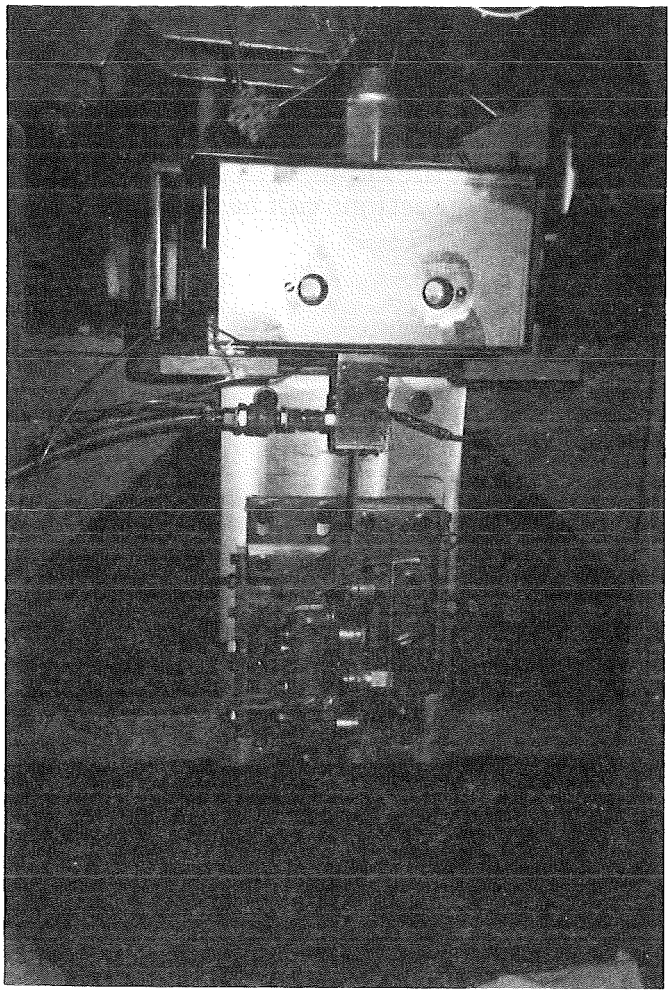

Fig. 5.6:
Beneath of the solder bath. The core is guided to the pulling caterpillar by a vertical guiding system.

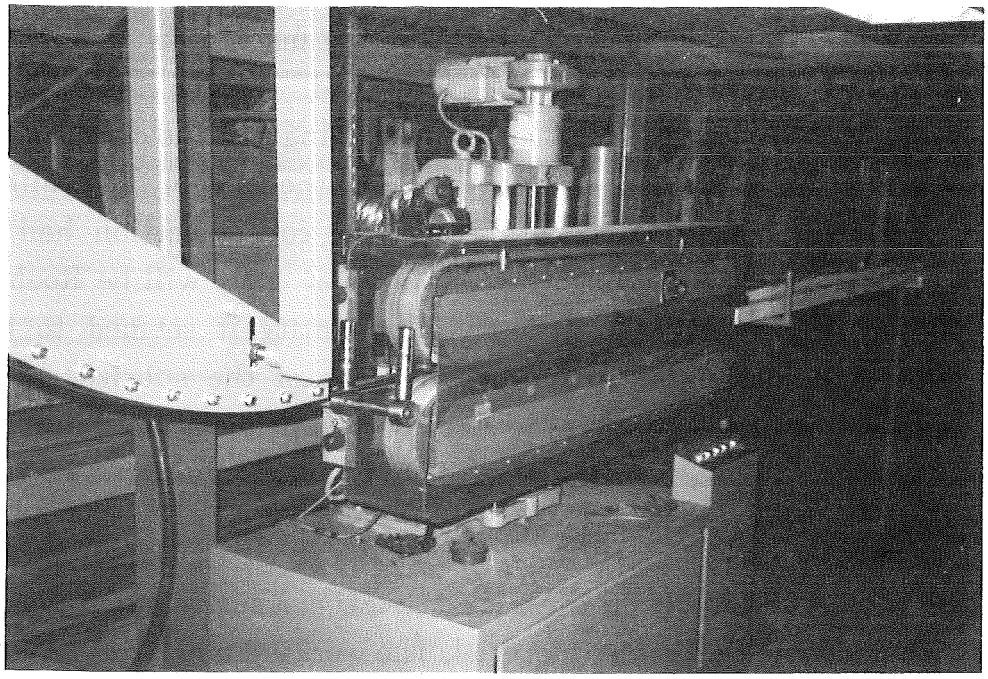

Fig. 5.7: Pulling of the core with the caterpillar.

for the purpose of the jacketing. The measured dimensional variations were 14.443 mm $\pm$ 0.076 in width and 8.268 $\pm$ 0,117 mm in thickness.

5.5 The jacketing by laser beam welding technique

The jacket of the cable requires 4 weld seams. The small size of the subsize cable will, however, add little knowledge towards the jacketing by laser beam weld process. In addition, during the poloidal field coil cable development reasonable amount of experiences were gained with this new technology. We can therefore state that the KfK-NET-TF cable can be ready weldable concerning the somewhat thicker jacket material.

The points to be considered are:

- Two laser working stations of the same type and same power range.
- A power of 3 kW seems to be reasonable for the ~ 4 mm thick jacket material.
- Use of the mirror system instead of lenses.
- In all spatial positions adjustable laser beam guns.
- Quality control of beam mode.
- Clean surface of the joints to be welded.
- A stop and go process control experience should be gained by preliminary weld tests.
- A stiff linear guiding system.
- Quality control of the weld seam.

All these technological experiences were gained by KfK during the production of the four lengths of the Polo-cable. Decreasing the jacket size as in the case of the subsize cable, will increase the required tolerances concerning the beam position, mode control, etc.. The KfK-NET-TF full size jacket production will, however, destress the situation compared to the poloidal field coil cable.

Therefore it was decided to produce the jacket of the subsize cable by an alternative method. The two lengths of 4 m and 2 m are industrially produced by jacketing a seamless tube. The tube was calibrated accurately on the subsize cable by drawing. The feasibility is demonstrated by the Dour Metal Company in Belgium. Figure 5.8 shows a cross section of the produced superconductor.

6. MEASUREMENTS

6.1 The effect of static and cyclic axial stresses on I_c of subsize NET Nb_3Sn conductor

6.1.1 Samples

For studying the physical properties of the KfK-NET-TF conductor, produced by the react and wind technique, the reduced size KfK-NET-TF conductor at the scale of 1:1.75 has been tested (Fig. 6.1.1).

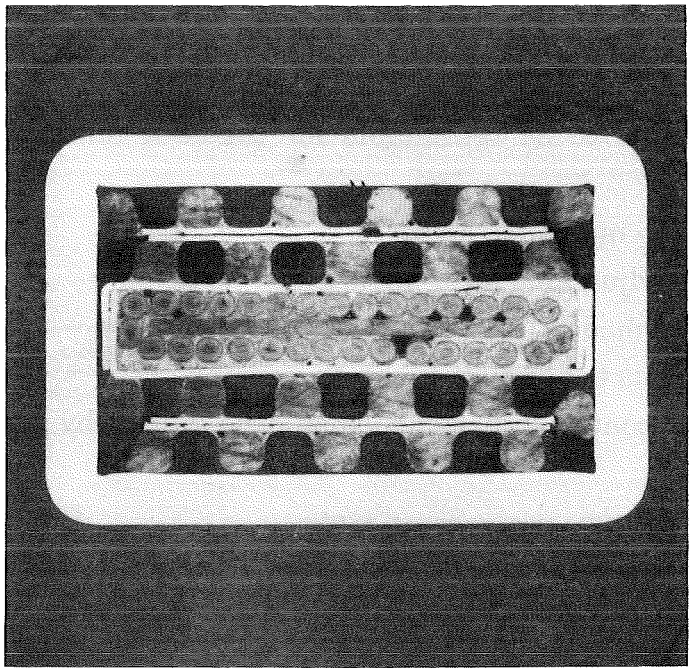

Fig. 6.1.1: Subsize superconductor cross section with the calibrated jacket on the cable.

In this section the measurements of the basic Nb_3Sn strand wire (sample STRAND), the superconducting core including the electrical stabilizer (sample A) and finally the complete subsize conductor (sample B) are presented. All samples have been heat treated for 64 h at 700°C in Argon atmosphere. Table 5.1 contains the main technical characteristics of the samples.

6.1.2 Apparatus and measurements

All measurements were performed in the FBI superconductor test facility at KfK which allows the testing of short straight samples at T = 4.2 K by simultaneously loading with axial force, F, magnetic field, B, and electrical current, I. Depending on the sample load different test rigs were used. For example, the subsize conductor (samples A, B) were tested in a 100 kN - 10 kA test rig allowing static and cyclic axial force up to 100 kN and currents up to 10 kA (Fig. 6.1.2). The magnetic field was supplied by a split coil perpendicular to the sample, which reaches B = 13 T at the gap width of 15 mm (field homogeneity ± 1,5 % within ± 25 mm along the sample axis). The self field of the sample was not considered at the analysis while an I_c criterion of 1 µV/cm was used for all samples. Further details about the FBI facility are given in [6.1.1]. After cooling to 4.2 K first the critical current, I_c, as a function of the magnetic field, B, without applied axial strain, ε_a, was measured, then I_c (and the axial force, F) versus ε_a under static loaded and unloaded conditions at a constant field of B = 12 T. Additionally the subcables with and without steel jacket were cyclically strained at different strain levels.

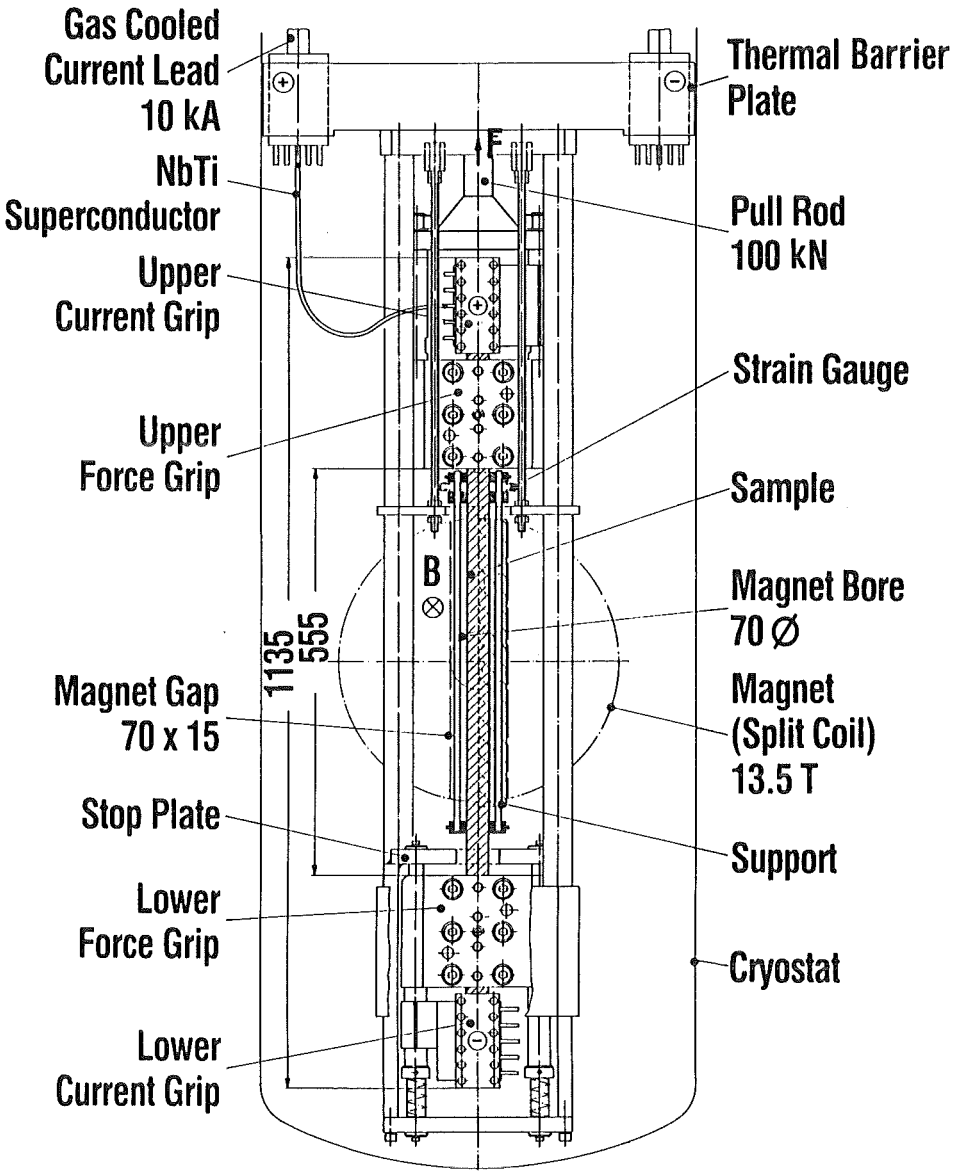

Fig. 6.1.2: The FBI 100 kN/ 10 kA/13 T test rig at KfK
(All dimensions in mm)

6.1.3 Results and discussions

6.1.3.1 I_c vs B measurements

The I_c vs B curves at $\varepsilon_a = 0$ and T = 4.2 K are shown in Fig. 6.1.3 The curve STRAND x 31 represents the I_c values of the single strand samples multiplied by 31 for comparison with the cable samples. One important result is the complete conformity of the I_c values of this sample with the sample B, the final cable with

the steel jacket. This means the whole fabrication procedure including the most delicate step of the steel drawing onto the already reacted cable has not affected the $I_c(B)$ characteristic. However, the sample A degradates compared to the STRAND (about 17 % at 12 T) which will be discussed in the next chapter.

6.1.3.2 I_c vs ε_a measurements

Fig. 6.1.4 shows the normalized critical current, I_c/I_{cm}, where I_{cm} represents the maximum of I_c, as a function of the axial intrinsic strain, $\varepsilon_o = \varepsilon_a - \varepsilon_m$, where ε_m is the strain at I_{cm}. All sample exhibit about the same characteristics. (Sample B could be strained only to $\varepsilon_o = 0.03$ % due to a failure of the apparatus). The compressive intrinsic strain amounts to $\varepsilon_o \approx -0{,}3$ % ($\varepsilon_m \approx 0{,}3$ %) for all samples and the I_c degradation, I_c/I_{cm}, at this ε_o value reaches about 0.84 for the samples STRAND and B and 0.72 for sample A. This means the decrease of I_c without applied strain at 12 T is 15 % higher for the sample A than for the samples STRAND and B. This is comparable with the results of the I_c vs B measurements (Fig. 6.1.3), where a difference of 17 % at 12 T between these samples has been observed. The additional decrease of I_c/I_{cm} for the sample A compared with the sample STRAND can be explained with the higher prestress in the sample A due to the bronze foil in the Nb_3Sn cable, the CuNi jacket around the cable and the stabilizer, which contains copper and the more effective stainless steel. For the sample B one would expect an even higher prestress due to the additional steel jacket relative to the sample A. But neither the measurements I_c vs B (Fig.6.1.3) nor I_c vs ε_a (Fig. 6.1.4) confirm this expectation: both characteristics of the samples STRAND and B are almost identical. This effect is not completely understood. One reason could be that during the drawing process of the steel jacket onto the reacted cable the prestress in the sample A is partly compensated leading to higher I_c values of the sample B in comparison to the sample A.

6.1.3.3 Cycling behavior

One of the most important tests for fusion conductors is the behavior of I_c after several strain cycles. Therefore both the samples A and B were cycled at 12 T and 4.2 K at different strain levels, shown in Fig. 6.1.5.

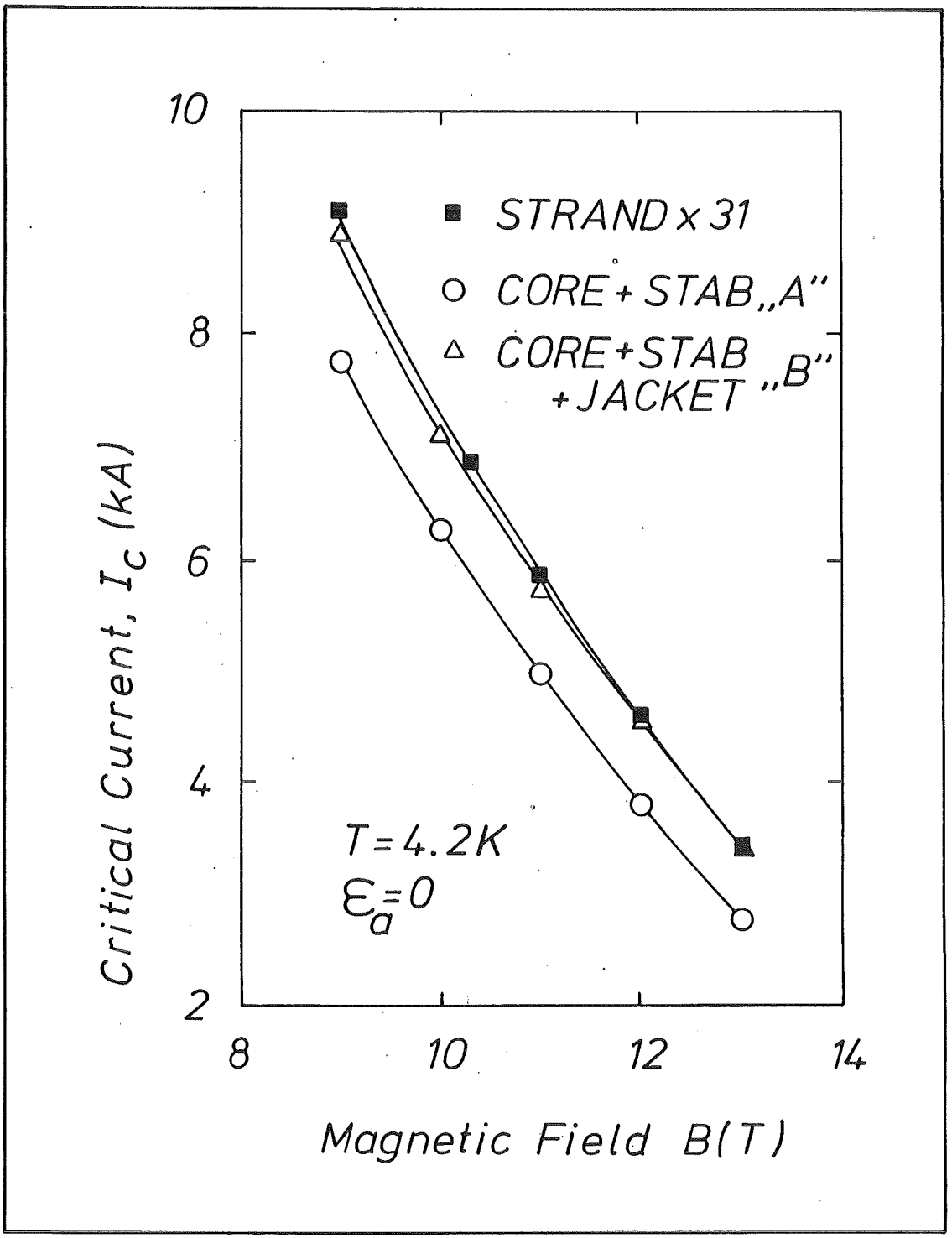

Fig. 6.1.3: Critical current, I_c, versus magnetic field, B, with out applied axial strain at 4.2 K.

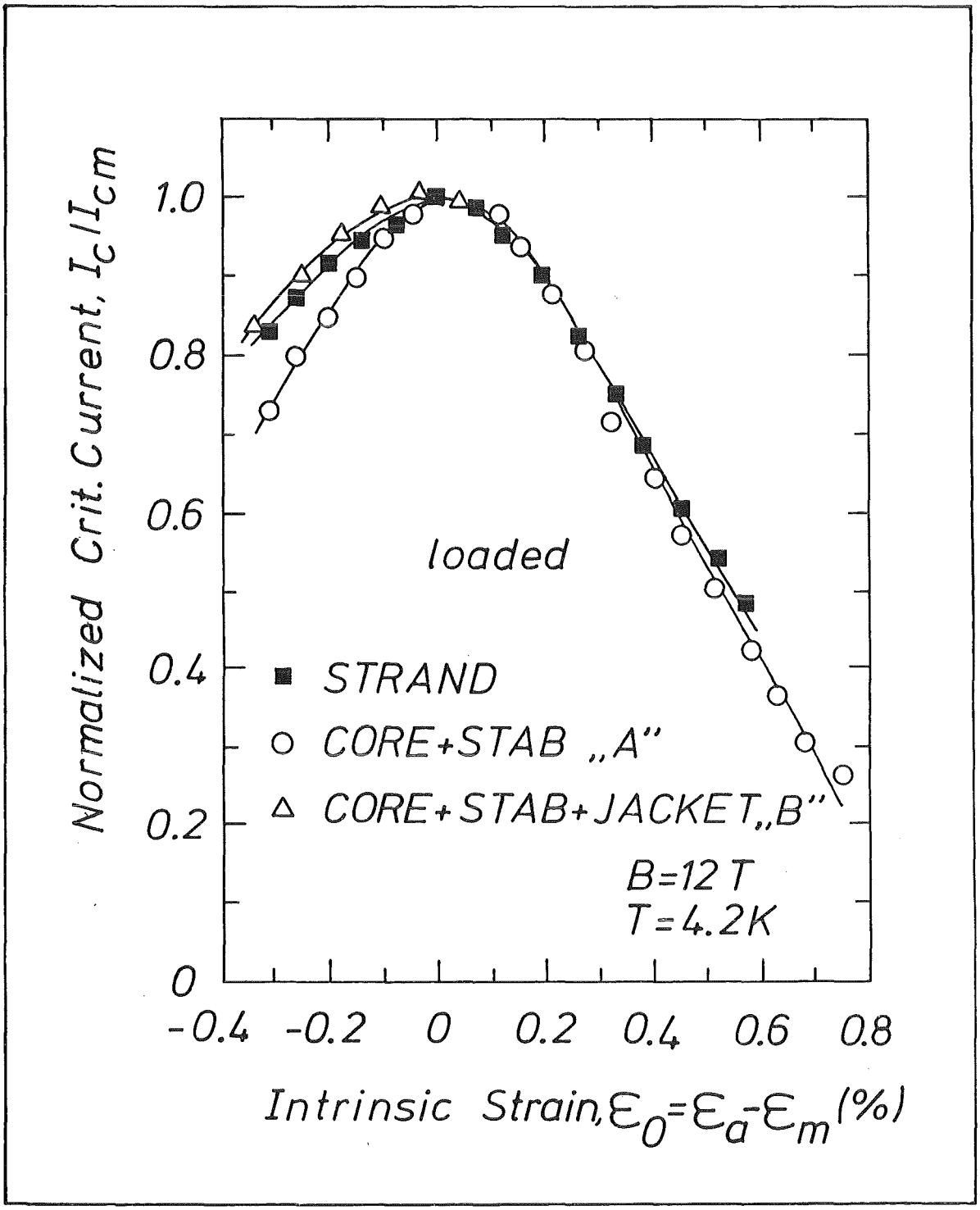

Fig. 6.1.4: Normalized critical current, I_c/I_{cm}, as a function of the intrinsic axial strain, ε_o, at 12 T and 4.2 K.

Sample A (CORE + STAB):

This conductor was first statically strained from $\varepsilon_a = 0$ to 0.18 %, resulting in an increase of I_c/I_{cm} from 0.72 to 0.91. At this point the sample was cycled 73 times up to 0.46 % with a cycling rate of about 0.01 Hz without any degradation of I_c. Then the strain was enhanced to $\varepsilon_a = \varepsilon_m = 0.32$ % and $I_c/I_{cm} = 1$ and cycled 25 times between 0.32 and 0.70 % with the same cycling rate. After further straining to 0.50 % and a lower value of $I_c/I_{cm} = 0.91$ the sample was finally cycled 25 times between 0.50 and 0.94 %. In all cases a complete reversibility of I_c was observed, irreversible behavior being expected at $\varepsilon_{irr} \geq 0.94$ % under the mentioned cycling parameters. Also shown in Fig. 6.1.5 is the reversibility of I_c under static loading and unloading conditions. After straining to $\varepsilon_a = 0.37$ % (point 1) the sample was unloaded to 0.09 % (point 1', the residual strain value of the sample), then to point 2-2', up to $\varepsilon_a = 1.06$ % (point 5), leading to a plastic strain of 0.59 % (point 5') in the unloaded condition.Thus, I_c for the samples A behaves reversible up to the measured static strain of $\varepsilon_a = 1.06$ % leading to an irreversible strain of $\varepsilon_{irr} \geq 1.06$ % under static conditions. Below this strain value no physical damage by filament cracking is expected.

Sample B (CORE + STAB + JACKET):

I_c was measured under static load up to $\varepsilon_a = 0.35$ % (point a, Fig. 6.1.5) and without load at the residual strain of 0.06 % (point a'). Then the sample was 100 times cyclically strained between 0.07 and 0.35 % and I_c was tested again under both static loaded ($\varepsilon_a = 0.35$ %) and unloaded conditions ($\varepsilon_a = 0.07$ %). In all cases no degradation of I_c was observed. At further straining the sample was unfortunately broken due to an operation error. But the I_c vs ε_a characteristic at $\varepsilon_a > \varepsilon_m$ of this sample should be similar to that of the sample A, moreover this strain region being less important for the practical application of such conductors.

Further test with considerably enhanced number of cycles of the final KfK-NET-TF subsize conductor are under preparation. However, we assume there is no influence on I_c as long as the cycling strain occurs below the irreversible strain which confirms earlier results on Nb_3Sn wires [6.1.2].

The effect of transverse compression on I_c of multifilamentary Nb_3Sn wires has previously been investigated [6.1.3 - 6.1.5]. A compression test rig is in preparation in order to extend these studies to cables like the NET subscale conductor.

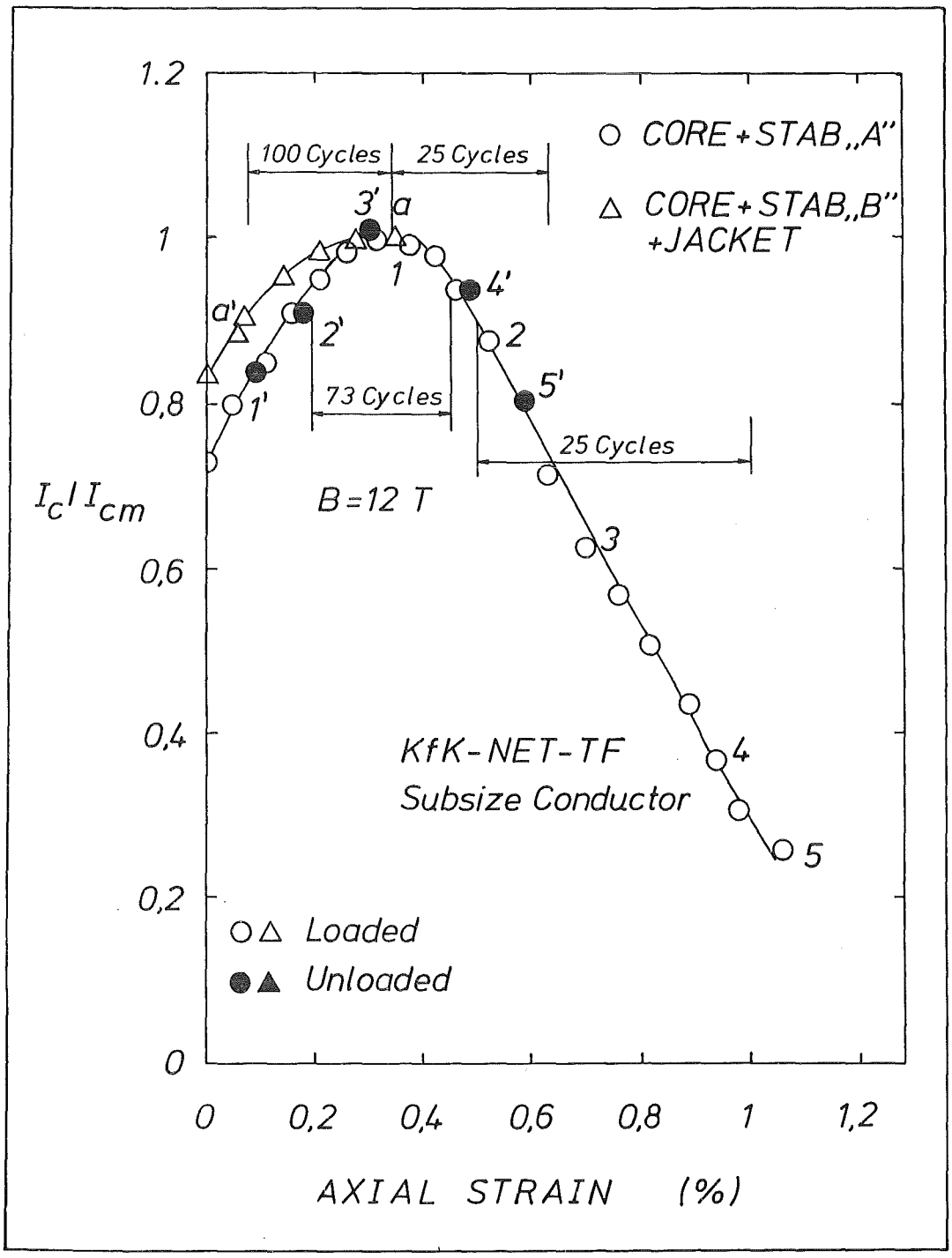

Fig. 6.1.5: Normalized critical current, Ic/Icm, versus applied axial strain, εa, at 12 T and 4.2 K. Sample CORE + STAB was cycled 73, 25 and 25 times at three different strain values, and sample CORE + STAB + JACKET 100 times between 0.07 and 0.35 % strain.

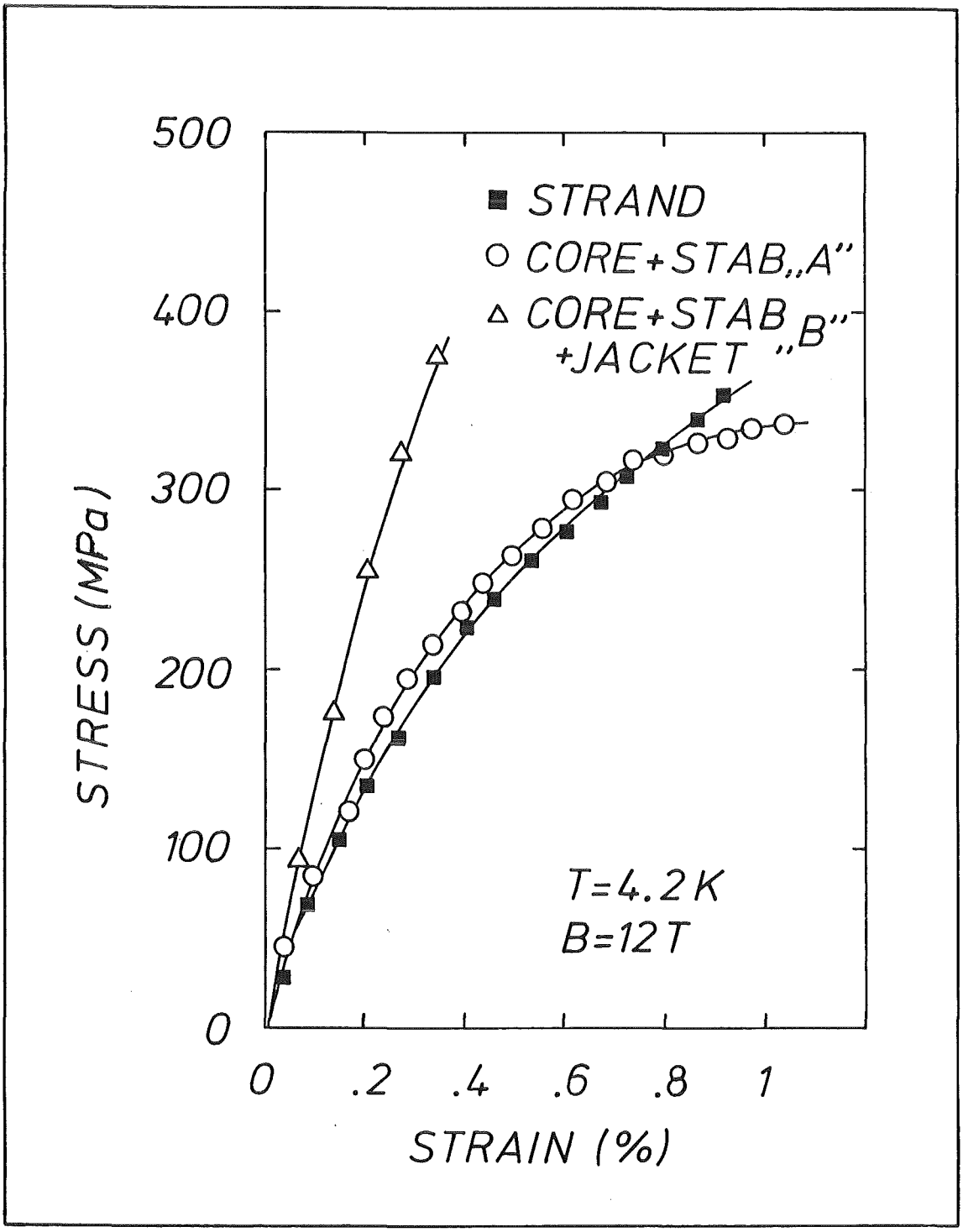

Fig. 6.1.6: Stress-strain curves at 4.2 K and 12 T.

6.1.3.4 Stress-strain curves

Simultaneously with the applied axial strain, ε_a, the tensile stress, σ_a, at 4.2 K and 12 T has been measured (Fig. 6.1.6). The elastic modulus, E, amounts to about 80 GPa for both samples STRAND and A and about 130 GPa for sample B. For determining σ_a of samples A and B the reference cross section includes the cooling channels (27 %).

The yield strength, σ_y, reaches about 270 MPa for both samples STRAND and A and ~ 500 MPa for the sample B. The increase of E and σ_y of the sample B compared to sample A, shows clearly the effect of the steel jacket, being 39 % of the total cross section of sample B. Note that this effect was achieved without introducing additional prestress.

References

[6.1.1] Specking, W., Nyilas, A., Klemm, M., Kling, A. and Flükiger, R., Proceedings MT-11, Tsukuba, Japan, 1989.

[6.1.2] T.Kuroda, H. Wada and K. Tachikawa, Adv. Cryog. Eng., Vol. 34, 577 (1988).

[6.1.3] B. Jakob and G. Pasztor, IEEE Trans.Magn., MAG-25, 2379 (1989).

[6.1.4] H. Boschmann, P.P.E. Fornerod and L.J.M. van de Klundert, IEEE Trans. Magn., Vol. 25, No. 2, 1976 (1989).

[6.1.5] W. Specking, F. Weiss and R. Flükiger, Proceedings, 12th Symposium on Fusion Engineering (1987), IEEE Catalog No. 87 CH 2507-2, p. 365

6.2 Time constant measurements of NET subsize conductors and stability behaviour during a plasma disruption

6.2.1 Short sample measurements

The technique of the time constant measurement is described in [6.2.1]. The cable sample of 12.5 cm length (one cabling length) is exposed to a half sinusoidal field pulse of a few milliseconds duration, perpendicular to the broad side of the conductor. The decaying eddy currents after the end of the field pulse are detected with a pick-up coil. A small background field of ~0.5 T parallel to the cable axis was supplied in order to avoid the tin-lead solder to be superconducting.

The following samples were investigated:

Sample 1:	CuNi core, 31 strands soldered onto the core
Sample 2:	insulated core
Sample 3:	Rutherford cable without core, soldered.

Fig. 6.2.1 shows a typical result for sample 1 The logarithm of the pick-up coil voltage after the end of the field pulse gives, in principle, the time constant. The result can, however, not be described by a single time constant, as it is usually the case for multifilamentary superconducting strands [6.2.2]. Furthermore the decaying eddy currents depend on the length of the inducing field pulse, as can be seen in Fig. 6.2.1. The reason is probably that different paths for eddy currents exist in a superconducting cable, each having a different decay time constant. The amplitude of the induced eddy currents in each path depend on the frequency of the inducing field (pulse time length). Short field pulses induce mainly eddy currents with a short time constant, long field pulses give higher amplitudes for the current paths with long time constants. There is, at present, no quantitative theory describing the decay of eddy currents in conductors of complex geometry.

The following table gives the time constant extracted from the ℓn U curves, for different pulse time lengths. The given values of τ are extracted from the slope of the ℓn U curves just after the end of the exiting field pulse.

	pulse length (ms)	1.9	5	16
Sample 1	time constants	0.6	0.8	2
Sample 2	in (ms)	1.1	1.8	2.6
Sample 3			1.2	2.4

For a very rough estimation of ac losses let us take the values measured with the 16 ms exciting pulse. We have here a time constant of $\tau_0 \sim 2.5$ ms. The first remark is that there is no significant difference between insulated and noninsulated core.

We may use the general loss formula

$$Q/V = (2/\mu_0)\, \dot{B}_i^2 \cdot \tau_0, \qquad Q/V = \text{loss power/ conductor volume} \qquad (1)$$

where

$$B_i = B_e - \dot{B}_i\, \tau_0, \qquad (2)$$

is the field inside the conductor and B_e is the external field. The dissipated energy is given by the integral

$$E/V = \int Q/V \quad dt \qquad (3)$$

The NET II-ITER-specifications for a plasma disruption suggest the following field variation of the perpendicular field component (the parallel field component is neglected here):

- Linear increase during a time $t_0 = 20$ ms with 20 T/s ($\Delta B = + 0.4$ T); followed by an
- Exponentiell field decrease with a time constant τ, and $\Delta B = -0.4$ T. The value of τ is not given in the NET specifications, but from estimations of the decay time constant of eddy currents in the vacuum vessel, we may deduce a value of $\tau = 20$ ms [6.2.3].

A simplified calculation assuming $B_i = B_e$ yields an energy dissipation per unit conductor volume, E/V, for the

-	linear increase:	$E/V = (2/\mu_0)\,\dot{B}_i^2 \cdot \tau_0 \cdot t_0 =$	$3.2 \cdot 10^4\ J/m^3$	(4)
-	exp. decrease:	$E/V = (\Delta B^2/\mu_0) \cdot \tau_0/\tau =$	$1.6 \cdot 10^4\ J/m^3$	(5)
	Sum:	$E/V =$	$4.8 \cdot 10^4\ J/m^3$	

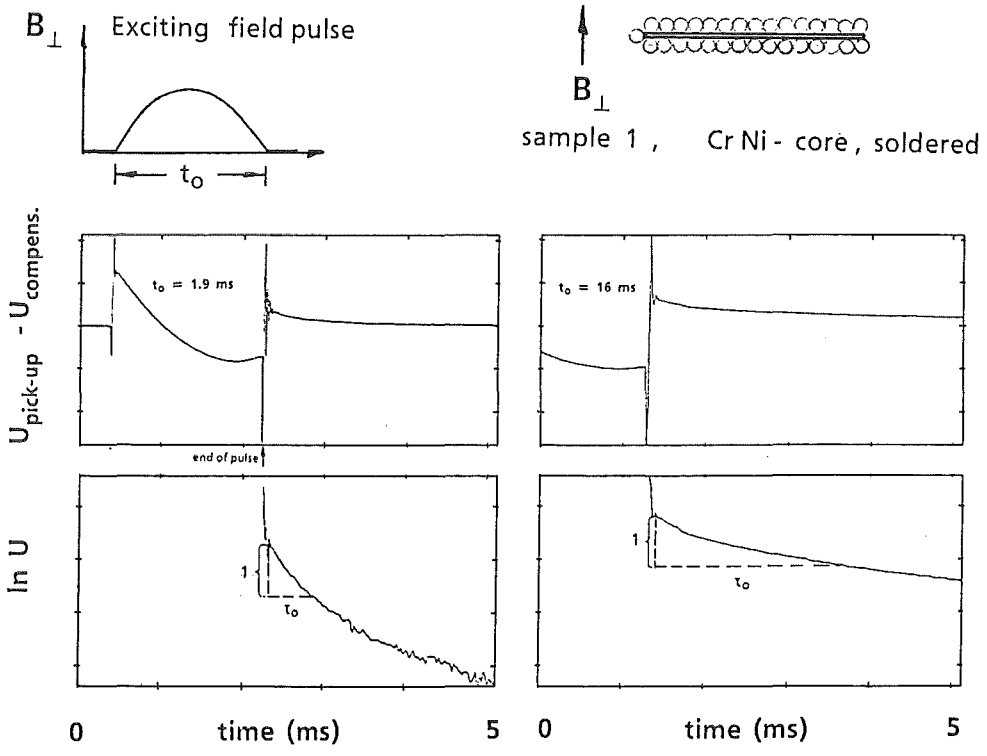

Fig.6.2.1: Compensated pick-up coil voltage and logarithm of this voltage for field pulses of 1.9 and 16 ms. The inset shows the exciting field pulse form.

6.2.1 Scaling for the Full Size Conductor

The time constant is expected to be $\propto \ell^2$ (cabling length). Assuming ℓ proportional to the broad face of the cable gives a scaling factor of ~ 9, or

$$\tau_0 = 23\,\text{ms}.$$

With this time constant the simplified assumption $B_i = B_e$ is not longer reasonable. A more exact calculation uses instead of Eqs. (4) and (5) for the

- linear increase: $E/V = (2/\mu_0)\,\dot{B}_i^2 \cdot \tau_0 \cdot t_0\,(1 + (\pi^2/4)\,(\tau_0/t_0)^2)^{-1}$ (6)
- exp. decrease: $E/V = (\Delta B^2/\mu_0)\,\tau_0/(\tau\,(1 + \tau/\tau_0))$ (7)

Introducing numerical values of the full size conductor yields for the

- linear increase: $6.9 \cdot 10^4\,\text{J/m3}$
- exponential decrease: $\underline{7.9 \cdot 10^4\,\text{J/m}^3}$

  Sum: $E/V = 1.5 \cdot 10^5\,\text{J/m}^3$

6.2.3 Stability during plasma disruption

The important quantity is energy dissipation per unit cooled surface area, $E/s = (E/V) \cdot (V/s)$.

Assuming that half of the broad faces are cooled (which is a very optimistic assumption), we get $V/s = 5 \cdot 10^{-3}$ m, and an energy dissipation per unit cooled surface area of

$$E/s = 739\,\text{J/m}^2 \qquad (8)$$

This value has to be compared with the transient heat removal capability of supercritical helium.

The diffusion model, which is well supported by experimentally measured transient heat transfer data [6.2.2], gives the maximum surface temperature increase for an exponentially decreasing heat load, as

$$\Delta T_{max} = 0.6 \cdot (E/s) \cdot (k\,C\,\tau_{th})^{-1/2} \qquad (9)$$

k and C are thermal conductivity and specific heat of supercritical helium (k ~ 0.022 W/mK, C ~ $3.4 \cdot 10^5$ J/m^3 at 4.2 K, 4 bar). τ_{th} is the time constant of the exponentially decreasing heat pulse. In the actual case we have a heat load with a complicated time dependence. For a rough estimation as it is done here, we might set the thermal time constant as half the value of the relevant field time constants, i.e. τ_{th} = 10 ms. (Because of $Q \propto \dot{B}_i^2$, τ_{th} is half the value of the field decay time constant for an exponentiell decay).

If we assume that a temperature increase of ΔT = 2 K is allowed, we get from Eq. (9) a maximal allowed energy input of

$$E/s = 29\ J/m^2. \qquad (10)$$

This is a factor of ~ 25 less than the expected energy input during a plasma disruption (Eq. 8). If we consider that the relation between the extracted time constant and the real AC losses of the cable is largely uncertain, we may assume that an error of a factor of two or even more seems possible. Anyway, the above calculation makes clear that the losses of the cable are still at least one order of magnitude too high to assure stability of the conductor during a plasma disruption.

References

[6.2.1] C. Schmidt et al.,Proceedings of the MT-9 (1985) p. 493

[6.2.2] C. Schmidt, Cryogenics, 28 (1988) 585

[6.2.3] L. Bottura et al.,Proc. 15th SOFT 19-23 Sept. 1988, Utrecht, The Netherlands, Nr. NET/88/Te/050-R-027

7. CONCLUSIONS

The design of the KfK-NET-TF react and wind conductor is based on the NET I parameters and fulfills the specifications given in Table 2.1 of this report.

The development phase of the conductor based on the following philosophy:

- A step by step progress to a full size superconductor development on the basis of an industrial manufacturing program of a relevant subsize conductor.
- Introducing of both manufacturing experience and conductor test results collected during the subsize development to the full size NET-TF superconductor.

This was followed during the development of the subsize conductor and led to the actual design of the conductor as seen in Fig. 3.1 with the main technical characteristics given in Tables 3.1 to 3.4. These tables contain a comparison of the data for the conductor at the state of 1986, 1988 and the present data at 1990 showing clearly the development steps and the performance of the conductor. Extended calculations on the stress load of the conductor core and on the thermohydraulics and electrical stability were performed. The industrial fabrication of a subsize conductor included all major manufacturing procedures necessary for a later full size cable fabrication:

- Cabling process of the Cu/Sn/Nb strands to a flat cable
- Reaction heat treatment for the Nb_3Sn formation
- Soldering of the reacted cable into two CuNi U-type sections to produce a rigid monolithic core
- Manufacturing of the electrical stabilizing units by the Roebel technique
- Soldering of the core between two stabilizing units to form a sandwich type cable
- Jacketing of the cable within stainless steel sections using the laser beam welding technique.

All steps could be successfully demonstrated. The produced subsize conductor was tested in KfK and the results confirmed the expectations. The critical current of the conductor was measured in its fabrication stages versus the magnetic field up

to 13 T and versus axial strain. No degradation in the various fabrication stages was found. The bronze route conductor demonstrated a predictable behavior and has the potential for increasing the current density: very recent experiments at KfK on Nb_3Sn multifilamentary wires prepared by the bronze route composite core process showed an increase of j_c by 20-30% with respect to the data in Table 3.3, j_c (overall, non Cu) being now $6.3 \cdot 10^4$ A/cm^2 at 12 T.

The development of a subsize conductor demonstrated that heat treatment and soldering were handled in industrial scale. The industrial fabrication of conductor components were demonstrated in other projects. The stabilizer cable has the industrial fabrication and soldering technique like the Euratom LCT conductor. A breakthrough in the laser beam welding technology for jacket fabrication was obtained by manufacturing 4 x 150 m Polo conductor. In a late state of the development phase of the subsize conductor the NET I design was replaced by NET II with remarkable enhancement of the size and requirements. New specifications given in Tables 2.2 to 2.4 for NET II required a new assessment of the conductor properties. This was done by using and improving the same calculation codes developed by the NET-team. The applicability of the KfK-NET-TF conductor for NET-TF coils was confirmed except the stability in case of a plasma disruption where the conductor will quench. To declare the severe condition of a plasma disruption as normal operation might be useful for plasma experiments, but is extremely questionable for plasma devices like NET which should proof fusion reactor relevant properties. Plasma disruptions causes problems in many other components, too and should therefore not be overstressed in the present state of development.

ACKNOWLEDGEMENT

This work has been performed in the framework of the Nuclear Fusion Project of the Kernforschungszentrum Karlsruhe and is supported by the European Communities within the European Fusion Technology Program. The industrial fabrication of the core and stabilizer of the subsize conductor were performed by VAC, Hanau, FRG. The jacket was manufactured by Dour Metall, Dour, Belgium. The heat treatment process was developed by KfK in close collaboration with PSI, Villingen, Switzerland. The computer codes of the NET team were modified for stability analysis.

The effort and continuous support of all partners in reaching the joint aim is gratefully acknowledged.